Technische Universität München

Development of Biomagnetic Interfaces for Magnetic Resonance Imaging and Magnetogenetic Actuation of Cells

Susanne Pettinger

Fakultät für Medizin

Fakultät für Medizin
Technische Universität München

Development of Biomagnetic Interfaces for Magnetic Resonance Imaging and Magnetogenetic Actuation of Cells

Susanne Katrin Pettinger

Vollständiger Abdruck der von der Fakultät für Medizin der Technischen Universität München zur Erlangung des akademischen Grades einer

Doktorin der Naturwissenschaften (Dr. rer. nat)

genehmigten Dissertation.

Vorsitzender:

Prof. Dr. Wolfgang A. Weber

Prüfende der Dissertation:

Prof. Dr. Gil Gregor Westmeyer
Prof. Dr. Wolfgang Wurst

Die Dissertation wurde am 01.10.2020 bei der Technischen Universität München eingereicht und durch die Fakultät für Medizin am 16.03.2021 angenommen.

Preface

The work presented in this thesis was conducted from June 2016 until February 2020 at the Institute of Biological and Medical Imaging (IBMI) and the Institute of Developmental Genetics (IDG) at the Helmholtz Zentrum München. The work was also funded by the International Graduate School of Science and Engineering (IGSSE) as part of the Technical University of Munich (TUM).

Parts of the presented work have been published in the following publications or are under preparation for publication:

*Sigmund, Felix; **Pettinger, Susanne**; Kube, Massimo; Schneider, Fabian; Schifferer, Martina; Schneider, Steffen et al. (2019): Iron-Sequestering Nanocompartments as Multiplexed Electron Microscopy Gene Reporters. In: ACS nano 13 (7), S. 8114–8123*

*Massner, Christoph; Sigmund, Felix; **Pettinger, Susanne**; Seeger, Markus; Hartmann, Carolin; Ivleva, Natalia P. et al. (2018): Genetically Controlled Lysosomal Entrapment of Superparamagnetic Ferritin for Multimodal and Multiscale Imaging and Actuation with Low Tissue Attenuation. In: Adv. Funct. Mater. 28 (19), S. 1706793. DOI: 10.1002/adfm.201706793.*

*Shams, Fatemeh S.; Ghazanfari, Mohammad Reza; **Pettinger, Susanne**; Tavabi, Amir; Siemensmeyer, Konrad; Smekhova, Alevtina et al. (2020): Structural perspective on revealing heat dissipation behavior of $CoFe_2O_4$-Pd nanohybrids: A great promise for magnetic fluid hyperthermia. **Under revision***

Zusammenfassung

Das menschliche Gehirn ist ein hochkomplexes System bestehend aus Milliarden von Neuronen und Synapsen, und bis heute bleibt es eine Herausforderung neuronale Prozesse zu entschlüsseln, die sowohl gesunden als auch kranken Zuständen zugrunde liegen. Verschiedene Bildgebungsverfahren wie zum Beispiel die nicht-invasive Magnetresonanz-Tomographie (MRT) oder hochauflösende Elektronenmikroskopie (EM) wurden entwickelt, welche es unter anderem ermöglichen molekulare Prozesse in einem biologischen Kontext zu studieren oder ein Konnektom zu erstellen, um detaillierte anatomische Informationen über die Verknüpfung von Synapsen in hoher Auflösung zu erhalten. Diese Techniken benötigen jedoch Kontrastmittel, um die ihnen zugrunde liegenden physikalische Limitationen zu überwinden, wodurch sich andere Herausforderungen ergeben, zum Beispiel bezüglich Verabreichung und Spezifität.

Obwohl Färbemethoden für EM normalerweise auf Schwermetallen wie Uran oder Blei beruhen, können Eisenoxide auch zu elektronendichtem Kontrast in der Elektronenmikroskopie führen, und gleichzeitig sind sie als Kontrastmittel auch für die Magnetresonanz-Tomographie geeignet. Zudem verfügen große, aus Magnetit bestehende Eisenoxide über vorteilhafte magnetische Eigenschaften und sind geeignet für magnetische Manipulationen von biologischen Systemen, wodurch sie die Bereiche der Bildgebung und Manipulation verknüpfen können. Obwohl Magnetit in der Natur vorkommt, zum Beispiel bei Käferschnecken oder bestimmten Bakterien, wurde eine genetisch kodierte, kontrollierbare Formation von Magnetit bisher jedoch nicht in aeroben Organismen erreicht. Das Ziel der vorliegenden Doktorarbeit war daher, verschiedene vollständig genetisch kodierte biologische Schnittstellen für MRT und EM zu entwickeln und zu charakterisieren, und die kontrollierte Bildung von Magnetit in einem biologischen Kontext zu untersuchen. Dazu wurden verschiedene protein-basierte Nanokompartimente in humanen Zellen exprimiert und bezüglich ihrer Fähigkeit Eisen einzulagern untersucht.

Der erste Teil der vorliegenden Arbeit konzentriert sich auf das ubiquitäre, Ferrihydrit-haltige Eisenlagerungs-Protein Ferritin sowie auf die Optimierung seiner magnetischen

Eigenschaften, um eine magnetische Interaktion mit Zellen zu ermöglichen. Während hoch-magnetisches, Magnetit-haltiges Ferritin (Magnetoferritin) bereits charakterisiert wurde, wurde der Magnetit-Kern nur durch eine *in vitro* Synthese erhalten, wodurch die Anwendbarkeit von Magnetoferritin als genetisch kodierte Schnittstelle stark eingeschränkt ist. In der vorliegenden Arbeit wurde sowohl an reinen Eisenpartikeln als auch an Ferritin detailliert untersucht, ob es möglich ist natürlich vorkommendes Ferrihydrit in das magnetisch bevorzugte Magnetit umzuwandeln. Diese Experimente beruhen auf der Hypothese, dass eine chemische Reduktion von Ferrihydrit eine Transformation zu Magnetit auslösen kann, weshalb verschiedene Reduktionsmittel und unterschiedliche pH-Konditionen getestet wurden. Zudem wurde die Anreicherung von Ferritin in lysosomalen Kompartimenten untersucht, um zu testen ob eine Agglomeration die magnetischen Eigenschaften von Ferrihydrit verbessern kann. Obwohl eine chemische Umwandlung von reinen Ferrihydrit-Partikeln zu Magnetit erfolgreich unter aeroben Bedingungen gezeigt werden konnte, konnten diese Ergebnisse nicht übertragen werden auf protein-umhülltes Ferrihydrit im Inneren von Ferritin. Daher ist Ferritin bisher nur eingeschränkt als genetisch kodiertes Kontrastmittel einsetzbar.

Im zweiten Teil der Arbeit liegt der Fokus auf der Charakterisierung eines neuen, proteinbasierten Nanokompartments bakteriellen Ursprungs: dem Encapsulin-System aus *Quasibacillus thermotolerans* (Qt), welches aus einem Hüllprotein und dem dazugehörigen Cargo-Protein besteht. Encapsuline sind bakterielle Nanokompartimente die an verschiedenen metabolischen Prozessen beteiligt sind, und einige enthalten Ferroxidasen als Protein-Cargo, was auf eine Rolle im Eisenmetabolismus schließen lässt. Das Encapsulin, das in dieser Arbeit gewählt wurde, ist assoziiert mit einem neuen Ferroxidase-Typ, und sowohl Hülle als auch Cargo-Protein wurden in der vorliegenden Arbeit charakterisiert. Expression und selbstständige Zusammenlagerung der Hülle sowie Einbau des Cargos wurden sowohl in *E. coli* als auch in humanen Zellen gezeigt. Zudem wurde eine Kryo-EM Analyse durchgeführt um detaillierte strukturelle Informationen zu erhalten, wodurch entdeckt wurde, dass dieses das erste Encapsulin mit einer Triangulationsnummer von T = 4 ist und damit das größte bisher bekannte Encapsulin. Zudem konnte gezeigt werden, dass das Cargo Ferroxidase-Aktivität besitzt und zu Eisenablagerungen in der Encapsulin Hülle führt. Die Qt Ferroxidase zeigt ein verbessertes Eisenablagerungs-Verhalten im direkten Vergleich sowohl zu einem weiteren Encapsulin als auch zu Ferritin, weshalb eine Eignung als MRT Kontrastmittel überprüft wurde. Zudem konnte gezeigt werden, dass das Qt Encapsulin als vollständig genetisch kodiertes EM-Kontrastmittel geeignet ist, da es zur Bildung von elektronenreichen, klar erkennbaren Partikeln führt.

Summary

The human brain is a highly complex structure consisting of billions of neurons and synapses, and to date it remains a challenge to uncover the neuronal processes underlying physiological and diseased states. Different imaging techniques have been developed, such as non-invasive magnetic resonance imaging (MRI) or high-resolution electron microscopy (EM) which, for example, allow to study molecular processes in their biological context or to construct a connectome in order to obtain detailed anatomical information about the synaptic wiring with high resolution. However, these techniques require contrast agents to overcome inherent physical limitations, which poses a challenge in regards to, *e.g.*, delivery and specificity.

While EM staining techniques are usually based on heavy metals such as uranium or lead, iron oxides can also yield electron-dense contrast in electron microscopy, and at the same time they are also suitable as contrast agents for magnetic resonance imaging. Furthermore, large iron oxide particles consisting of magnetite have favorable magnetic properties enabling magnetic manipulations of biological systems, thus bridging the fields of imaging and manipulation. However, while magnetite can be found in nature, for example in chitons or certain bacteria, a genetically-controlled, induced magnetite formation was not achieved in aerobic organisms yet. The aim of this doctoral thesis was thus to develop and characterize different fully genetically encoded biological interfaces for MRI as well as EM, and to examine the controlled formation of magnetite in a biological context. To this end, different proteinaceous nano-compartments were expressed in mammalian cells and characterized in regards to their iron accumulation capability.

The first part of this work focused on the ubiquitous, ferrihydrite-forming iron storage protein ferritin and the improvement of its magnetic properties to enable magnetic interactions with cells. While highly-magnetic, magnetite containing ferritin (magnetoferritin) has already been characterized, the magnetite core is obtained by *in vitro* synthesis, thus limiting the applicability of magnetoferritin as a genetically encoded interface. In this work, the possibility to transform naturally occurring ferrihydrite to magnetically more favorable magnetite was studied in detail both on uncoated particles and inside the ferritin protein shell. This work was based on the hypothesis that a reduction of ferrihydrite can lead to a transformation to magnetite, and thus different

reducing agents as well as different pH conditions were tested. In addition, an accumulation of ferritin inside cellular lysosomal compartments was examined to test whether agglomeration effects can enhance the magnetic properties of ferrihydrite. However, while a chemical transformation of uncoated ferrihydrite particles to magnetite could be demonstrated under aerobic conditions, these results could not be transferred to experiments with ferritin-encapsulated particles. Thus, ferritin had to be considered as restricted in its applicability as a genetically encoded contrast agent and actuator.

The second part of this work concentrated on the characterization of a new, proteinaceous nano-compartment of bacterial origin: the encapsulin system of *Quasibacillus thermotolerans* (Qt) consisting of a shell protein and a self-sorting cargo. Encapsulins are bacterial nano-compartments involved in various metabolic processes, and some reportedly encapsulate ferroxidases as cargos, which indicates that they play a role in iron metabolism. The encapsulin chosen for this work is associated with a new type of ferroxidase, and both shell and cargo have been characterized in this work. Expression, self-assembly and cargo auto-targeting were demonstrated both in *E. coli* and in mammalian cells. In addition, cryo-EM analysis was performed to gain in-depth structural information, which revealed that this encapsulin is the first to be reported with a triangulation number T = 4, thus making it the largest encapsulin known so far. In addition, the native cargo was confirmed to possess ferroxidase activity and its capability to accumulate iron inside the encapsulin shell was demonstrated. The Qt ferroxidase was demonstrated to have a superior iron sequestration capability in direct comparison to another encapsulin system as well as to ferritin, which highlights the suitability of iron-loaded Qt encapsulin as a contrast agent for magnetic resonance imaging. In addition, the Qt encapsulin was shown to be suitable as a fully genetically encoded electron microscopy contrast agent as it yielded electron-dense, clearly distinguishable particles in cellular TEM.

Contents

List of Figures

List of Tables

Abbreviations

ALF	Artificial lysosomal fluid
asc	ascorbic acid
BN-PAGE	Blue Native-Polyacrylamide Gel Electrophoresis
Cryo-EM	Cryo-electron microcopy
DAB-PB	3,3-diaminobenzidine enhanced Prussian Blue stain
DMEM	Dulbecco's modified Eagle's medium
DNA	Deoxyribonucleic acid
DPBS	Dulbecco's phosphate-buffered saline
EM	Electron microscopy
enc	encapsulin
FAS	Ferrous ammonium sulfate
FBS	Fetal bovine serum
Fe	iron
Ft	ferritin
Goe	goethite
HEK 293T	Human embryonic kidney cells
Hem	hematite
HEPES	4-(2-hydroxyethyl)-1-piperazineethanesulfonic acid
ICP-MS	Inductively coupled plasma mass spectrometry
IPTG	Isopropyl-β-D-thiogalactopyranoside
Lep	lepidocrocite
Mag	magnetite
Mgh	maghemite

MRI	Magnetic resonance imaging
Mx	Myxococcus xanthus
PFA	Paraformaldehyde
ROI	Region of interest
ROS	Reactive oxygen species
SDS-PAGE	Sodium dodecyl sulfate-Polyacrylamide Gel Electrophoresis
SQUID	superconducting quantum interference device
TAE	Tris-Acetate-EDTA buffer
TBS	Tris-buffered saline
TEM	Transmission electron microscopy
TfR1	Transferrin receptor 1
Tm	Thermotoga maritima
VSM	Vibrating sample magnetometer
Qt	Quasibacillus thermotolerans
ZFC/FC	Zero-field-cooling / field-cooling
Zip14	ZRT, IRT1-like protein 14

Chapter 1| Introduction

The brain is a highly complex structure consisting of billions of neurons and synapses with a vast diversity in cell types differing in their molecular expression patterns, connectivity and physiological activity. In order to shed light onto neuronal processes and to understand physiological as well as diseased states, tools are required to enable high-resolution imaging and the extraction of molecular information.

While substantial progress has been made in obtaining connectomes from different model organisms such as *Caenorhabditis elegans*, *Cionia intestinalis*, the fruit fly *Drosophila melanogaster*, and even the mouse brain (Takemura et al. 2013; Kasthuri et al. 2015; Helmstaedter et al. 2013; Ryan et al. 2016; White et al. 1986; Bhattacharya et al. 2019), this task is still challenging as it requires a careful sample processing and acquisition as well as the analysis of huge data sets. Connectome data are currently obtained using electron microscopy (EM), which allows a high resolution but requires a tedious reconstruction, even though progress is made in high-throughput EM and semi-automated pipelines (Tamura et al. 2015; Chiang et al. 2011; Helmstaedter 2013). However, while a vast toolbox of multicolor fluorescent proteins is available for other imaging techniques such as fluorescence microscopy (Shaner et al. 2007; Tsien 1998), equivalent genetic tools for EM are still lacking. While some semi-genetic EM markers are available (Martell et al. 2012; Lam et al. 2015; Shu et al. 2011; Joesch et al. 2016; Bouchet-Marquis et al. 2012), they are based on the genetically controlled precipitation of exogenous chemicals and thus have only limited spatial precision and lack tissue penetration. Furthermore, specimens have to be fixed and permeabilized during EM sample preparation, which potentially affects their ultrastructure and thus constrains chemical EM stains such as gold immunolabelling or antibody labelling (Fang et al. 2018; Hagiwara et al. 2010; Pallotto et al. 2015; Shahidi et al. 2015).

Ferritin (Ft), an ubiquitous iron storage protein (Masuda et al. 2010; Andrews 2010), has been proposed as a fully genetically encoded EM marker, but due to its small size it is hard to distinguish against the cellular background (Wang et al. 2011; Matsumoto et al. 2015; Clarke und Royle 2018). Interestingly, ferritin has also been suggested as a magnetic resonance imaging (MRI) contrast agent (Cohen et al. 2005; Cohen et al. 2007; Iordanova und Ahrens 2012; Feng et al. 2012; Naumova et al. 2010), but it generates only weak contrast and requires iron supplementation. While different groups worked

extensively on the improvement of Ft-related relaxivity, the underlying mechanism of contrast enhancement is still being questioned.

1.1 Iron mineralization in biology

Iron as the most common element on earth is not only a major component of Earth's outer and inner core, it is also an essential trace element for most creatures. A total of 16 different iron oxides, hydroxides and oxide-hydroxides are known, which consist of different combinations of elemental iron (Fe), oxygen (O) and hydroxyl groups (-OH) and will be jointly referred to as iron oxides in the following (Cornell und Schwertmann 2003; Liu et al. 2007). As a transition metal iron has multiple oxidation states, with the most common ones being 0 (metallic), +2 (iron(II), ferrous) and +3 (iron(III), ferric). In iron oxide compounds Fe usually takes on a trivalent state, with the three exceptions wüstite (divalent), iron(II) hydroxide (divalent) and magnetite (mixed divalent and trivalent) (Cornell und Schwertmann 2003).

Iron oxides are not only of interest for geosciences such as geology or mineralogy, they also found various applications in (industrial) chemistry or medicine as inorganic pigments, precursors for permanent magnets (Cudennec und Lecerf 2005, 2006) or as contrast agents (Sun et al. 2008; Laurent et al. 2008) (**Figure 1A**). Furthermore, they play an important role in the field of biology as most life forms are dependent on iron. In nature, poorly crystallized iron oxides such as ferrihydrite (Ft) or green rust are the first to form when iron is oxidized in solution, and the degree of crystallization and structural order increases with time when further solid phases are formed, the main ones relevant in nature being goethite (goe), lepidocrocite (lep), hematite (hem) and maghemite (mgh) (Cudennec und Lecerf 2005, 2006; Liu et al. 2007). These transformations between iron oxides are influenced by different environmental factors such as pH, presence of ligands or inhibitors, and presence of other metals (Cornell und Schwertmann 2003; Cudennec und Lecerf 2005; Faivre 2016; Ivanov und Kosoy 1975) and can be roughly classified as either topotactic or reconstructive. Topotactic transformations are based on internal atomic re-arrangements, transforming one crystal into another within the solid phase, which is only possible if the two iron oxide phases are structurally related (Cornell und Schwertmann 2003; Cudennec und Lecerf 2005). In contrast, reconstructive transformations are based on dissolution and re-precipitation processes, and no structural relationship between precursor and product is needed as the initial phase is completely broken down before a new, usually thermodynamically more stable, phase precipitates again from the solution (Cornell und Schwertmann 2003; Hansel et al. 2005). The end phases of natural transformation processes are often either goethite or hematite, as these two are thermodynamically the most stable iron oxides at ambient temperatures (Cornell und Schwertmann 2003; Cudennec und Lecerf 2005; Liu et al. 2007). The crystals formed during these processes are often small, in the range of

nanometers to micrometers but with high specific surface areas, as crystallization processes require a lot of energy (Cornell und Schwertmann 2003).

1.1.1 Iron oxides in nature

Of the 16 known iron oxides, six are synthetic compounds only synthesized in laboratories; apart from these, all major iron oxides except for hematite can be found in organisms where they fulfil various functions mostly in metabolism or as supporting materials (Cornell und Schwertmann 2003; Liu et al. 2007).

Ferrihydrite

Ferrihydrite (Ft) is widespread in the surface environment and precipitates rapidly upon hydrolysis of Fe^{3+} solutions, thus making it the first iron oxide phase to form in most cases (Cornell und Schwertmann 2003; Cudennec und Lecerf 2006; Hansel et al. 2005). However, Ft exists only as nano-crystals and is thermodynamically unstable with respect to many other iron oxides, thus serving as a precursor for better crystalline Fe oxides and transforming into more stable phases if not stabilized (Cornell und Schwertmann 2003; Liu et al. 2007). While this conversion is slow without catalysts, even low Fe^{2+} concentrations are sufficient to trigger a phase transformation, which raised questions regarding the availability and stability of Ft in natural systems (Hansel et al. 2005).

Ferrihydrite is only poorly crystalline, so while it is known to be a ferric iron hydroxide its definite structure and chemical formula are still controversial due to the nanoparticulate formation and a variable composition of OH and H_2O (Cornell und Schwertmann 2003). The empirical formula is $(Fe^{3+})_2O_3 \bullet 0.5\ H_2O$, but it can also be given as $(Fe^{3+})_5O_8H \bullet H_2O$ (Cornell und Schwertmann 2003) or $5(Fe^{3+})_2O_3 \bullet 9\ H_2O$ (Cudennec und Lecerf 2006) among others. Ferrihydrite crystals consist of a mixture of defect-free and defective structural units, with an overall octahedral iron coordination and Fe-deficient sites (Cornell und Schwertmann 2003). However, the possibility of tetrahedral Fe coordination on the crystal surface is being discussed (Hansel et al. 2005).

Magnetite and maghemite

Magnetite (mag) is one of the most important iron ores and responsible for the magnetic properties of rocks, as it is either ferrimagnetic or super-paramagnetic (when smaller than 6 nm) at room temperature (Cornell und Schwertmann 2003). It is classified as an iron oxide of mixed ferric and ferrous composition and can be described with the formula $Fe^{2+}(Fe^{3+})_2O_4$ (Cornell und Schwertmann 2003). Stochiometric magnetite thus has a Fe^{2+} : Fe^{3+} ratio of 0.5; however, non-stochiometric magnetite with cation-deficient Fe^{3+} sub-lattices are also known (Cornell und Schwertmann 2003). In general, mag has an inverse spinel structure, the ferrous iron occupying octahedral sites and while the ferric

iron can occupy both tetrahedral and octahedral sites (Cornell und Schwertmann 2003; Hansel et al. 2005).

Maghemite is isostructural to magnetite and also referred to as “oxidized magnetite” as it consists entirely of trivalent iron with the chemical formula being γ-$(Fe^{3+})_2O_3$ (Cornell und Schwertmann 2003; Cudennec und Lecerf 2005). Like magnetite, it displays ferrimagnetic behavior at room temperature or super-paramagnetic properties beneath a size of 10 nm. In nature, maghemite is a weathering product of magnetite in soils, and in the laboratory it is one of the end products obtained when heating other iron oxides (Cornell und Schwertmann 2003). As mag and mgh are structurally closely related, the latter also has a spinel structure but shows vacancies in some octahedral sites which would have been occupied by ferrous iron as a compensation for the oxidation to Fe^{3+} (Cornell und Schwertmann 2003).

Apart from magnetite and maghemite, the only other iron oxide displaying magnetic behavior is feroxyhyte. However, this ferric oxide-hydroxide is only formed under high pressure conditions, *e.g.* in the depths of oceans and seas, and rapidly transforms to goethite when exposed to air (Cornell und Schwertmann 2003).

1.1.2 The principals of iron homeostasis and storage

Iron as a mineral is essential for life, but it forms insoluble iron oxides under physiological conditions (Boyer und J. McCleary 1987): both ferrous and ferric iron are poorly soluble at neutral pH in aerobic environments, which poses a challenge for aerobic organisms that depend on ferric iron acquisition to maintain biological functions (Cornell und Schwertmann 2003). Furthermore, poorly chelated Fe^{2+} can lead to the formation of reactive oxygen species (ROS), which mediate cellular damage and are even suggested to play a role in certain neurodegenerative diseases (Badu-Boateng et al. 2017; Xiao et al. 2018). Thus, iron metabolism has to be tightly controlled and organisms have developed strategies both for the uptake and the storage of iron, usually as complexes with proteins or chelates (Reif 1992; Badu-Boateng et al. 2017).

The role of ferritin in higher vertebrates

The ferritin protein (E.C. 1.16.3.1) is widely distributed in vertebrates, invertebrates, plants, fungi and bacterial species (Crichton 1984; Carmona et al. 2014; Theil et al. 2013) and plays a crucial role in many biological and chemical processes involving iron and oxygen, including electron transfer, nitrogen fixation, deoxyribonucleotide synthesis, and detoxification of reactive oxygen species among others (Vladimirova und Kochev 2010; Honarmand Ebrahimi et al. 2015; Octave et al. 1983). First described in the late 1930’s as an iron-containing protein by Laufberger (Laufberger 1937), it has even been highlighted as important for the transition of anaerobic to aerobic life (Theil 2011). Ferritin fulfills a double function as the main intracellular iron storage protein supporting iron-

dependent cellular processes and as an iron scavenger aiding in the detoxification of excess iron, thus keeping iron in a physiologically safe form while preventing ROS-mediated oxidative damage (Baader et al. 1996; Roginsky et al. 1997; Reif 1992; Vladimirova und Kochev 2010; Theil 2011; Honarmand Ebrahimi et al. 2015; Treffry et al. 1992; Crichton 1984).

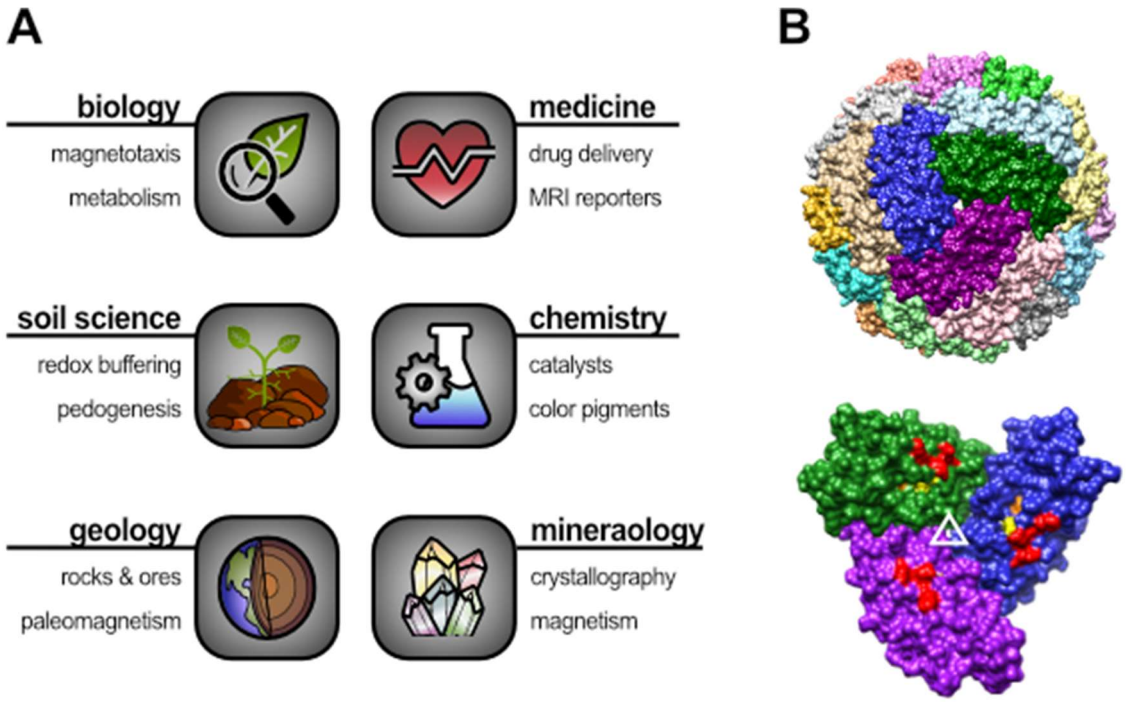

Figure 1| The role of iron in nature.
A) Iron and iron oxides play an important role in various different scientific fields. Scheme adapted from (Cornell und Schwertmann 2003; Faivre 2016). **B)** Structure of the iron storage protein ferritin centered on a three-fold pore (top) and close-up of three ferritin monomers forming a three-fold pore (white triangle) as viewed from the inside of the shell (bottom). The ferroxidase sites are highlighted in yellow (site A), orange (site B) and red (site C). Structures were created with Chimera 1.14 based on PDB entry 2FHA and based on (Honarmand Ebrahimi et al. 2015; Toussaint et al. 2007).

Ferritins are spherical, cage-like proteins that form highly symmetric hollow nanospheres about 12 nm in diameter (**Figure 1B**, top) (Vladimirova und Kochev 2010; Theil 2011; Badu-Boateng und Naftalin 2019; Honarmand Ebrahimi et al. 2015; Crichton 1984). They self-assemble from 24 monomers, each of them consisting of a four-helix bundle (helices A to D) with a fifth short α-helix (E) at the C-terminal end tilted at a 60° angle (Toussaint et al. 2007; Vladimirova und Kochev 2010). The ferritin cavity can be filled with up to 4,500 iron atoms forming ferrihydrite-like nanocrystals laced with phosphate, although under physiological conditions only 500-2,500 Fe/cage are stored (Reif 1992; Dognin und Crichton 1975; Vladimirova und Kochev 2010; Xiao et al. 2018; Badu-Boateng und Naftalin 2019; Badu-Boateng et al. 2017; Lawson et al. 1989; Treffry et al. 1992; Theil 2011). Ferritin is a very robust protein which is not only stable in respect to heat, urea, and guanidine but also tolerates a broad pH range between 3 and 11 (Crichton 1984; Granick 1942; Theil et al. 2013). Due to these properties, ferritin has found many biotechnological applications, *e.g.* for the production of nanomaterials with a narrow,

defined size distribution and enhanced biocompatibility, for targeted drug delivery, and for the encapsulation of contrast agents such as fluorophores or radionucleotides (Theil et al. 2013; Honarmand Ebrahimi et al. 2015).

Ferritins in bacteria and archaea are made up of only one subunit-type, whereas plants and animals have two different ferritin subunits termed light-chain and heavy-chain, which allows a tissue-specific control over mineralization (Theil 2011; Masuda et al. 2010; Toussaint et al. 2007; Carmona et al. 2014). In general, L-chain rich ferritins show slower iron oxidation rates but better nucleation and storage capabilities and an overall improved iron mineralization (Badu-Boateng et al. 2017; Badu-Boateng und Naftalin 2019; Carmona et al. 2014). While early works suggested the iron mineral forms in solution and is encased during ferritin assembly (Pape et al. 1968), iron uptake into intact ferritin shells via channels has been postulated in 1970 by Niederer et. al. (Niederer 1970). Indeed, the heavy-chain subunit was demonstrated to contain a ferroxidase center buried within the four-helix bundle subunits (Lawson et al. 1989; Lawson et al. 1991; Toussaint et al. 2007; Honarmand Ebrahimi et al. 2015) enabling fast oxidation of ferrous to ferric iron. The light-chain subunits, on the other hand, are thought to contain a nucleation site thus aiding the nucleation process (Theil 2011; Badu-Boateng et al. 2017; Honarmand Ebrahimi et al. 2015; Toussaint et al. 2007) and were also suggested to manage electron transfer across the protein shell (Carmona et al. 2014). Further structural analysis of ferritin crystal structures reveled that each heavy-chain subunit contains three metal-binding sites (**Figure 1B**, bottom), which are heavily conserved among heavy-chain ferritins (Lawson et al. 1991; Lawson et al. 1989; Treffry et al. 1992). In human H-chain ferritin, site A coordinates one iron atom via the amino acid residues Glu27 and His65 and site B via Glu107; in addition, the residue Glu62 bridges the two iron atoms via its two oxygen atoms (Toussaint et al. 2007; Treffry et al. 1992; Lawson et al. 1991; Lawson et al. 1989; Honarmand Ebrahimi et al. 2015). These two sites are thought to constitute the di-iron ferroxidase center (Toussaint et al. 2007; Lawson et al. 1991; Lawson et al. 1989). The third binding site, C, is located closer to the inner surface of the cavity and coordinates another iron atom via the residues His60, Glu64 and Glu67 (Toussaint et al. 2007; Lawson et al. 1991). Other amino acid resides such as Tyr34, Glu61 and Gln141 have also been reported to be directly involved in iron coordination at one of the three sites (Lawson et al. 1991; Masuda et al. 2010), but these findings could not be supported by other reports (Toussaint et al. 2007; Treffry et al. 1992).

The general process of iron uptake into ferritin was postulated as a multistep process, where iron upon its delivery is transferred to the ferroxidase center (sites A and B) and oxidized before nucleation is initiated at specific sites on the inner cavity surface (Lawson et al. 1991; Masuda et al. 2010; Toussaint et al. 2007; Honarmand Ebrahimi et al. 2015; Boyer und J. McCleary 1987). While a potential narrow 1-fold channel has been predicted by molecular dynamics simulations leading from the protein surface directly to the ferroxidase centers (Honarmand Ebrahimi et al. 2015; Lawson et al. 1991), it is in general assumed that iron enters through eight hydrophilic three-fold channels (Boyer

und J. McCleary 1987; Theil 2011; Masuda et al. 2010; Crichton 1984; Theil et al. 2013). After its uptake, ferrous iron is sequentially oxidized at the di-iron ferroxidase center consisting of the sites A and B using O_2 or H_2O_2 as the electron acceptor, and is has been postulated that site A binds iron first as the affinity of site B for iron is low when A is empty (Toussaint et al. 2007; Badu-Boateng et al. 2017; Theil 2011; Honarmand Ebrahimi et al. 2015; Treffry et al. 1992). The role of the third iron binding site C in the overall process is still not clear even though this site can also clearly bind iron; however, it has been suggested to serve as a gateway translocating iron into and out of the ferroxidase center (Lawson et al. 1991; Toussaint et al. 2007; Honarmand Ebrahimi et al. 2015).

As ferritin is meant as a temporary storage rather than a terminal iron sink, iron has to be released again to partake in cellular processes. However, an uncontrolled release of iron could not only disrupt the cellular iron metabolism, but also lead to the production of ROS and thus cause damage to DNA, lipids and proteins (Reif 1992; Baader et al. 1996). Therefore, iron release from ferritin has to be regulated, and two potential mechanisms are being proposed. One option would be the proteolytic degradation of the ferritin protein shell inside lysosomes, which would allow to access the complete ferrihydrite mineral; however, this process is mostly uncontrolled and therefore potentially toxic (Badu-Boateng und Naftalin 2019; Badu-Boateng et al. 2017). It is thus more likely that iron is released by reducing ferric iron on the surface of the ferrihydrite core to more soluble ferrous iron (Bienfait und van den Briel, M. L. 1980; Dognin und Crichton 1975; Theil 2011). This method either requires reductants that can enter the core via diffusion through three-fold channels or electron tunneling through the ferritin shell or the hydrophobic four-fold channels via an electron transport chain (Badu-Boateng et al. 2017; Badu-Boateng und Naftalin 2019; Vladimirova und Kochev 2010; Bienfait und van den Briel, M. L. 1980; Crichton 1984). In experiments, a reductive release of iron from ferritin was, for example, triggered by thiols, flavins, superoxide, nitric oxide and different reducing agents such as ascorbate, cysteine or glutathione as well as by siderophores and catecholamides with different release rates (Boyer und J. McCleary 1987; Sirivech et al. 1974; Baader et al. 1996; Roginsky et al. 1997; Mazur et al. 1955; Reif 1992; Dognin und Crichton 1975). While it remains controversial whether Fe^{2+} generated inside the ferritin cavity requires a chelator to be mobilized from ferritin (Watt et al. 1985; Boyer und J. McCleary 1987; Reif 1992; Roginsky et al. 1997) or whether it can exit the protein shell via the respective channels (Vladimirova und Kochev 2010; Badu-Boateng et al. 2017; Badu-Boateng und Naftalin 2019; Theil 2011), a reductive dissolution of ferrihydrite in either case allows for controlled iron mobilization, thus minimizing the risk of toxic side effects for organisms.

1.2 Encapsulins and their role in bacterial metabolism

The first encapsulin was originally described as a large proteinaceous aggregate composed of a single monomer subunit with bacteriocin activity isolated from *Brevibacterium linens* M18 (Valdés-Stauber und Scherer 1994), and few years later homologous multi-subunit proteins were discovered in *Mycobacterium tuberculosis* (Rosenkrands et al. 1998) and in *Thermotoga maritima* (Tm), which was described as a homo-multimeric protease of large globular structure with gene sequence homology to the *B. linens* bacteriocin (Hicks et al. 1998). The third encapsulin, discovered in *Pyrococcus furiosus* almost a decade later (Namba et al. 2005), was originally characterized as a non-infectious virus-like particle devoid of nucleic acids (Akita et al. 2007) before all three structures were recognized as belonging to a widespread family of conserved bacterial proteins, which were re-named as encapsulins (Sutter et al. 2008). Encapsulins (enc) are proteinaceous nano-compartments found in bacteria and archaea sharing a HK97-like fold despite having only low amino acid identity (Akita et al. 2007), and they can encapsulate cargo proteins via a short, conserved N- or C-terminal targeting peptide (Giessen 2016; Sutter et al. 2008; McHugh et al. 2014; Sigmund et al. 2018; Giessen und Silver 2017). Interestingly, the HK97-fold is found not only in bacterial viruses but also in human herpes viruses and encapsulins of archaeal origin, hinting at a common evolutionary root linking all three domains of life (Heinemann et al. 2011; Sutter et al. 2008). It was thus suggested that encapsulins could be of viral origin with an HK97-ancestor that emerged before the bacterial and archaeal kingdoms separated (Sutter et al. 2008; Heinemann et al. 2011; Akita et al. 2007). A recent study identified 909 putative encapsulin systems in different bacteria and archaea, as well as several new cargo types such as haem-erythrins, di-iron proteins and a copper nitrite reductase-hydroxylamine oxidoreductase (NIR-HAO) fusion construct (Giessen und Silver 2017), indicating a vast potential in the field of encapsulin research.

Chapter 2| Materials and Methods

All chemicals were purchased from Sigma Aldrich or Merck if not stated otherwise. Deionized and ultrapure water were autoclaved before use.

2.1 Preparation of ferrihydrite particles and ferritin

Naked ferrihydrite particles were prepared and supplied by our collaboration partner Carolin Hartmann as described in (Hartmann et al. 2019) and stored dry at room temperature in the dark. For transformation experiments, 10 mg of ferrihydrite particles were incubated in 500 µl of indicated buffer in the dark with periodic mixing as indicated for each experiment. For Raman analysis, samples were vortexed to mix well and 50 µl were supplied for measurements performed by Carolin Hartmann (TU München).

Artificial lysosomal fluid (ALF) 10x buffer was prepared based on (Stopford et al. 2003; Thélohan und Meringo 1994) according to Table 1 and the pH was adjusted to either 4.6 or 7.4 with 1 M sodium hydroxide. Autoclaved buffer was stored at 4 °C and freshly diluted with Milli-Q water directly before use. 400 µL protein solution with known concentration were dialyzed against 1 L ALF 1x buffer for 24 h at 4 °C with constant stirring using Slide-A-Lyzer™ Dialysis Cassettes (ThermoFisher Scientific) with a molecular weight cut-off of 10,000. After incubation, samples were centrifuged at 13,000 rpm for 10 min and protein concentration of the supernatant was determined using the Pierce™ BCA Protein Assay Kit (ThermoFisher Scientific). Samples were analyzed with Native-PAGE according to chapter 2.2.2. Pellet and supernatant were stored at 4 °C; the supernatant was dialyzed against 50 mM HEPES buffer for 24 h at 4 °C using Slide-A-Lyzer™ dialysis cassettes (ThermoFisher Scientific) before storage.

Table 1| Composition of artificial lysosomal fluid (ALF) 10x buffer.

Compound	Chemical formula	c [g/L]	c [mol/L]
Trisodium citrate dihydrate	$Na_3C_6H_5O_7$	0.077	$2.6 \cdot 10^{-4}$
Sodium hydroxide	NaOH	6.000	$1.5 \cdot 10^{-1}$
Citric acid	$C_6H_8O_7$	20.800	$1.1 \cdot 10^{-1}$
Magnesium chloride	$MgCl_2$	0.050	$5.3 \cdot 10^{-4}$
Sodium chloride	NaCl	3.210	$5.5 \cdot 10^{-2}$
Disodium phosphate	Na_2HPO_4	0.071	$5.0 \cdot 10^{-4}$
Sodium sulfate	Na_2SO_4	0.039	$2.7 \cdot 10^{-4}$
Calcium chloride dihydrate	$CaCl_2 \cdot 2\ H_2O$	0.128	$8.7 \cdot 10^{-4}$
Glycine	$C_2H_5NO_2$	0.059	$7.9 \cdot 10^{-4}$
Sodium tartrate	$Na_2C_4H_4O_6$	0.090	$3.9 \cdot 10^{-4}$
Sodium lactate	$C_3H_5NaO_3$	0.085	$7.6 \cdot 10^{-4}$
Sodium pyruvate	$C_3H_3NaO_3$	0.086	$7.8 \cdot 10^{-4}$

2.2 Molecular Biology Techniques

2.2.1 Construct design and plasmid preparation

Primers, gBlocks and plasmid constructs were designed using Geneious Prime software. Enzymes were purchased from New England Biolabs. Sequencing was performed by Eurofins Genomics (Eurofins). Primer and gBlocks were purchased from IDT DNA and cloned into the appropriate vector backbone using restriction digestion followed by ligation or Gibson Assembly.

For gene expression in bacterial cultures, the gene of interest was inserted into the multiple cloning site (MCS) of pRSFDuet™-1 backbone (Novagene) either via restriction digestion followed by ligation or via Gibson Assembly designed using the program NEBuilder Assembly Tool. PCR reactions were performed with Q5 High-Fidelity 2x Master mix (New England Biolabs) in 25 µl reaction volume containing final concentrations of 0.5 µM of each forward and reverse primer. The PCR program contained an initial denaturation step at 98 °C (30 sec), 35 cycles of denaturation at 98 °C (10 sec), primer annealing (20 sec) at a primer-specific temperature calculated according to the NEB Tm calculator (New England Biolabs) and elongation at 72 °C (30 seconds / kB), and a final elongation step at 72 °C (3 min). Restriction digestions were

planned using the NEBcloner program; double digestions were performed in 50 µl reaction volume using the recommended buffer and incubated for 10 min at 37 °C. Digested constructs were either purified via gel electrophoresis or via the Monarch PCR&DNA clean-up kit (New England Biolabs). For Gibson Assemblies, the NEBuilder HiFi DNA Assembly Master Mix was used and reactions were set up according to the manufacturer with a vector:insert ratio of 1:2 using 100 ng vector and sample incubation at 50 °C for 15 min. Obtained vector constructs were transformed into OneShot Top10 chemically competent *E. coli* (Thermo Fisher Scientific) or NEB Stable Competent *E. coli* (High Efficiency) (New England Biolabs) and plated on LB-agar plates containing the respective antibiotics. Sequence insertion was tested via colony-PCR using DreamTaq Green DNA-Polymerase 2x Master Mix (Thermo Fisher Scientific) according to the manufacturer using single colonies of transformed *E. coli* as template. Correct sequence identity was confirmed by sequencing of DNA prepared with QIAprep Spin Miniprep Kit (Qiagen) or PureYield Plasmid Maxiprep System (Promega).

2.2.2 Gel electrophoresis

Protein extraction from mammalian cells was performed using M-Per Mammalian Protein Extraction Reagent (Thermo Fisher Scientific) containing a protease inhibitor cocktail (Sigma-Aldrich). In brief, cells were washed twice with DPBS, M-Per was added as specified in the user's manual and cells were incubated for 15 min on an orbital shaker. Samples were centrifuged at 13,000 rpm in a table-top centrifuge for 5 min to spin down debris and protein extracts were stored at -20 °C until use.

Agarose gel electrophoresis

For electrophoresis of DNA, 1 % agarose gels were prepared in Tris-acetate-EDTA (TAE) buffer. For DNA purification from agarose gels, the Monarch DNA Gel Extraction Kit was used according to the manufacturer. A 2-Log DNA Ladder ranging from 0.1 – 10.0 kb (New England Biolabs) was added to each gel as a marker.

SDS-PAGE

Sodium dodecyl sulfate (SDS) gel electrophoresis of proteins was performed with a Mini-PROTEAN Tetra cell system (Bio-Rad) using 12 % Mini-PROTEAN TGX Precast Protein Gels (Bio-Rad). Protein extracts were mixed with equal volumes of Laemmli sample buffer (Sigma-Aldrich) and incubated at 95 °C for 5 min. After heating, samples were either frozen at -20 °C or freshly loaded onto gels. Gels were run with 1x Tris/Glycine/SDS buffer (Bio-Rad) for 45 min at 200 V. As a marker, PageRuler™ Plus Prestained Protein Ladder was loaded onto each gel.

Blue-Native PAGE

Blue-Native PAGE (BN-PAGE) was performed on XCell SureLock Mini-Cell Electrophoresis System (Thermo Fisher Scientific) using pre-cast Novex™ NativePAGE 3.12 % Bis-Tris protein gels (Thermo Fisher Scientific). Samples were mixed with 4x NativePAGE Sample Buffer (Thermo Fisher Scientific) and 35 µL were loaded on pre-cast 10-well gels. Anode and Light Blue Cathode Buffer were prepared according to the user's manual and gels were run for 2 h at 150 V.

Coomassie Staining

For protein stainings of BN-PAGE and SDS-PAGE gels, Bio-Safe™ Coomassie Stain (Bio-Rad) was used. Gels were washed twice for 5 min with deionized water, Coomassie stain was added to cover the gels and incubated for 30-60 min with gentle shaking. Coomassie solution was discarded and gels were washed with deionized water until protein bands became visible.

DAB-PB Staining

Diaminobenzidine (DAB)-enhanced Prussian Blue staining was adapted from Meguro et. al. with minor modifications (Meguro et al. 2007). Gels were washed twice with deionized water, incubated in freshly prepared 2 % potassium hexacyanoferrate (II) solution in 10 % HCl for 30-45 min at room temperature and again washed with deionized water for 3x 5 min. DAB-enhancement was done with a freshly prepared solution of PBS containing 0.025 % DAB and 0.005 % H_2O_2 for 30 min in the dark.

Silver Staining

For silver staining of SDS-gels the ProteoSilver™ Silver Stain Kit (Sigma-Aldrich) was used according to the manufacturer. Fixing solution and 30 % ethanol solution were prepared and stored at room temperature until use, sensitizer solution, silver solution and developer solution were prepared freshly before use. In brief, 50 ml fixing solution was added to the gel in a clean tray, heated in a microwave for 30 sec and incubated at room temperature for 5 min before decanting. The gel was washed with 50 ml 30 % EtOH solution for 10 min followed by three washing steps with ultrapure water. Then 50 ml sensitizer solution was added, the gel was heated in a microwave for 30 sec and incubated at room temperature for 2 min. Solution was decanted and gel was washed twice with ultrapure water, each time heating for 30 sec in a microwave and incubating for 2 min at room temperature. 50 ml silver solution was added, the gel was again heated for 30 sec and incubated for 2 min before washing with ultrapure water for 60 sec. The gel was developed by adding 50 ml developer solution and incubated for 3-5 min until the desired staining intensity was achieved. To stop the reaction, 5 ml of Stop solution

was added directly to the Developer solution, the gel was incubated for 5 min and then washed twice with ultrapure water.

2.2.3 Protein expression and purification

To express StrepTag-II tagged encapsulins in *E. coli* BL21(DE3), 0.5 ml lysogeny broth medium containing the appropriate antibiotics was inoculated at 37 °C. At an OD_{600} of about 0.6, protein expression was induced with 0.5 mM isopropyl-β-D-thiogalactopyranoside (IPTG) for 24 h at room temperature under constant shaking. Cultures were pelleted by centrifugation at 5000 rpm for 15 min and either stored at -20 °C or immediately lysed. For lysis, bacterial pellets were resuspended in cold lysis buffer (100 mM Tris-HCl, 150 mM NaCl) containing protease-inhibitor cocktail (Roche) and sonicated 4x 3 min on ice. The lysate was centrifuged at 15,000 g for 20 min and filtered through 0.22 µm syringe filters with PES membranes (Millex-GP).

StrepTag-II tagged encapsulins were purified from cleared *E. coli* lysate using 10 ml Strep-TactinXT Superflow high capacity column (IBA) according to the manufacturer.

FLAG-tag purification of encapsulins from HEK 293T (see chapter 2.3 for protein expression) was performed in batch format using Anti-FLAG M2 affinity gel (Sigma-Adrich) according to the manufacturer. In short, cleared cell lysate was incubated with pre-equilibrated resin for 2 h at 4 °C on a rotary shaker. Afterwards, the flow-through was collected and the resin was washed with five column volumes (CV) of TBS. To elute bound protein, the resin was incubated with 100 µg/ml of 3x FLAG tag peptide (Sigma-Aldrich) for 30 min at 4 °C on a rotary shaker before eluate was collected. Elution fractions were kept at 4 °C until further analysis.

2.2.3 Ferroxidase activity measurement

For ferroxidase activity measurements, cargo-loaded encapsulins were purified from HEK 293T cells as described earlier. Protein concentrations of both shell and cargo were determined densitometrical and 16 µM of QtIMEF or MxBCD inside the respective encapsulin shells were incubated with 50 Fe^{2+} per cargo in TBS buffer (pH 7.4). The absorption of Fe^{3+} was monitored at 350 nm for 20 min in a plate reader (SpectraMax M5, Molecular Devices). For background correction, the absorption of free iron in buffer was recorded in parallel and subtracted from all measured values.

2.3 Cell Culture Techniques

Human embryonic kidney cells (HEK 293T, ATCC: CRL-11268) were cultivated in advanced Dulbecco's modified Eagle's medium (DMEM, Thermo Fisher Scientific) supplemented with 10 % fetal bovine serum (FBS), 2 mM Glutamax (Thermo Fisher Scientific) and 100 U/ml penicillin/streptomycin solution (Thermo Fisher Scientific) at 37 °C in a humidified atmosphere containing 5 % CO_2. Cells were passaged using accutase solution (Sigma-Aldrich) for detachement, and the Countess™ II Automated Cell Counter (Thermo Fisher Scientific) was used to determine cell numbers for seeding.

2.3.1 Transient transfection and iron loading

Cells were transfected with X-tremeGENE HP (Roche) according to the manufacturer. DNA amounts of shell and cargo were kept constant in all transient transfections unless noted otherwise. To express recombinant encapsulins with cargo proteins, 70 % of the total DNA amount encoded the shell and 30 % encoded the respective cargo. For low-level Zip14 co-expression, the amount of shell DNA was reduced to 65 % and 5 % Zip14-DNA was used. For co-expression of two cargos, the amount shell DNA was 70 % and the DNA amount of each cargo was split equally.

Iron loading was facilitated by supplementing cell culture medium with freshly prepared ferrous ammonium sulfate (FAS) at the indicated concentrations 24 h after transfection.

2.3.2 Protein purification from cells

For protein purification or expression analysis, cells were harvested between 24 and 48 h after transfection and lysed using M-PER mammalian protein extraction reagent (Pierce Biotechnology) containing a mammalian protease-inhibitor cocktail (Roche). Cell debris was spun down at 10,000 g for 5 min and cleared lysates were kept at 4 °C until analysis. Protein concentration was either determined by measuring the absorbance at 280 nm or using the Pierce™ BCA Protein Assay Kit (Thermo Fisher Scientific) according to the manufacturer.

2.3.3 Quantification of cellular iron content

The iron content of cell lysates was quantified using a commercial Iron Assay Kit (Sigma-Aldrich) according to the manufacturer. In short, cleared cell supernatant was incubated with iron reducer solution for 30 min at room temperature to reduce Fe^{3+} to Fe^{2+} before the iron probe solution was added. The reaction was incubated for further 60 min at room temperature and absorbance was measured at 593 nm using a plate reader (SpectraMax

M5, Molecular Devices). To calculate iron concentrations, a standard curve was plotted for the range of 0−14 µM iron.

2.4 Imaging methods

2.4.1 Fluorescence microscopy

Fluorescence microscopy of cells was performed on an EVOS M5000 Imaging System (Thermo Fisher Scientific) equipped with the EVOS Light Cubes DAPI, GFP and RFP. Cells were either imaged live after changing the medium or fixed. For fixation, cells were washed twice with DPBS and incubated with 4 % paraformaldehyde solution in PBS for 10 min in the dark.

2.4.2 Magnetic resonance imaging

MR images were acquired with a Bruker BioSpec 94/20 USR, 9.4 T system equipped with an RF RES 400 1H 112/072 Quad TR AD resonator.

For relaxivity calculations of protein solutions, four different protein concentrations were measured in modified 384 well plates (Thermo Fisher Scientific). All wells surrounding a sample were filled with the corresponding sample buffer to allow for accurate buffer correction. T_2-measurements were performed using a multi-slice multi-echo (MSME) sequence with a repetition time (TR) of 6000 ms, 30 echoes, an echo spacing of 20 ms, a flip angle of 90°, a field of view of 60×60 mm and an image size of 256×256 pixels.

For T_2*-measurements performed on cell pellets, HEK 293T cells were transfected and incubated with FAS as described in chapter 2.3.1 for 48 h. Cells were washed with DPBS three times, detached with accutase solution and pelleted at 500 g for 4 min. Pellets were resuspended in 800 µl DPBS and transferred to cryobank vials (Thermo Fisher Scientific) containing 50 µL of hardened 1 % agarose. In the vials, cells were spun down for 2 min at 2,000 g to obtain a pellet on top of the agarose and immediately used for MRI. Measurements were performed in a custom-made holder filled with DPBS and higher order shims were used for all measurements. T_2*-values were calculated based on a multiple gradient echo (MGE) sequence with a TR of 800 ms, 12 echoes with an echo spacing of 4.5 ms, a flip angle of 50°, a field of view of 65×65 mm and an image size of 256×256 pixels. Relaxation times were calculated using the Image Sequence Analysis Tool from Bruker BioSpin MRI GmbH.

2.4.3 Magnetometry measurements

SQUID and VSM measurements were performed by Prof. Dr. Michael Winklhofer (Institute for Biological and Environmental Sciences, Carl von Ossietzky University Oldenburg) and Dr. Ulf Wiewald (Faculty of Physics and Center for Nanointegration (CENIDE), University of Duisburg-Essen).

2.4.4 Electron microscopy

Transmission electron microscopy was kindly performed by Martina Schifferer and Thomas Misgeld (German Center for Neurodegenerative Diseases, DZNE) as described in (Sigmund et al. 2019).

Cryo-electron microscopy reconstructions were kindly performed by Massimo Kube, Fabian Schneider and Hendrik Dietz (Laboratory for Biomolecular Design, Department of Physics, Technical University of Munich) as described in (Sigmund et al. 2019).

For manual segmentation of encapsulin particles in TEM images of cells, 100 particles were manually marked as regions of interest (ROI) and the diameters as well as the histograms of each nano-compartment were calculated using ImageJ.

Chapter 3| Results

The aim of this doctoral thesis was to develop and characterize interfaces for imaging and manipulation of cells. In the first part of this work, the possibility of transforming a pre-existing biologically relevant non-magnetic iron mineral into a magnetic iron mineral was assessed experimentally. In the next steps, a new encapsulin system was characterized and its applicability as an iron-biomineralizing protein nano-compartment for magnetic resonance imaging and magnetic manipulation of cells was evaluated. In addition, application of encapsulins for non-magnetic imaging methods such as electron microscopy was demonstrated.

In a preceding publication (Massner et al. 2018), we demonstrate that magnetoferritin, which is obtained by synthesizing magnetite under *in vitro* conditions inside the ferritin shell, can be used not only as a contrast agent for magnetic resonance imaging, but also as an actuator for cell ablation in magnetic hyperthermia. Our magnetic characterizations of magnetoferritin revealed an increase of more than 400 % in relaxivity r_2 per iron compared to ferritin, and MRI contrast obtained from cells was enhanced more than 80-fold upon receptor-mediated uptake and accumulation inside lysosomes. In addition, we were able to demonstrate sorting of magnetoferritin-containing cells in magnetic fields as well as ablation via magnetic hyperthermia, which demonstrated that magnetoferritin can also act as a biological interface to manipulate cells. However, while our results clearly suggested that magnetoferritin is suitable both as a contrast agent and as an actuator, its applicability as a genetic interface was severely limited by the *in vitro* synthesis of the magnetite core, which only allowed semi-genetic applications in combination with a ferritin uptake receptor. Thus, in the following chapter strategies will be evaluated to transform pre-existing ferrihydrite inside the ferritin shell into magnetite to generate a fully genetically encoded magnetic protein similar to magnetoferritin.

3.1 Reductive transformation of ferrihydrite

Ferrihydrite is among the first iron oxide phases to form in nature as it can rapidly precipitate from Fe^{3+} solutions, and as a thermodynamically unstable mineral it easily transforms into more stable iron oxides, thus serving as a precursor for better crystalline phases (Cornell und Schwertmann 2003; Cudennec und Lecerf 2006; Hansel et al. 2005). However, transformation reactions of iron oxides to magnetite usually involve elevated temperatures and basic pH and all of them are performed at anaerobic or microaerobic conditions (Cudennec und Lecerf 2006; Cornell und Schwertmann 2003; Hansel et al. 2005; Kukkadapu et al. 2003; Liu et al. 2007; Schwertmann und Murad 1983). Thus, possible transformations of ferrihydrite were studied under biologically relevant conditions in the following, most importantly under strictly aerobic conditions and at room temperature. Three different methods for converting ferrihydrite to magnetite based on pH, different reducing agents, or ascorbic acid (*asc*, vitamin C) are tested with naked ferrihydrite particles. In a second step, the possibility to transform the ferrihydrite core of ferritin is evaluated both *in vitro* and in cell culture to assess to possibility of magnetizing ferritin in a biologically relevant context.

3.1.1 Transformation of naked ferrihydrite particles

Ferrihydrite particles in a low nanometer size range were synthesized and provided in dried form by our project partners Carolin Hartmann and Natasha Ivleva (Institute of Hydrochemistry, TU Munich). Particle identity was confirmed by Raman micro-spectroscopy, Mössbauer spectroscopy and X-ray diffraction analysis (Hartmann et al. 2019). Raman spectroscopy measurements were performed by Carolin Hartmann (Institute of Hydrochemistry, TU Munich), SQUID and VSM measurements were performed by Dr. Ulf Wiedwald (Universität Duisburg-Essen).

pH-based changes in mineral phase

In a first test, triggering of ferrihydrite transformation was tested in acidic and basic conditions. pH is an important variable in the synthesis of iron nanoparticles, which usually occurs at slightly basic conditions. On the other hand, ferrihydrite was suggested to be degraded at acidic conditions in lysosomes when iron has to be mobilized *in vivo* (Lawrence und Zoncu 2019; Asano et al. 2011).

To test whether a pH-based transformation of ferrihydrite can occur, 10 mg ferrihydrite nanoparticles were mixed with different buffers in a pH-range of 4 to 9 either with or without an additional spiking of 50 mM ferrous ammonium sulfate (FAS) and incubated at room temperature in an overhead shaker. After four weeks, an aliquot was taken for Raman analysis. As can be seen in **Figure 2A**, all samples without FAS addition showed no transformation regardless of the pH, whereas samples with 50 mM FAS added showed clear changes in a pH range of 5-8. Ferrihydrite incubated at pH 5 with 50 mM FAS was transformed completely to lepidocrocite as indicated by the two prominent peaks around 250 cm^{-1} and 380 cm^{-1}. In contrast, ferrihydrite incubation at pH 7 or pH 8 with 50 mM FAS triggered the transformation to goethite with peaks at 300 cm^{-1} and 390 cm^{-1}. Interestingly, strongly acidic or basic conditions (pH 4 or 9) did not lead to a transformation, indicating a narrow pH tolerance.

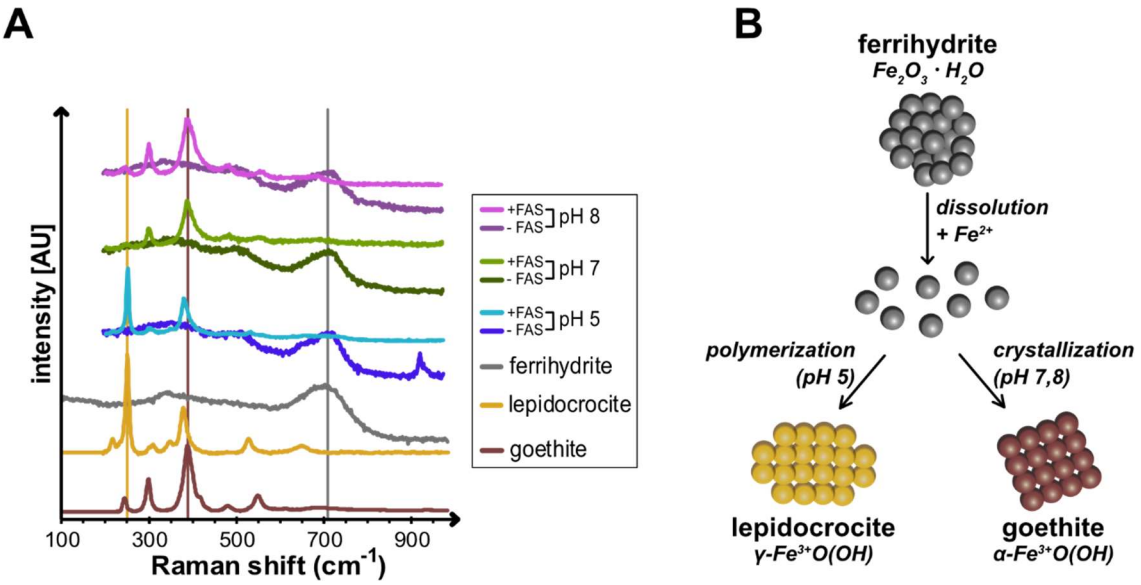

Figure 2| Raman analysis of naked iron particles.
Ferrihydrite particles with or without addition of 50 mM FAS were incubated at room temperature for four weeks at pH 5, 7, or 8 before analysis. **A)** Samples mixed with 50 mM FAS showed changes in Raman spectra indicating transformation of ferrihydrite to lepidocrocite (pH 5, blue curve) or goethite (pH 7 and 8, green and purple curves, respectively). Measurements were performed by Dr. Carolin Hartmann at the Institute of Hydrochemistry, TU München. (Hartmann 2019) **B)** Schematic of the proposed pH-dependent ferrihydrite transformation.

Reductive transformation triggered by reducing agents

The second hypothesis for ferrihydrite transformation to magnetite is based on the addition of reducing agents. As has been speculated for chitons, the only known aerobic organism where bio-organic magnetite synthesis was demonstrated (Lee et al. 1998; Nemoto et al. 2019), a partial reduction of ferric iron to ferrous iron on the surface could lead to a local mineral phase change from ferrihydrite (consisting only of ferric iron) to magnetite (consisting of a mixture of ferric and ferrous iron).

To test this hypothesis, 100 mM of different reducing agents were added to 10 mg ferrihydrite in 100 mM HEPES buffer pH 7.4 and incubated at room temperature for 21 days with sporadic mixing. The chosen reducing agents pyruvate, acetate, and lactate all have biological relevance, *e.g.*, as components in metabolic pathways or as building blocks for biosynthesis.

Addition of pyruvate or lactate did not lead to any changes in the Raman spectra, as can be seen in **Figure 3**. In contrast, ferrihydrite samples incubated with acetate showed a small shoulder in their Raman spectra at 665 cm^{-1}, which could indicate that a minor part of ferrihydrite was transformed to magnetite.

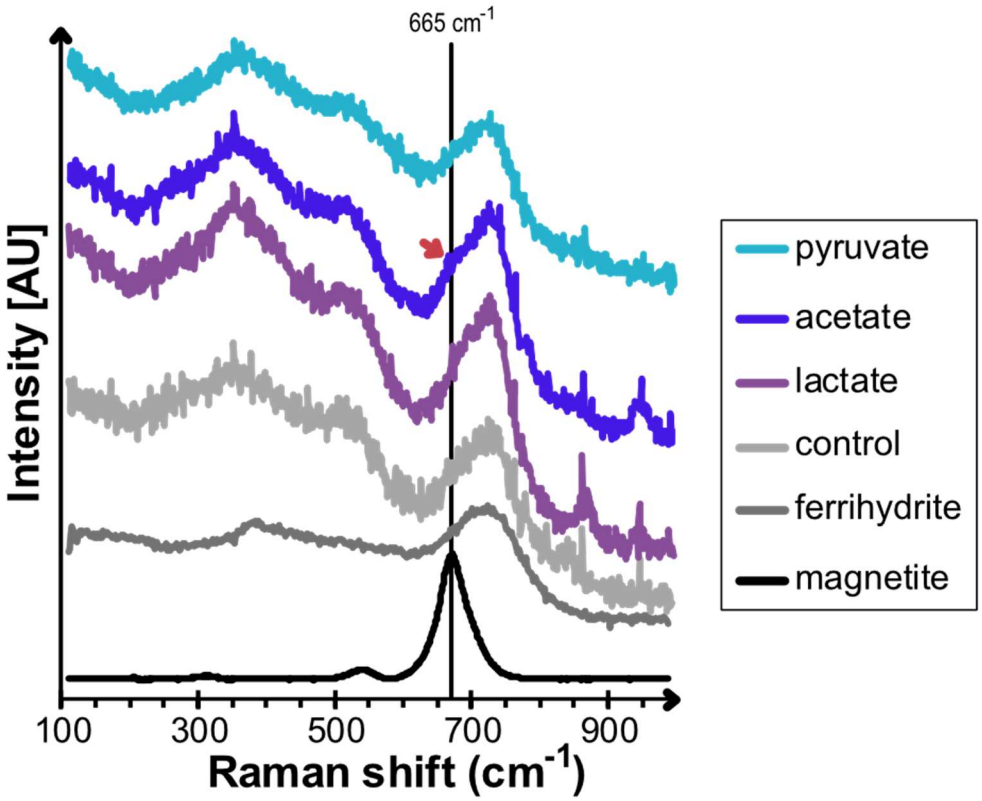

Figure 3| Raman analysis of naked iron mineral particles incubated with different reducing agents. Ferrihydrite particles (control, light grey) were incubated with 100 mM sodium pyruvate (light blue), sodium acetate (blue), or sodium lactate (purple) for 21 days at room temperature. Raman analysis showed a small shoulder at ~670 cm-1 (red arrow) after incubation with sodium acetate, whereas the mineral spectra did not change for the other conditions. Measurements were performed by Dr. Carolin Hartmann at the Institute of Hydrochemistry, TU München. (Hartmann 2019)

Reductive transformation via dual-purpose reducing agent and oxygen scavenger

As a third possibility to trigger the transformation of ferrihydrite to magnetite, the effect of ascorbic acid was evaluated. Ascorbic acid can have a dual function as a reducing agent acting directly on the iron mineral and as an oxygen scavenger decreasing the level of oxygen in the reaction mixture. As chemical synthesis of magnetite is performed under strictly anaerobic conditions (Cornell und Schwertmann 2003; Faivre 2016), a local reduction of oxygen levels could be beneficial for the process of reductive transformation.

To test this hypothesis, 10 mg ferrihydrite in 100 mM HEPES pH 7.4 were mixed with 100 mM *asc* and incubated at room temperature for 14 days before Raman and X-ray diffraction (XRD) measurements were performed in collaboration with Carolin Hartmann (TU Munich) and Dr. Damien Faivre (Max Planck Institute of Colloids and Interfaces), respectively. As can be seen in **Figure 4A**, addition of ascorbic acid (light blue curve) significantly changed the Raman spectrum compared to controls without *asc* (dark blue). While the peak at 715 cm^{-1} indicating the presence of ferrihydrite is still visible, it is significantly narrower which can indicate a higher order of crystallinity. Furthermore, a second peak at 665 cm^{-1} appeared after addition of *asc*, which is indicative of magnetite. Overall, the Raman analysis of ferrihydrite incubated with ascorbic acid hints at a partial transformation to magnetite. To further evaluate the mineral composition after incubation with ascorbic acid, X-ray diffraction measurements were performed (**Figure 4B**). Compared to untreated control particles, ferrihydrite treated with *asc* shows additional peaks at 13, 21, 24, 30, 37 and 47 nm^{-1} (indicated with red arrowheads), which can be attributed to magnetite.

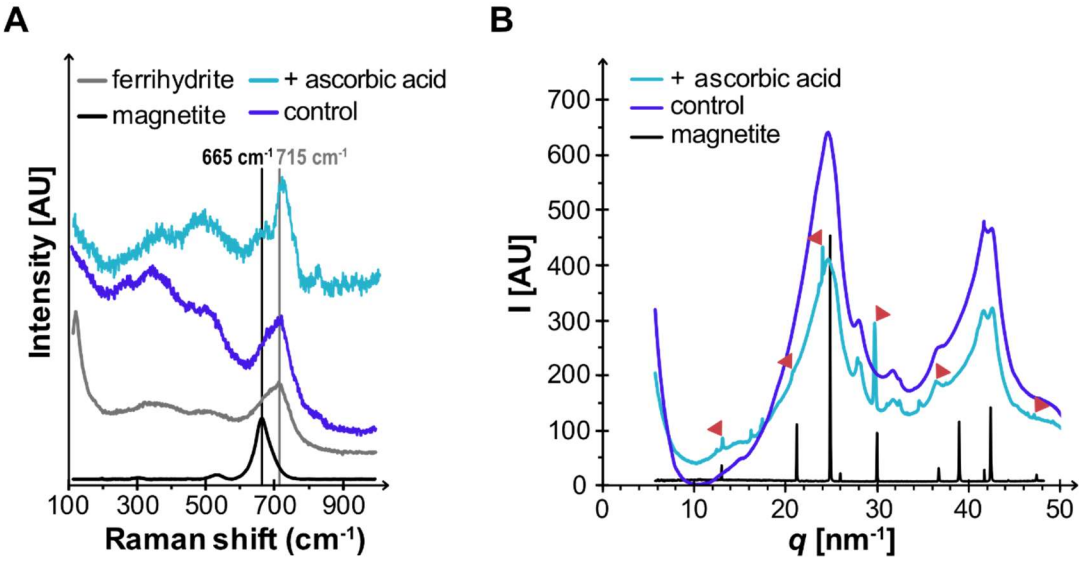

Figure 4| Mineral analysis of ferrihydrite particles treated with ascorbic acid.
10 mg of ferrihydrite particles were incubated with 100 mM ascorbic acid for 14 days at room temperature. **A)** Raman analysis of ferrihydrite particles incubated with ascorbic acid (light blue) showed an additional peak at ~665 cm-1 compared to a control sample (dark blue). Measurements were performed by Dr. Carolin Hartmann at the Institute of Hydrochemistry, TU München. **B)** X-ray diffraction (XRD) measurements showed additional peaks (red arrows) for ferrihydrite particles treated with ascorbic acid (light blue) compared to an untreated control sample (dark blue). XRD measurements were performed by Lucas Kuhrts.

In conclusion, it could be demonstrated that ferrihydrite is not an inert mineral and can be transformed to other iron oxide species under biologically relevant conditions. In particular, complete conversion to lepidocrocite or goethite can be triggered by pH-changes in the presence of additional ferrous iron. On the other hand, a partial transformation to magnetite was observed upon addition of reducing agents, and this effect could be further enhanced by using a combination of reducing agent and oxygen scavenger.

However, while these experiments demonstrate possible ways of modulating iron oxide nanoparticles, biologically relevant ferrihydrite is stored inside ferritin and thus covered by a protein shell. Thus, in the next chapter the possibility of transferring these findings to protein-encapsulated ferrihydrite particles is evaluated.

3.1.2 Transformation of ferrihydrite inside ferritin

As previously published, ferritin that is taken up in HEK 293T cells via the Tim-2 pathway accumulates in lysosomes (Massner et al. 2018), which are acidic cellular compartments with a pH of 4.5-5 (Lawrence und Zoncu 2019). Considering the mineral transformation of naked ferrihydrite particles to goethite and lepidocrocite at low pH described in the previous chapter, the fate of ferrihydrite stored inside ferritin accumulated in lysosomes was investigated in this chapter. To this end, an *in vitro* study of ferritin in lysosome-mimicking buffer was performed followed up by an analysis of purified lysosomes extracted from HEK 293T cells after long-term loading with ferritin. In addition, the effect of ascorbic acid as the most promising trigger of a transformation from ferrihydrite to magnetite was tested.

The effect of ascorbic acid on ferritin *in vitro*

In the previous chapter, ascorbic acid with its dual function as a reducing agent and an oxygen scavenger and its interaction with iron oxides has been shown to trigger a partial transformation from ferrihydrite to magnetite. To test the effect of *asc* on protein-encapsulated ferrihydrite, 3 mg/ml of either ferrihydrite-containing ferritin (eFtH+L) or iron-depleted apo-ferritin (apo-eFtH+L) from equine spleen were mixed with or without 100 mM ascorbic acid in 100 mM HEPES pH 7.4 and incubated for 5 h at 4 °C. Afterwards, samples were centrifuged and the supernatant was analyzed on Native PAGE regarding its protein and iron content.

Incubation with ascorbic acid did not lead to protein losses compared to an untreated control condition as can be seen by the Coomassie protein stain on Native PAGE (**Figure 5A**, upper panel), indicating that the highly stable ferritin is not affected on a protein level. However, iron staining of the gel revealed that ferritin incubated with *asc* lost its iron mineral core at least partially, which is in accordance with the visual evidence of a large brown pellet and the decoloring of the originally amber protein solution (**Figure 5A**, middle and bottom panels).

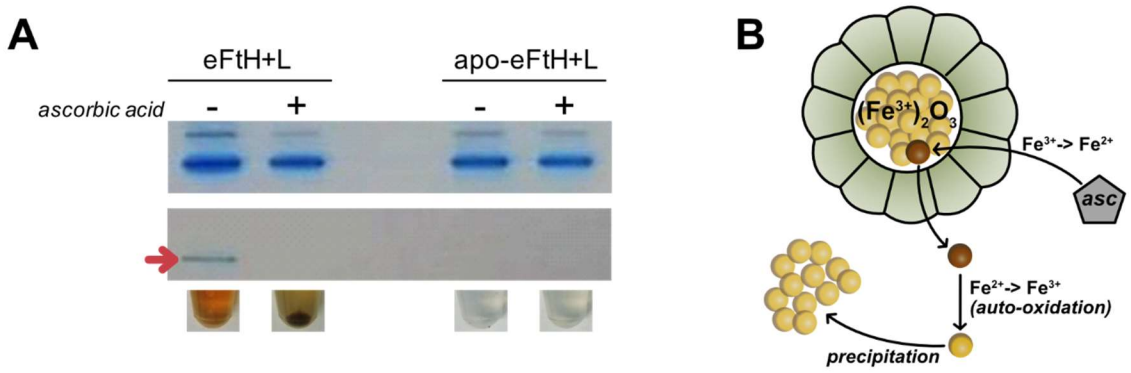

Figure 5| The effect of ascorbic acid treatment on iron-loaded ferritin.
Ferritin or apo-ferritin were mixed with or without ascorbic acid and incubated for 4 h at 4 °C. **A)** Native PAGE analysis showed no protein losses (Coomassie, upper panel, whereas the iron staining (Prussian Blue stain, middle panel) clearly indicated a loss of iron after incubation with asc compared to the control (red arrow). The bottom panel shows a large brown pellet for ferritin incubated with asc after centrifugation. **B)** Schematic of the proposed effect of ascorbic acid on ferritin. Asc can reduce ferric iron bound in the ferrihydrite core, the generated ferrous iron leaves the ferritin shell and auto-oxidizes to ferric iron in the buffer solution, which leads to precipitation of an insoluble iron-oxide outside the shell.

Effects of lysosomal environment on ferritin in an *in vitro* simulation

The aggregation of iron atoms outside the ferritin protein shell after partial mineral degradation triggered by ascorbic acid seems to interfere with a direct transformation of ferrihydrite inside ferritin. However, as ferritin can be accumulated in lysosomes (Massner et al. 2018) which are known to have an acidic pH, the effects of such an environment on the stability of both protein shell and iron mineral were evaluated.

To mimic the lysosomal environment *in vitro*, an artificial lysosomal fluid (ALF) buffer was prepared based on [ref]. 3.4 mg/ml ferritin was dialyzed for 24 h against either ALF pH 4.6 or pH 7.4 as a control and centrifuged afterwards. Protein concentration determination of the supernatant after dialysis revealed that 89 % of initial protein could be recovered after incubation at neutral pH, whereas 83 % were recovered after incubation at acidic pH (**Figure 6A**). In addition, centrifugation yielded a brown pellet after incubation at acidic pH, while no pellet was visible for samples incubated at neutral pH. Further native PAGE analysis of the supernatant with an adjusted protein concentration of 1 mg/ml revealed that ferritin incubated at pH 4.6 shows a weaker signal in Prussian Blue staining and DAB-enhancement compared to control conditions (**Figure 6B**), indicating a loss of iron inside the ferritin protein shell.

To further investigate whether the acidic artificial lysosomal environment could have a potential effect on the iron oxide species precipitating outside the protein shell, ferritin was incubated in ALF buffer pH 4.6 for 11 or 27 days and centrifuged to obtain pellets. While a Raman analysis of these pellets was not possible due to low signal and strong background, magnetometry measurements on a superconducting quantum interference device (SQUID) performed in collaboration with Dr. Ulf Wiedwald (University of Duisburg-

Essen) gave a weak but analyzable signal. Zero-field-cooling / field-cooling (ZFC/FC) curves (**Figure 6C**) showed a maximum at blocking temperatures T_B of 9 K and 12 K for 11 and 27 days, respectively. The narrow peaks at T_B indicate a moderate particle size distribution, and the negative shift of both curves can be ascribed to diamagnetic properties of the material. Magnetization curves indicate superparamagnetic behavior and a coercivity H_C at 2 K of 39 mT and 62 mT after 11 and 27 days of incubation, respectively.

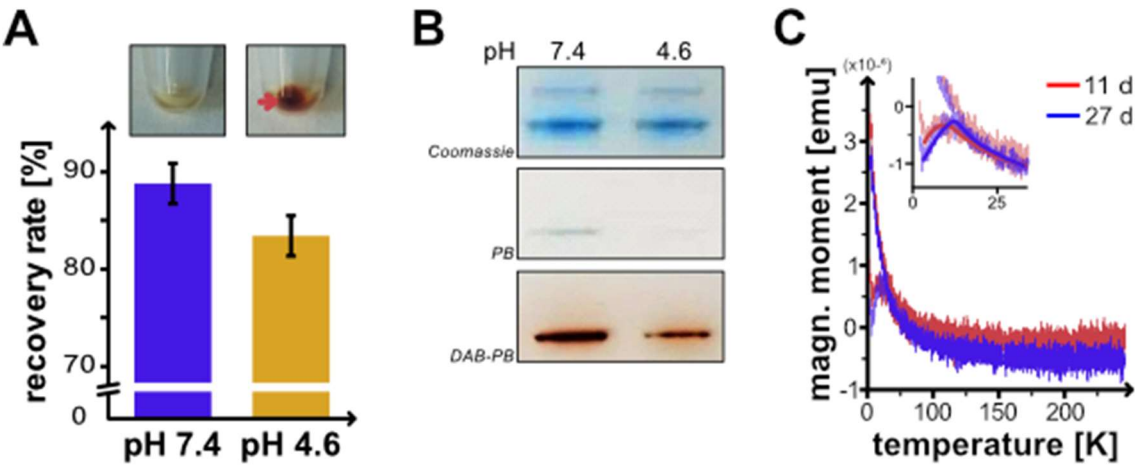

Figure 6| Effect of *in vitro* simulated lysosomal environment on ferritin.
A) 3.4 mg/ml ferritin solution was dialyzed against 1 L ALF buffer pH 7.4 or pH 4.6 for 24 h at 4 °C. Experiments were performed as n = 3 technical replicates. After incubation at pH 7.4 about 89 % of total protein could be recovered (blue), whereas recovery rates dropped to 83 % after incubation at pH 4.6 (orange). Inserts above the graph show a small pellet after centrifugation of the sample at pH 4.6 (red arrow). **B)** Native PAGE analysis of supernatants shows reduced iron loading of ferritin after incubation at pH 4.6 (top panel, Coomassie stain; middle panel, Prussian Blue stain; bottom panel, DAB-enhancement). 1 mg/ml ferritin was applied on all lanes. **C)** ZFC/FC curves of the pellets measured at 10 mT show a narrow peak with a TB of 9 K and 12 K after incubation for 11 and 27 days, respectively. Inset shows a zoom-in at the peak region. Measurement was performed by Dr. Ulf Wiedwald (Universität Duisburg-Essen).

Analysis of purified lysosomes after long-term loading with ferritin

While the ALF buffer mimics the chemical composition of the lysosomal lumen, this simulation of a lysosomal environment lacks the proteinaceous components of these organelles as well as the spatial restraints of about 1 µm / 0.5 $µm^3$ (Lawrence und Zoncu 2019). Thus, the effect of long-term ferritin accumulation on the magnetic properties of ferrihydrite in lysosomes was studied in mammalian cells.

HEK 293T cells stably expressing the ferritin receptor Tim-2 were supplemented with 300 µg/ml ferritin over 27 days and intact lysosomes were prepared for analysis. Raman spectra of lysosomes isolated from treated and untreated control cells showed peaks indicative of a complex biological sample, such as peaks for amino acids tyrosine, tryptophan and phenylalanine and for N-Cα-C or C-H stretches, as well as bands for primary and tertiary amides. The spectrum for lysosomes from ferritin-supplemented cells shows an additional band at 715 cm^{-1} not present in the control sample, which could be attributed to ferrihydrite (**Figure 7A**). However, the band is only weak, which could be

due to an unfavorable ratio of ferrihydrite compared to biological matrix in the sample. Therefore, magnetic measurements on a SQUID were performed in addition to gain more information about the magnetic properties of lysosomes. The ZFC/FC curves of lysosomes purified from similarly treated cells show a widened peak at T_B = 15 K indicating that the measured particles have a spread in size distribution. In addition, the curve is split up to a T_B of ~100 K (**Figure 7B**), which indicates the presence of larger particles or agglomerates.

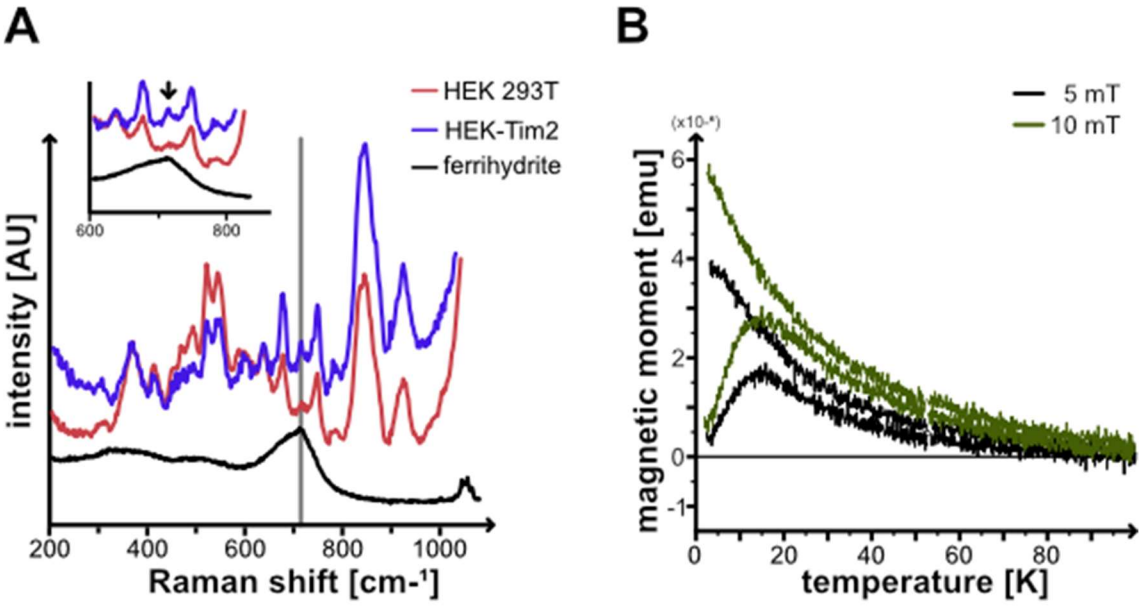

Figure 7| Analysis of lysosomes purified from HEK 293T cells after long-term ferritin supplementation.
Cells stably expressing Tim-2 were supplemented with 300 µg/ml ferritin for 27 days before lysosomes were isolated. **A)** Raman analysis of purified lysosomes show a small peak at 715 cm-1 compared to untreated cells indicative of ferrihydrite. Measurements were performed by Dr. Carolin Hartmann at the Institute of Hydrochemistry, TU München. **B)** ZFC/FC curves of lysosomes show a TB peak at 15 K with a curve splitting up to a TB of 100 K, indicating the presence of larger particles or agglomerates. Measurement was performed by Dr. Ulf Wiedwald (Universität Duisburg-Essen).

In conclusion, the work presented in this chapter indicates that a partial reductive transformation of naked ferrihydrite particles to magnetite is possible under aerobic conditions and ambient temperatures in the presence of a suitable reducing agent, such as ascorbic acid. However, it proved to be difficult to transfer these findings to protein-encapsulated ferrihydrite particles as diffusion of mobilized ferrous iron led to unwanted precipitation of iron oxides outside the protein shell and magnetite nucleation could not be induced. Similar problems occurred when using lysosomes as a biologically defined compartment for iron mineralization, as iron metabolism is tightly controlled in cells and a strict control of precise reaction conditions is difficult on a cellular level without a number of intrusive modifications. While a chemically triggered transformation of ferrihydrite in biological contexts seems to be complicated and hard to control, it stands to reason that an enzymatic solution could be desirable as sub-cellular enzyme localizations can be controlled on a genetic level, and thus introducing an enzyme to catalyze the reduction of ferric iron in ferrihydrite could aid potential transformation

processes. However, the ferritin cavity is too small to allow protein incorporation in this context, and a genetic targeting of cargo inside ferritin would only be possible by rationally designed fusion constructs which would require extensive screening for possible altered functionality. Thus, a relatively new class of large proteinaceous nano-compartments called encapsulins were investigated for their potential to incorporate iron in the following chapter.

3.2 Characterization of the Qt encapsulin system

Encapsulins, which were originally characterized as bacteriocins or proteases (Valdés-Stauber und Scherer 1994; Hicks et al. 1998), are proteinaceous nano-compartments found in bacteria and archaea consisting of a shell with HK97-like fold and cargo proteins targeted to the lumen via short C-terminal peptide targeting sequences (Giessen 2016; Sutter et al. 2008; McHugh et al. 2014). The first discovered cargo proteins were either ferritin-like proteins (Flp) or DyP-type peroxidases (Rahmanpour und Bugg 2013; Sutter et al. 2008), and while still little is known about the biological role of encapsulins, they are attributed roles in iron oxidation and detoxification as well as other redox processes and degradation activities (Giessen 2016; McHugh et al. 2014; Sutter et al. 2008).

In this chapter, the encapsulin compartment of the soil bacterium Quasibacillus thermotolerans (Qt) is characterized in detail for the first time (Sigmund et al. 2019). In particular, the system was transferred to mammalian cells and the structure was solved using Cryo-electron microscopy. In addition, the function of the native cargo was analyzed and comparisons to already published encapsulin systems were drawn.

3.2.1 Expression in mammalian cells

In order to express the encapsulin system of *Quasibacillus thermotolerans* in mammalian cells, expression constructs were generated containing either the shell protein QtEnc fused with a C-terminal FLAG affinity tag (QtEnc-FLAG) or the cargo protein QtIMEF including the internal C-terminal targeting peptide QtSig (**Figure 8A**).

To test assembly and cargo-targeting in mammalian cells, the shell and cargo proteins QtEnc-FLAG + QtIMEF were co-expressed in HEK 293T cells. Blue Native-PAGE (BN-PAGE) analysis of cell lysates revealed a sharp, high molecular weight band above 1.2 MDa, which runs higher than the protein band corresponding to T = 3 *Myxococcus xanthus* encapsulin (MxEnc) (**Figure 8B**). In addition, SDS-PAGE analysis after FLAG-pulldown revealed that QtEnc and QtIMEF co-precipitate running at 32 and 23 kDa respectively, which proves that cargo targeting inside the shell via the internal QtSig sequence is successful (**Figure 8C**). In addition, densitometric analysis revealed that 51 ± 1 % of total protein accounted for the shell and 49 ± 1 % for the cargo. DLS

measurements of empty and cargo-filled particles gave narrow size distribution histograms with average sizes of 39 and 40 nm for QtEnc and QtEnc + QtIMEF, respectively (**Figure 8D**). Taken together, these results clearly indicate that QtEnc self-assembly as well as auto-targeting and encapsulation of the QtIMEF cargo protein work in HEK 293T cells, demonstrating a successful transfer of the Qt encapsulin system from the original bacterial organism to a mammalian model system.

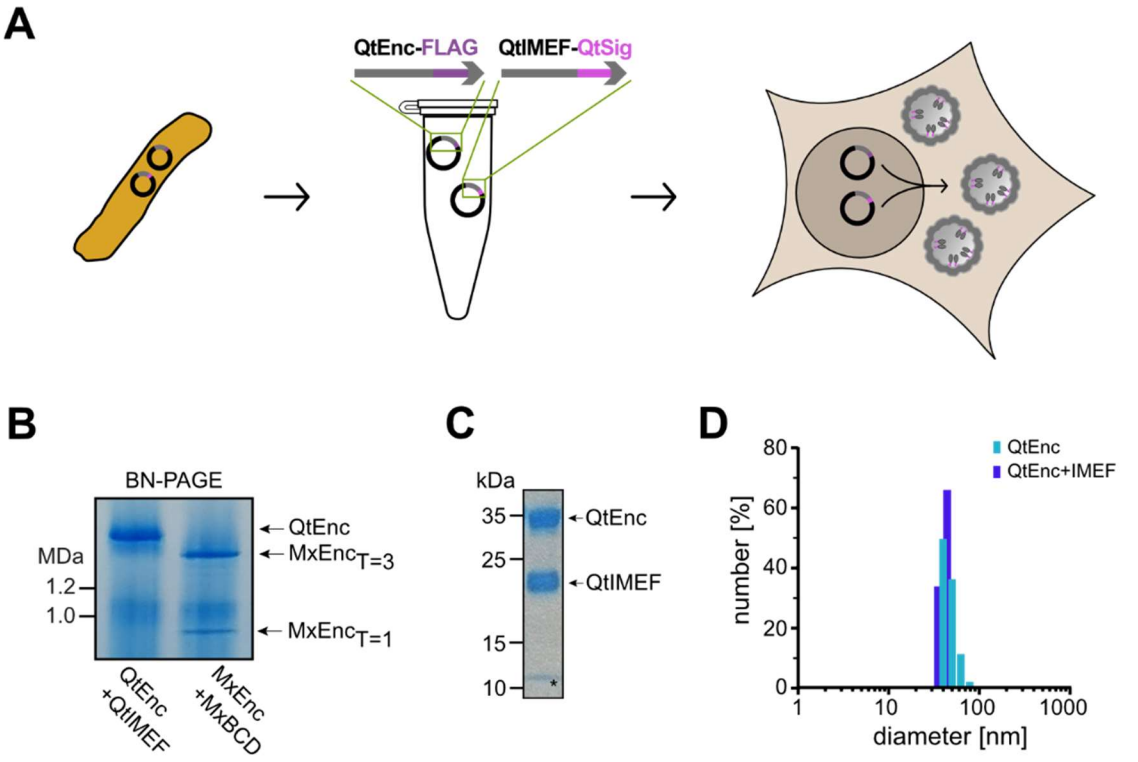

Figure 8| Expression of the Qt encapsulin system in mammalian cells.
A) Mammalian gene expression constructs encoding for the Quasibacillus thermotolerans (Qt) encapsulin system were generated consisting of the encapsulin shell fused to a C-terminal FLAG-tag (QtEnc-FLAG) and the cargo protein containing an internal C-terminal auto-targeting peptide sequence (QtIMEF-QtSig). **B)** Cell lysates of HEK 293T cells expressing the Qt encapsulin system were analyzed on Blue Native-PAGE stained for protein with Coomassie. A high molecular weight band above 1.2 MDa was found. **C)** Coomassie-stained SDS-PAGE of QtEnc-FLAG+QtIMEF purified via FLAG-pulldown showed a band at ~35 kDa for QtEnc and another band at ~23 kDa for QtIMEF co-precipitating with the shell. **D)** DLS measurements of empty QtEnc shells and QtEnc+QtIMEF gave a narrow size distribution histogram with average diameters of 39 and 40 nm for QtEnc and QtEnc+QtIMEF, respectively. Data were published in (Sigmund et al. 2019).

3.2.2 Structural analysis

The first high-resolution structure of an encapsulin has already been published a decade ago (Akita et al. 2007), and several other encapsulin structures have been added to the protein data base in the meantime which where all classified as icosahedral structures with triangulation numbers of either T = 1 or T = 3 (Sutter et al. 2008; Giessen et al. 2019; McHugh et al. 2014; Lončar Nikola et al. 2020; Nichols et al. 2020). However, the

biochemical data obtained in the previous chapter suggest that the Qt encapsulin could have a different icosahedral symmetry, and thus its structure was studied in more detail using cryo-electron microscopy in cooperation with the group of Prof. Dr. Hendrik Dietz (Laboratory for Biomolecular Design, Department of Physics, Technical University of Munich). As the encapsulin system is of bacterial origin and has been transferred to a mammalian system, both particles expressed in bacteria and in mammalian cells were analyzed and compared.

While several T = 1 and T = 3 encapsulins have been described in literature (Akita et al. 2007; McHugh et al. 2014; Sutter et al. 2008; Rahmanpour und Bugg 2013; Rosenkrands et al. 1998; Rurup et al. 2014; Valdés-Stauber und Scherer 1994; Hicks et al. 1998), the Qt encapsulin is the first to be reported with a T = 4 icosahedral symmetry. A comparison of MxEnc as a representative of the T = 3 encapsulin class and the T = 4 QtEnc shows several differences in the overall architecture of these encapsulins (Sigmund et al. 2019; Giessen et al. 2019) (**Figure 9**). In the T = 4 QtEnc, the asymmetric unit consists of three hexameric monomers and one pentameric monomer color-coded blue, green and light and dark purple in **Figure 9B**; thus the QtEnc monomer can take on four different conformations in total compared to three conformations in MxEnc (blue, light and dark purple). In both encapsulins, the five-fold symmetry axes are located at the center of the pentamers, while the localization of the other two symmetry axes differ. In QtEnc, the center of each hexamer represents a two-fold symmetry axis corresponding to an icosahedral edge, with the three-fold symmetry axis located at the conjunction of three hexamers. In contrast, the centers of hexameric capsomers in MxEnc correspond to three-fold symmetry axes, while the two-fold symmetry axes are located at the interface between two hexamers.

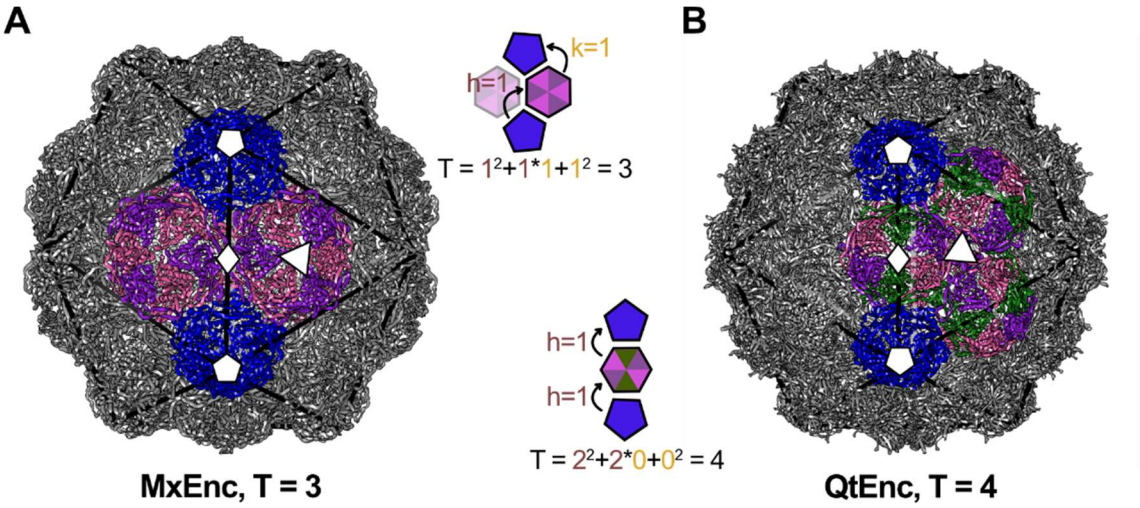

Figure 9| Architecture of T=3 and T=4 encapsulins.
Surface view of the T=3 Mx encapsulin **(A)** and the T=4 Qt encapsulin **(B)** centered on two-fold axes. The icosahedral facets drawn in black lines highlight the overall icosahedral symmetry. Five-fold, three-fold and two-fold symmetry axes are indicated with pentagon, triangle and diamond symbols, respectively. Two pentamers are highlighted dark blue and adjacent hexamers are highlighted light and dark purple and dark green according to their subunit-composition. Structures were adapted from PDB entries [xxx] and rendered in Chimera. The schematics are colored analogous and illustrate the calculation of the triangulation numbers for MxEnc (top) and QtEnc (bottom). Structures were adapted from PDB: 4PT2 and (Sigmund et al. 2019).

For cryo-EM analysis, Qt encapsulin particles with co-expressed QtIMEF cargo were affinity-purified from either *E. coli* BL21(DE3) or HEK 293T cells *via* Strep-Tag II or FLAG-Tag, respectively. Electron density maps with resolutions of 6 and 4.5 Å for particles from HEK cells and *E.coli*, respectively, showed a T = 4 icosahedral structure made up of 12 pentamers and 30 hexamers with four different monomer conformations distinguishable (**Figure 9B**, **Figure 10A**). The cutaway views revealed additional cargo densities inside the cavities corresponding to the QtIMEF cargo molecules docked inside the shell (**Figure 10B**). These cargo densities were located at the five-fold and two-fold symmetry axes with a distance of 2.5 nm from the shell, as indicated in the figure. Outer and inner diameters determined in slice representations (**Figure 10C**) revealed that encapsulins expressed in both bacterial and mammalian organisms have the same dimensions, with an outer diameter of 40 to 43 nm measured through two-fold and five-fold symmetry axes, respectively, and an inner diameter of 30 nm. Overall, no differences could be determined between particles originating from the two different sources, which is a strong indication that the encapsulin system could be transferred to mammalian organisms without negative impact on structural level.

Further analysis of the electron density maps at the symmetry axes revealed two putative pore regions (Sigmund et al. 2019). The centers of pentameric capsomers, which represent the five-fold symmetry axes, showed a circular electron-sparse region with an apparent diameter of 1 nm. In addition, the three-fold symmetry centers at the interface of three hexamers formed a potential triangular-shaped pore of about 1 nm. In contrast, the two-fold axes at the hexameric centers are unlikely to contain a pore region, as their electron-sparse cleft seems to be closed by opposing monomer residues.

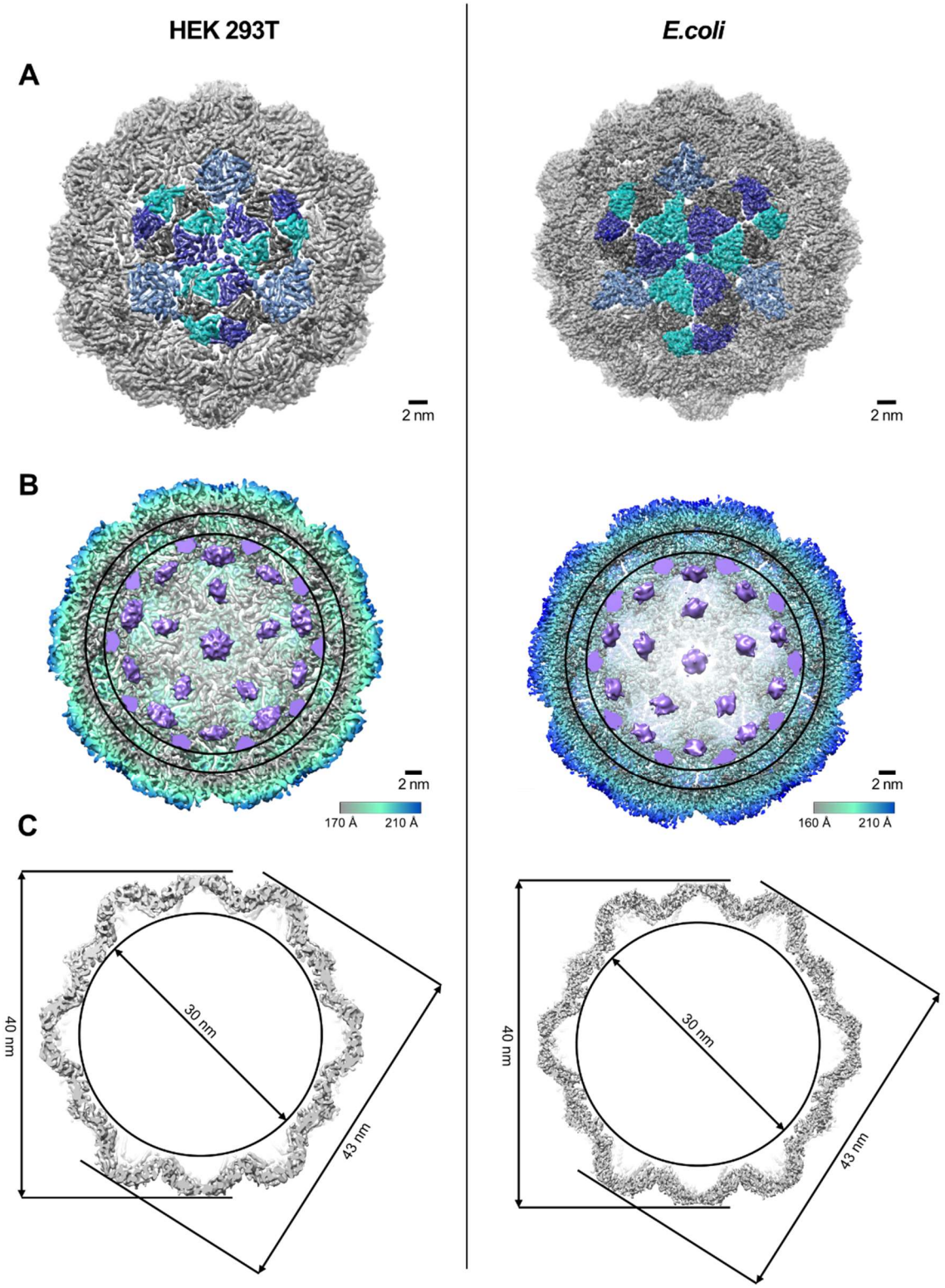

Figure 10| Cryo-EM analysis of Qt encapsulin expressed in mammalian cells and *E. coli*.
QtEnc + QtIMEF was purified via FLAG-affinity purification (HEK 293T, left column) or Strep-Tag II affinity purification (E. coli, right column). **A)** Segmented electron density of the encapsulin system purified from HEK 293T (left) or E. coli BL21(DE3) (right). The four different monomer conformations are color-coded according to their interconnectivity. **B)** The cutaway views through the maximum diameter of QtEnc (43 nm) show cargo densities (purple) at 2.5 nm distance from the shell as indicated by the two circles. **C)** Slice representations through the center of QtEnc show that particles from both HEK cells and E. coli have the same dimensions, with outer diameters of 40-43 nm and an inner diameter of 30 nm. Data were published in (Sigmund et al. 2019). Data were published in (Sigmund et al. 2019).

3.2.3 QtIMEF cargo functionality

The Qt encapsulin cargo QtIMEF has been described as a member of the ferritin-like protein superfamily with a four-helix bundle fold and iron-binding capacities despite lacking typical ferroxidase motifs (Giessen et al. 2019; Giessen und Silver 2017; Andrews 2010). Instead, a di-nuclear ferroxidase site is formed at the interface of two IMEF dimers coordinating two Fe atoms, representing an inter-subunit ferroxidase center (Giessen et al. 2019). However, iron mineralization mediated by QtIMEF has only been tested in *E. coli* so far, thus the functionality of the QtEnc + QtIMEF system in or derived from mammalian cells was studied and compared to the well-known iron biomineralizing capabilities of MxEnc.

Iron storage capacity of encapsulin systems

The theoretical iron storage capacity χ of encapsulins, assuming ferrihydrite is the iron oxide species formed, was calculated according to

$$\chi = V_{apo} \cdot \frac{\rho}{M_{Fh}} \cdot 2 \cdot N_A = \frac{1}{6} \cdot \pi \cdot d_{cavity}^3 \cdot \frac{\rho}{M_{Fh}} \cdot N_{Fe} \cdot N_A \qquad (1)$$

where d_{cavi}^3 is the inner diameter of the encapsulin shell, π is Archimedes' constant pi, ρ is the density of ferrihydrite, M_{Fh} is the molecular weight of ferrihydrite, N_{Fe} is the number of iron atoms per nm^3 in ferrihydrite, and N_A is the Avogadro constant. Details on the calculation can be found in **Table 2**. Based on equation (1), the maximum iron storage capacity was calculated as 380,000 and 200,000 Fe/protein for QtEnc and MxEnc, respectively, whereas ferritin has a theoretical iron storage capacity of 4900 Fe/protein.

To quantify the iron storage capacities under cellular conditions, both encapsulin systems were purified from HEK 293T treated with 2 mM FAS for 36 h and the iron content was quantified using ICP-MS. The total amount of iron per encapsulin (χ_{cell}) was determined as 35,097 ± 853 Fe/protein for QtEnc + QtIMEF and 18,856 ± 807 Fe/protein for MxEnc + MxBCD. Ferritin, in comparison, has been reported to load ~1,200 – 2,500 Fe/protein under native conditions [ref] and was measured to contain 1,800 Fe/protein.

Table 2| Calculation of the theoretical iron storage capacities of QtEnc, MxEnc and ferritin.

	d_{cavity}^3	$\rho\ [\frac{g}{nm^3}]$	$M_{Fh}\ [\frac{g}{mol}]$	N_{Fe}	χ	χ_{cell}
QtEnc	30	$3.8 \cdot 10^{-21}$	168.7	2	383,532	35,097
MxEnc	24				196,368	18,856
ferritin	7				4,872	1,800

Ferroxidase assay

The iron biomineralization efficiency of encapsulins was characterized *in vitro* using a spectroscopic ferroxidase assay [ref] performed with QtEnc + QtIMEF and MxEnc + MxBCD affinity-purified from HEK 293T cells (**Figure 11A**). To this end, 50 Fe^{2+} per cargo protein were added to either encapsulin system and the absorbance was monitored at 350 nm for 20 min. These absorbance traces were then corrected for iron-autooxidation by subtracting the absorbance trace of free Fe^{2+}. For QtEnc + QtIMEF, a fast initial increase in absorbance was observed, which could be monitored only partially due to a dead time of ~1 min for pipetting and mixing of the reaction. After 5 min, a plateau was reached which was stable for the remaining reaction time. In contrast, a delay of ~6 min was observed for MxEnc + MxBCD before the absorbance increased, and a stable plateau was reached only after 15 min.

Encapsulin iron loading in cells

While iron is readily available in *in vitro* ferroxidase assays on purified proteins, iron biomineralization in cells is hampered as iron is highly regulated on cellular level and can cause significant cellular stress due to the generation of reactive oxygen species. Therefore, the ferrous iron transporter Zip14 was co-expressed together with either the Qt or Mx encapsulin system in a sub-set of the following cell culture experiments to increase the amount of ferrous iron available in the cytosol for encapsulin-dependent biomineralization (**Figure 11B**). To analyze encapsulin-dependent iron biomineralization, cells co-expressing either QtEnc + QtIMEF or MxEnc + MxBCD with or without additional Zip14 were treated with different amounts of FAS for 36 h and the soluble lysate was analyzed with Blue Native-PAGE (**Figure 11C**, upper panels). DAB-enhanced Prussian Blue staining of the gels allowed to visualize the iron content both of encapsulins as well as ferritin as the endogenous iron storage system. Without co-expression of the Zip14 transporter, the Qt encapsulin system showed iron loading already at the lowest FAS supplementation (0.125 mM), whereas Mx encapsulin showed no iron loading for all tested FAS concentrations under this condition. Notably, endogenous ferritin was iron loaded at all FAS concentrations when the Mx encapsulin system was expressed, while the ferritin bands are significantly weaker when co-expressing Qt encapsulin. This indicates that the Qt encapsulin system can compete with endogenous ferritin for iron at low iron concentrations. Upon co-expression of Zip14, iron loading of Mx encapsulin can be detected starting at FAS supplementations of 0.5 mM [Sigmund 2017], whereas the Qt encapsulin system again shows clear iron bands at the lowest FAS supplementation (0.125 mM) (**Figure 11C**, bottom panels). As before, endogenous ferritin is strongly iron-loaded despite expression of MxEnc + MxBCD at all FAS supplementations, whereas expression of the Qt encapsulin system reduces the iron loading of ferritin, again indicating that QtEnc + QtIMEF can compete for bioavailable iron with the endogenous iron storage system.

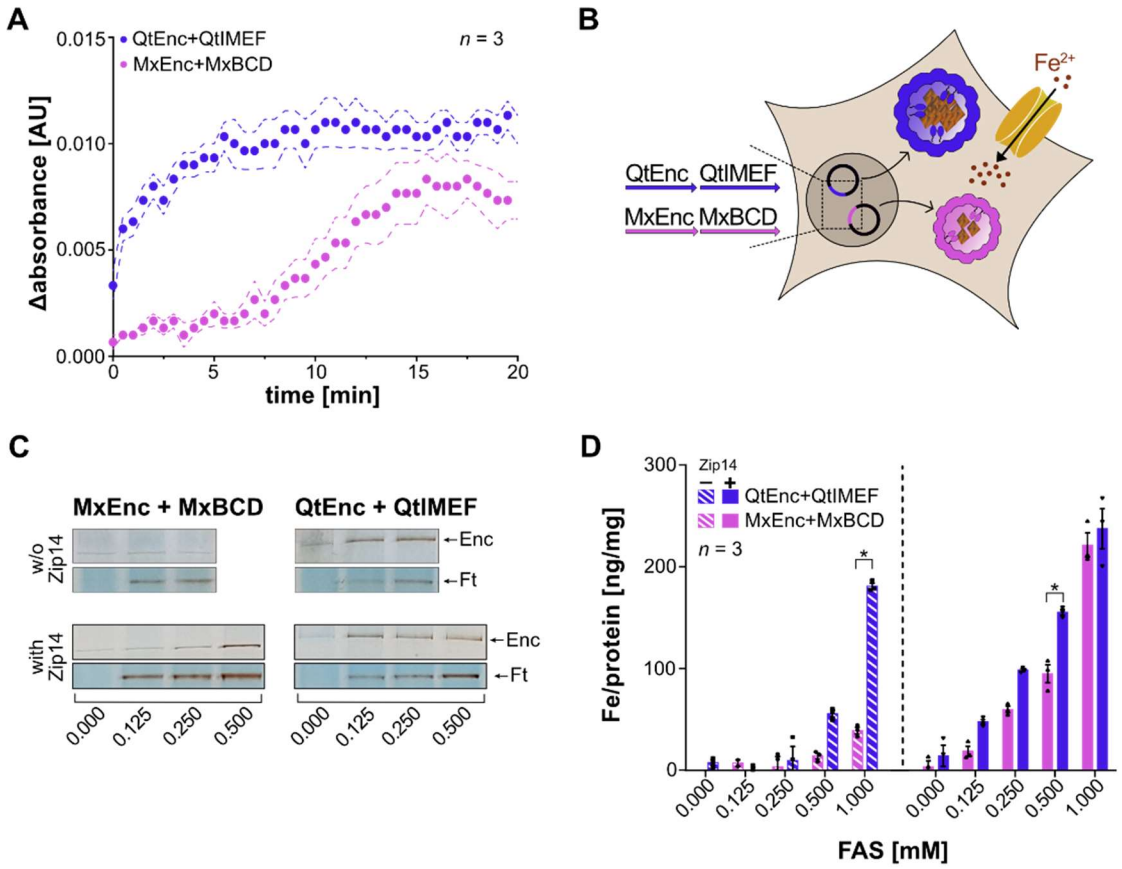

Figure 11| Characterization of QtIMEF-mediated iron biomineralization.
A) The encapsulin systems QtEnc + QtIMEF and MxEnc + MxBCD were purified from HEK 293 cells and iron biomineralization was monitored spectroscopically. 50 Fe2+ ions were added to 16 µM of either cargo system was recorded at 350 nm for 20 min. **B)** Schematic of iron biomineralization inside encapsulins in cells co-expressing iron importer Zip14. **C)** Analysis of DAB-enhanced Prussian Blue stained Blue-Native gels loaded with lysates of cells expressing either encapsulin system with or without additional upregulation of Zip14. Cells were supplemented with the indicated amount of FAS for 36 h prior to lysis. Bands for encapsulins (Enc) and the native iron storage protein ferritin (Ft) are indicated with arrows. **D)** Analysis of cellular iron content after expression of either Mx (purple) or Qt (blue) encapsulin system with or without co-expression of Zip14. Stars indicate p-values <0.05 in two-way ANOVA tests. n = 3 independent biological replicates. Data were published in (Sigmund et al. 2019).

To quantify the effect of encapsulin iron biomineralization on the total cellular iron content, a colorimetric iron assay was performed on cells lysed after 36 h of FAS treatment (**Figure 11D**, left). In the absence of Zip14, cells co-expressing QtEnc and QtIMEF showed a significant increase in total iron starting at 0.5 mM FAS compared to untreated control cells (2-way ANOVA, $p < 0.05$), whereas cells expressing the Mx encapsulin system showed significant iron accumulation only at the highest FAS level (1.0 mM). In addition, cells expressing the Qt encapsulin showed higher absolute levels of iron accumulation compared to cells expressing Mx encapsulin. These results indicate that Qt encapsulin can accumulate iron more efficient at low iron availability. Upon co-expression of Zip14, cells expressing either of the two encapsulin systems showed significant iron accumulation starting at 0.25 mM FAS and differences in the level of iron accumulation could only be observed for 0.5 mM FAS, whereas a higher FAS

concentration led to comparable absolute amounts of iron accumulation (**Figure 11D**, right).

3.2.4 Cargo encapsulation in QtEnc and MxEnc

Various encapsulin cargo proteins have been identified so far, and their terminal targeting peptides have been shown to be highly conserved among different classes of encapsulins and cargo types (Giessen und Silver 2017; Sutter et al. 2008; McHugh et al. 2014; Rahmanpour und Bugg 2013). In addition, it has been shown that artificial cargo proteins can be encapsulated upon fusion to minimal targeting signals (Sigmund et al. 2018; Sigmund et al. 2019; Rurup et al. 2014; Lau et al. 2018). However, the minimal targeting signals of QtEnc (QtSig, KGFTVGSLIQ) (Sigmund et al. 2019) and MxEnc (MxSig, LTVGSLRR) (Sigmund et al. 2018; McHugh et al. 2014) have a distinct sequence similarity, and it is thus possible that cargo proteins carrying these signal sequences can target both encapsulins. As this would hamper the possibility to use different encapsulin systems for multiplexing based on controlled cargo assignment, it was tested in the following whether the encapsulin targeting signals are indeed promiscuous.

Cross-functionality of native ferroxidase cargos

To test whether the native ferroxidase cargo proteins of Qt and Mx encapsulins can be targeted to the shell of the respective other species without loss of function, QtIMEF and MxBCD were co-expressed in combination with Zip14 and either QtEnc or MxEnc in HEK 293T cells treated with 2 mM FAS for 36 h. SDS-PAGE analysis after FLAG-pulldown of QtEnc revealed that targeting of either MxB, MxC or MxBCD^{P2A} containing the native MxSig targeting sequence to the Qt encapsulin lumen worked (**Figure 12A**). In addition, QtIMEF containing the native QtSig targeting peptide could successfully be targeted to the MxEnc lumen. Blue Native-PAGE analysis of cell lysates furthermore proved that both QtIMEF and MxBCD are still functional when targeted to the respective other encapsulin shell, as iron biomineralization was still observed (**Figure 12B**).

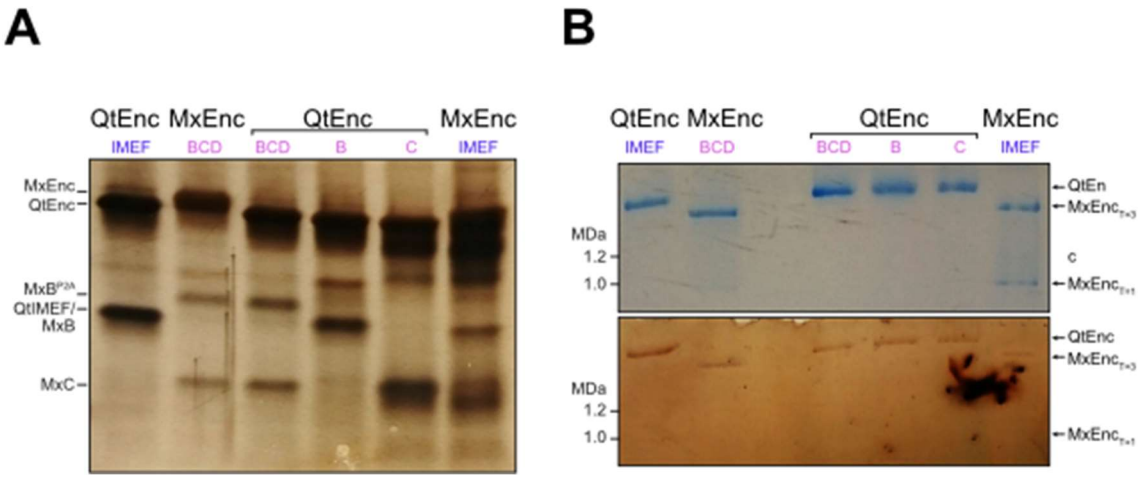

Figure 12| Cross-targeting of native encapsulin ferroxidases.
The native cargos QtIMEF and MxBCD were co-expressed with either Qt or Mx encapsulin shell and Zip14 in HEK 293T cells. **A)** SDS-PAGE analysis of Qt and Mx pulldowns from cell lysates. The respective bands for QtIMEF and MxBCD co-purified with the shells are annotated. **B)** Blue Native-PAGE analysis of cell lysates show protein assembly (Coomassie, upper panel) and iron loading (DAB-enhanced PB, bottom panel) for all construct combinations. Data are unpublished, manuscript is in preparation.

Encapsulation of artificial cargos

It has already been demonstrated that the Mx encapsulin can load artificial cargos such as fluorescent or luminescent proteins by terminal fusion with the minimal targeting sequence MxSig (Sigmund et al. 2018; Lau et al. 2018). It was thus tested if QtEnc can also encapsulate foreign cargos and whether co-targeting of different types of cargoes is possible.

In a first step, encapsulation of the fluorescent protein mEos4b as a foreign cargo inside QtEnc as well as cross-targeting into MxEnc was tested. HEK 293T cells were co-transfected with Qt or Mx encapsulin and mEos4b C-terminally fused to either the QtSig or MxSig targeting signal (**Figure 13A**). Blue Native-PAGE analysis of cell lysates showed successful assembly of Qt and Mx encapsulins. In addition, UV-Vis imaging of the gel revealed fluorescent bands running at the same height as the protein bands independent of the chosen targeting sequence, proving that mEos4b was targeted to either of the encapsulins regardless of the origin of the targeting sequence.

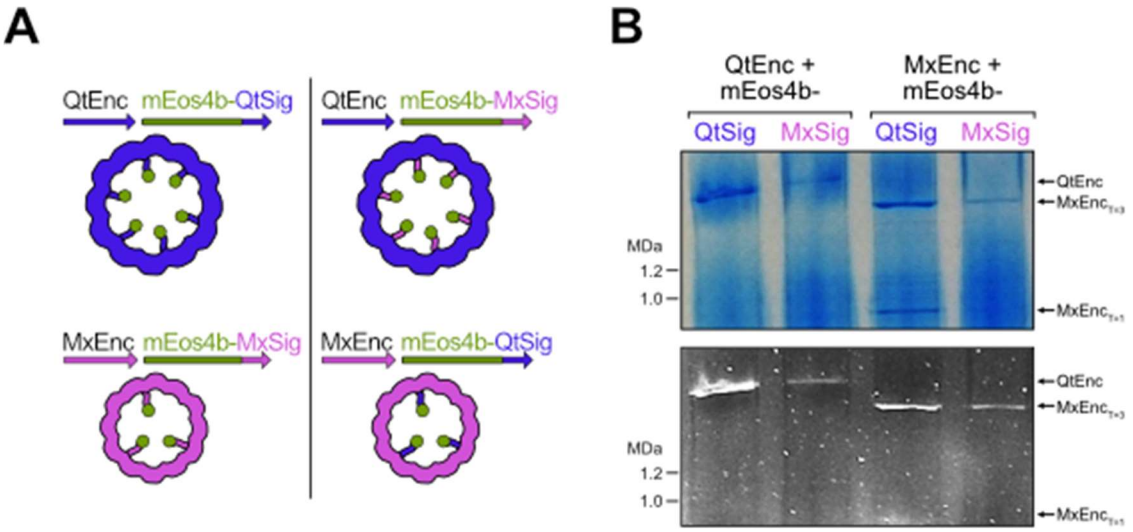

Figure 13| Targeting of the artificial cargo mEos4b to Qt and Mx encapsulin.
A) The fluorescent protein mEos4b (green) was C-terminally fused to either QtSig (blue) or MxSig (purple) and co-expressed with Qt or Mx encapsulin in HEK 293T cells. **B)** Blue Native-PAGE analysis of cell lysates show encapsulin assembly (Coomassie, upper panel) and the presence of mEos4b inside the respective encapsulin shells (UV-Vis, bottom panel). Data are unpublished, manuscript is in preparation.

In a next step, co-targeting of two different cargo proteins into Qt encapsulin was tested to demonstrate its possible applicability as a multi-purpose contrast agent. To this end, the native ferroxidase cargo QtIMEF (containing an intrinsic QtSig) and the fluorescent protein mEos4b-QtSig were chosen. QtIMEF can mediate iron biomineralization, thus generating contrast for MRI or EM imaging, whereas the fixation-stable mEos4b can be used as a contrast agent for fluorescence-based imaging techniques (**Figure 14A**). HEK 293T cells were co-transfected with QtEnc, the two chosen cargo proteins and Zip14 and treated either with 2 mM FAS or PBS as mock control for 36 h before lysates were analyzed on Blue Native-PAGE (**Figure 14B**). UV-irradiation of gels revealed fluorescent bands at the same height than the protein bands, indicating that mEos4b-QtSig was encapsulated and is still functional (**Figure 14B**, middle panel, green arrow). DAB-enhanced Prussian Blue staining further confirmed iron loading of encapsulins only for cells treated with FAS, indicating that QtIMEF is still functional (**Figure 14B**, bottom panel, orange arrow).

Alternate iron sources for encapsulin loading

Using genetically controlled iron-based contrast agents such as ferritin or encapsulin for *in vivo* imaging is advantageous as they can bypass traditional problems of synthetic contrast agents such as stability in blood and body fluids, targeted delivery or crossing of the blood-brain-barrier (Cao et al. 2014; McCarthy und Kosman 2015). However, the accessibility of iron *in vivo* for biomineralization remains a major obstacle. While iron uptake and availability can be boosted in cell culture by expressing iron importers and supplementing free iron, iron homeostasis in organisms is a delicate process and

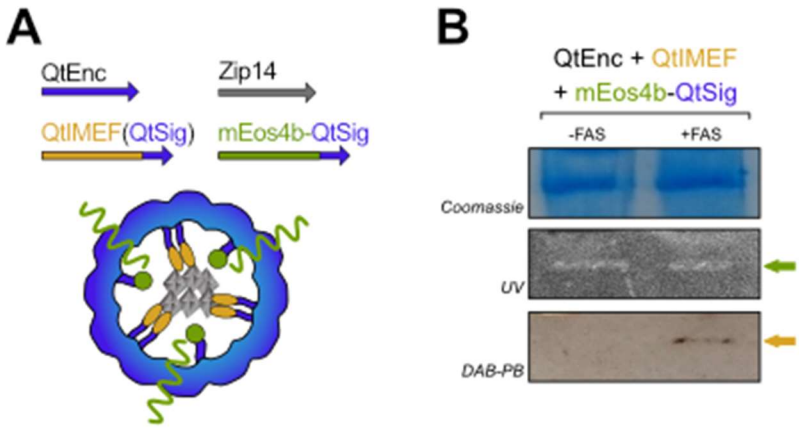

Figure 14| Co-targeting of two different cargos to QtEnc.
A) Co-expression of the native ferroxidase QtIMEF (orange) containing the intrinsic targeting signal QtSig, the fluorescent protein mEos4b (green) C-terminally fused to QtSig, the QtEnc shell (blue) and Zip14 enables iron biomineralization inside encapsulins and at the same time fluorescence signal generation. **B)** Blue Native-PAGE analysis of cells treated with 2 mM FAS for 36 h before lysis showed successful targeting of two functional cargo proteins. Protein bands (Coomassie, upper panel) co-localize with fluorescent bands (UV-Vis, middle panel), and iron staining (DAB-enhanced PB, bottom panel) was positive for cells supplemented with iron. Data are unpublished, manuscript is in preparation.

manipulations of related processes can lead to serious side effects. On the other hand, injection of free iron to the site of interest is invasive, and it remains to be assessed whether an iron-rich diet alone is enough to increase the bioavailability of iron *e.g.* in the brain to a level that allows efficient biomineralization and incorporation in contrast agents such as encapsulins. Thus, in the following section a potentially biocompatible iron delivery strategy based on ferritin and its competition for iron with encapsulin is tested. Ferritin is a ubiquitous iron storage protein that can be found in most mammals and contains up to 2500 iron atoms per protein shell (Reif 1992; Dognin und Crichton 1975; Lawson et al. 1991; Treffry et al. 1992; Theil et al. 2013; Theil 2011), and furthermore it was shown to cross the blood-brain-barrier in a receptor-mediated way (Cao et al. 2014; McCarthy und Kosman 2015). As shown in chapter 3.2.3, the overexpressed Qt and Mx encapsulin systems can efficiently compete with endogenous ferritin for externally supplemented iron. It was thus tested whether ferritin could be used to deliver iron to cells for biomineralization inside encapsulins.

HEK 293T cells were co-transfected with the Qt or Mx encapsulin system either with or without Tim-2 and supplemented with 300 µg/ml ferritin (eFt) for 36 h. Tim-2 overexpression leads to efficient ferritin accumulation inside lysosomes (Massner et al. 2018), followed by ferritin degradation and dissolution of its ferrihydrite core (Austin et al. 2005; Lockwood 2013). The generated free iron is transported into the cytosol, where it can be incorporated either into endogenous ferritin or into encapsulins (**Figure 15A**).

Blue Native-PAGE analysis of lysed cells expressing Tim-2 and treated with eFt showed iron accumulation inside both encapsulin systems. No additional iron band could be detected when expressing the Qt encapsulin, indicating that Qt out-competes endogenous ferritin for available iron. In contrast, for Mx encapsulin a strong ferritin iron band is detected, which hints at a distribution of iron between MxEnc and endogenous ferritin. In the absence of eFt, no iron loading could be detected for either encapsulin, demonstrating that the iron needed for biomineralization is indeed derived from the exogenously applied ferritin (**Figure 15B**). Without overexpression of the Tim-2 receptor but in the presence of eFt, Mx expressing cells showed a weak ferritin iron band but no encapsulin iron loading. This indicates that HEK 293T cells can take up eFt via endogenous pathways albeit less efficiently, and the accumulated iron is not enough to facilitate biomineralization inside MxEnc. In contrast, under the same conditions Qt expressing cells showed encapsulin iron loading but no ferritin iron band, confirming again that the Qt encapsulin system can sequester iron more efficiently at low iron conditions.

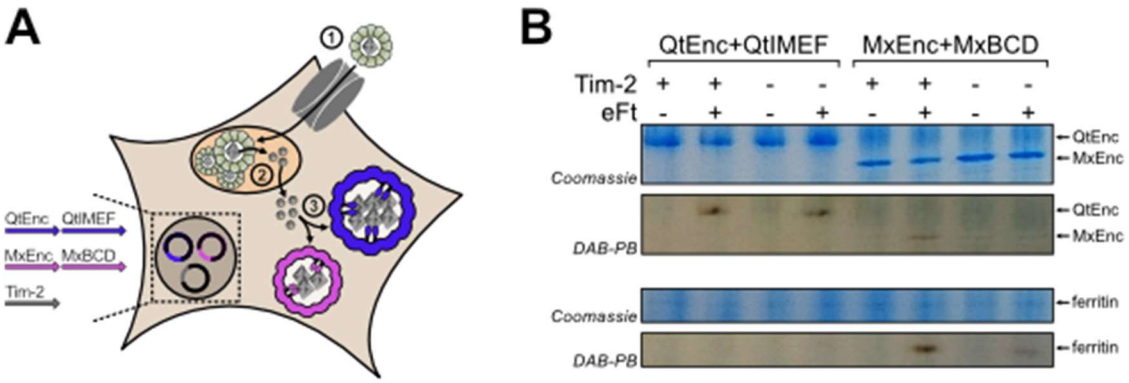

Figure 15| Ferritin can serve as an alternative iron source for encapsulin loading.
A) Ferritin taken up via the receptor Tim-2 (1) accumulates in lysosomes, where its ferrihydrite core is dissolved (2). The free iron is transported into the cytosol, where it is accumulated inside Qt or Mx encapsulin (3). **B)** HEK 293T cells were co-transfected with Tim-2 and QtEnc + QtIMEF or MxEnc + MxBCD and supplemented with 300 µg/ml ferritin for 36 h prior to lysis. Blue Native-PAGE analysis of cell lysates indicates iron loading of both Qt and Mx encapsulin system when Tim-2 is expressed and ferritin is supplemented, indicating that the iron released from ferritin can be redirected into encapsulins. The bottom panel shows increased ferritin uptake upon expression of Tim-2. Data are unpublished, manuscript is in preparation.

Establishment of a system for orthogonal cargo targeting

As the minimal targeting sequences of the Mx and Qt encapsulin systems are promiscuous in respect to each other as demonstrated above, a strategy was developed to allow precise cargo targeting into selected encapsulins without cross-reactivity.

3.2.5 Targeting of sub-cellular structures

Encapsulins are of bacterial or archaeal origin, where they form proteinaceous cytosolic organelles suspected to be involved in metabolic processes or stress responses (McHugh et al. 2014; Sutter et al. 2008; Giessen 2016; Giessen und Silver 2017). When expressed in mammalian cells encapsulins are primarily cytosolic, but can also be targeted to the membrane *via* a lipid anchor (Sigmund et al. 2018; Sigmund et al. 2019). However, as encapsulins are discussed as contrast agents for various imaging techniques in the scope of this work, their capability to target sub-cellular structures such as different organelles was examined.

Nuclear targeting of encapsulins

The nucleus is most commonly the largest organelle within eukaryotic cells and is separated from the cytosol by the nuclear envelope, a double membrane punctured by nuclear pores to gate the transport of larger molecules from and to the cytosol. For import into the nucleus, proteins are tagged with a nuclear localization signal (NLS) consisting of a short cluster of basic amino acids like lysine and arginine (Diekmann und Pereira-Leal 2013; D'Angelo et al. 2009).

To design encapsulins for nuclear import, the shell QtEnc was C-terminally fused to the bipartite NLS of nucleoplasmin KRPAATKKAGQAKKKK, which consists of two strings of basic amino acids (underlined) separated by a short linker. In addition, the cargo protein DD-N_mEos4b-QtSig was fused C-terminally to the same NLS to facilitate fluorescent readout of encapsulin localization. HEK 293T cells were co-transfected with QtEnc and DD-N_mEos4b-QtSig either with or without the NLS fused to the termini and treated with Hoechst 33342 (Thermo Fisher Scientific) to counter-stain the nuclei before live-cell fluorescent imaging. Cells expressing QtEnc-NLS + DD-N_mEos4b-QtSig_NLS showed a distinct nuclear fluorescent pattern matching the signal of Hoechst staining, whereas no cytosolic signal was detected (**Figure 16A**). Interestingly, when only the QtEnc shell was fused to the NLS but not the mEos4b cargo, the same fluorescence pattern matching the Hoechst stain was detected, indicating that mEos4b does not require a nuclear localization sequence on its own but can be transported into the nucleus bound to QtEnc (**Figure 16B**). In contrast, cells expressing QtEnc-FLAG + DD-N_mEos-QtSig with neither of the proteins fused to a NLS, a diffuse cytosolic fluorescence signal was obtained with no encapsulin-derived signal in the nucleus (**Figure 16C**).

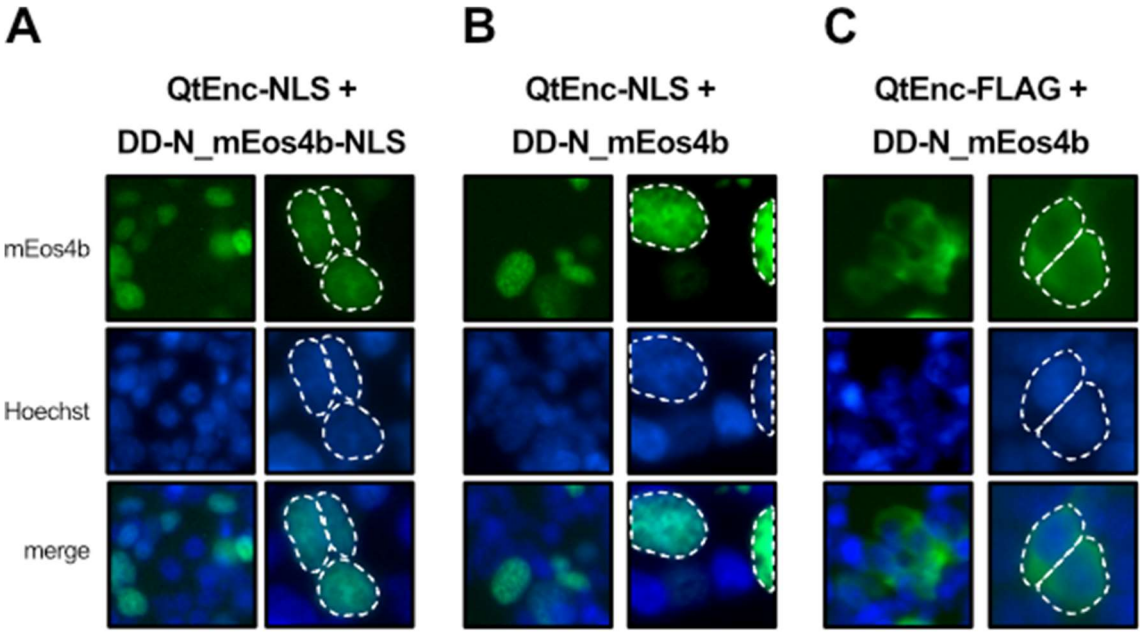

Figure 16| Targeting of QtEnc to the nucleus.
QtEnc and mEos4b-QtSig were fused to a nuclear localization signal (NLS) derived from nucleoplasmin. HEK 293T cells were transfected with the indicated construct combinations for 36 h and counter-stained with Hoechst before imaging. **A)** When the NLS was fused to both QtEnc and mEos4b-QtSig, a distinct nuclear fluorescence pattern was observed that co-localized with nuclei counter-stained with Hoechst. **B)** When the NLS was fused only to the QtEnc shell but not the mEos4b-QtSig cargo, a nuclear fluorescence pattern matching the Hoechst stain was observed. **C)** Control cells transfected with wild-type QtEnc and mEos4b-QtSig showed cytosolic fluorescence signal. Left panels: 10x magnification, right panels: 20x magnification. Data are unpublished, manuscript is in preparation.

Peroxisomal targeting of encapsulins

Peroxisomes are small sub-cellular compartments separated from the cytosol by a single lipid membrane. They are oxidative organelles involved in different metabolic processes and play an important role in the reduction of reactive oxygen species (ROS) such as hydrogen peroxide. Peroxisome-associated proteins are translated in the cytoplasm and translocated into the peroxisome in their folded state *via* a peroxisomal targeting signal (PTS) which is recognized by import receptors (Brocard und Hartig 2006; Diekmann und Pereira-Leal 2013). The most common targeting signal, the C-terminal PTS1, consists of the tripeptide (S/A/C)(K/R/H)(L/M) with the most conserved version being -SKL. In contrast, the second known transport signal PTS2 is usually located at the N-terminal end of proteins and has a less conserved sequence (Lametschwandtner et al. 1998).

To target encapsulins to the peroxisome, both QtEnc and DD-N_mEos4b-QtSig were fused C-terminally to a previously reported PTS1 version consisting of the peptide Hs55 and the non-consensus ending -SLL (EGGRRGMGFPAVRSLL) (Lametschwandtner et al. 1998). HEK 293T cells were co-transfected with QtEnc-PTS1^{Hs55} and DD-N_mEos4b-QtSig_PTS1^{Hs55} and the cell nuclei were counter-stained with Hoechst 33342 (Thermo Fisher Scientific) prior to live-cell imaging. A speckled fluorescence pattern was observed in the cytosol and around the nucleus, whereas control cells showed a diffuse cytosolic pattern (**Figure 17**).

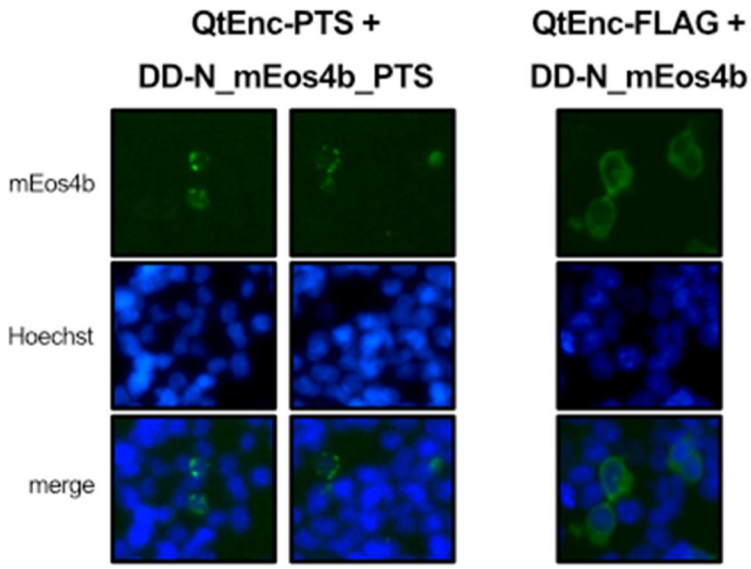

Figure 17| Peroxisomal targeting of Qt encapsulin.
HEK 293T cells were co-transfected with QtEnc-PTS1^{Hs55} and DD-N_mEos4b-QtSig-PTS1^{Hs55} and stained with Hoechst 33342. Live-cell imaging showed a distinct speckled fluorescence pattern in the cytosol (left panels), whereas control cells showed a diffuse cytosolic signal (right panel). Data are unpublished, manuscript is in preparation.

3.3 Application of iron-loading encapsulins for MRI

In this part, the applicability of iron-loaded Qt encapsulin as a fully genetic MRI contrast agent is demonstrated. Furthermore, the possibility to interact with Qt-expressing cells using magnetic fields is evaluated. In a further step, protein engineering is applied to improve the iron loading inside encapsulins and enhance the magnetic properties.

In a first step, the transverse relaxivity r_2 of iron-loaded encapsulins was measured using QtEnc + QtIMEF and MxEnc + MxBCD purified from HEK 293T cells treated with 2 mM FAS for 36 h. A linear increase of the relaxation rate ΔR_2 background-corrected for buffer absorption was observed for increasing amounts of applied encapsulin protein (**Figure 18A**, left). The relaxivity per protein was determined as the slope of a linear fit and was calculated as 56,507 $mM^{-1}s^{-1}$ and 30,809 $mM^{-1}s^{-1}$ for Qt and Mx encapsulin, respectively. Compared to commercial ferritin solution (Sigma-Aldrich) with a r_2 of 2450 $mM^{-1}s^{-1}$ per protein (**Figure 18A**, right), Qt and Mx encapsulins thus have a 23- and 13-times higher relaxivity per protein due to the higher amount of iron per protein shell (see **Table 2**). The relaxivity per iron was comparable for both encapsulins with 1.6 $mM^{-1}s^{-1}$. But showed an 18 % increase compared to commercial ferritin which ad a relaxivity per iron of 1.36 $mM^{-1}s^{-1}$ (**Figure 18B**).

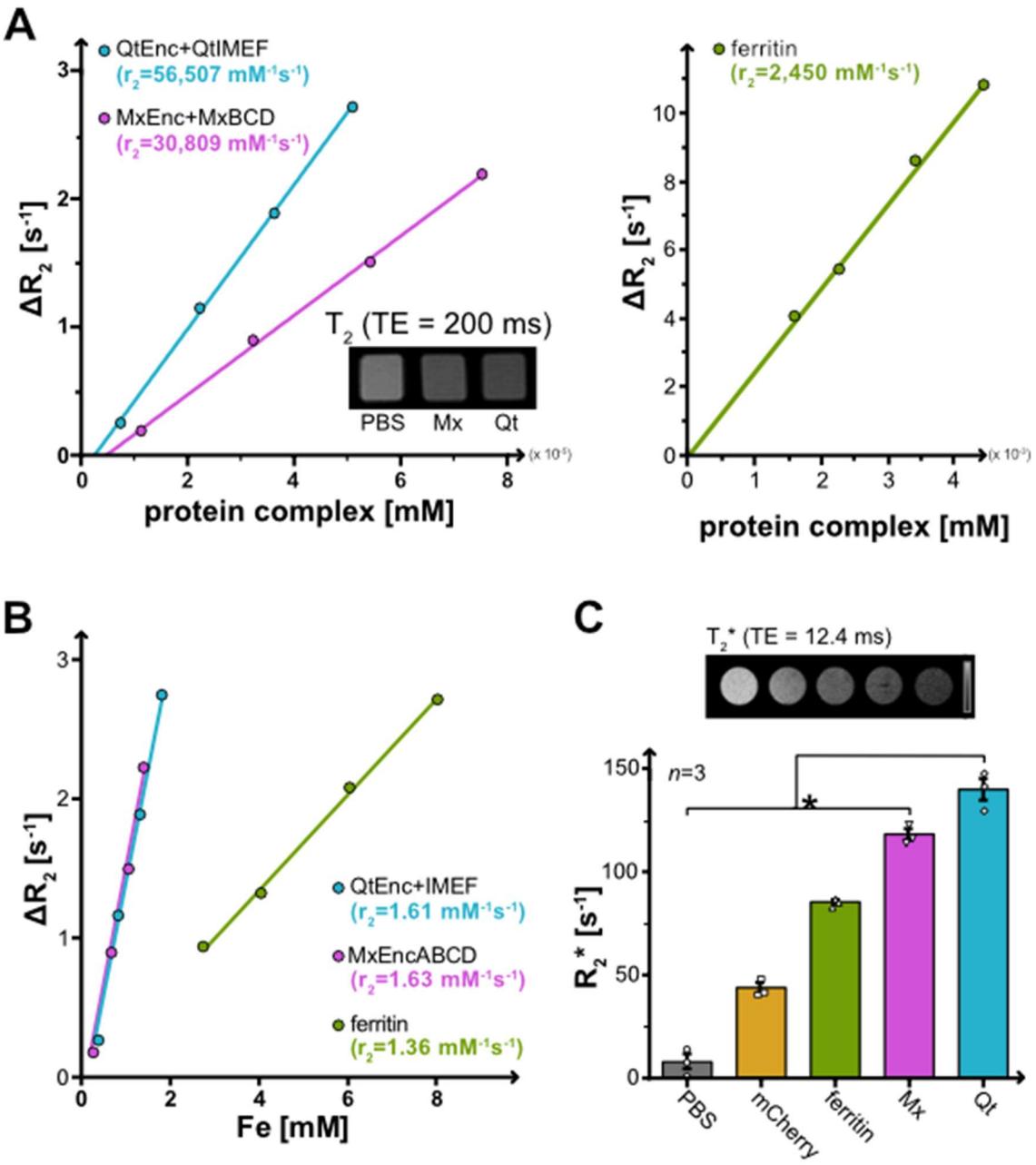

Figure 18| Application of Qt and Mx encapsulin as genetic MRI markers.
A) QtEnc + QtIMEF and MxEnc + MxBCD were purified from HEK 293T cells treated with 2 mM FAS for 36 h. Transverse relaxivity r_2 was determined as 56,507 and 30,809 $mM^{-1}s^{-1}$ for Qt (blue) and Mx (purple) encapsulin respectively. For commercial ferritin (green), r_2 was determined as 2,450 $mM^{-1}s^{-1}$ per protein. Inset shows the MR image of a transverse slice through the sample plate. **B)** Calculation of the transverse relaxivity r_2 per iron for QtEnc + QtIMEF (blue, 1.61 $mM^{-1}s^{-1}$), MxEnc + MxBCD (purple, 1.63 $mM^{-1}s^{-1}$) and commercial ferritin (green, 1.36 $mM^{-1}s^{-1}$) based on the same MR measurement than in A). Iron content of the samples was determined via ICP-MS. **C)** HEK 293T cells co-overexpressing Zip14 with either Qt or Mx encapsulin, ferritin, or mCherry were treated with 0.5 mM FAS for 36 h before the transverse relaxation rate R_2* of cell pellets was determined. Cells expressing Qt encapsulin showed a significantly higher relaxation rate than cells expressing either of the other constructs. Inset shows the MR image of a transverse slice through the sample pellet. Data are unpublished, manuscript is in preparation.

To determine the intracellular contrast generation of iron-filled encapsulins, HEK 293T cells co-transfected with Zip14 and either Qt or Mx encapsulin, ferritin or mCherry were treated with 0.5 mM FAS for 36 h before the relaxation rate R_2* of pelleted cells was determined (**Figure 18C**). Cells expressing either Mx encapsulin or ferritin showed a

significantly higher relaxation rate than control cells expressing mCherry, with MxEnc + MxBCD giving stronger contrast than ferritin as previously published [Sigmund 2018]. However, cells expressing QtEnc + QtIMEF gave a significantly higher T_2*-derived MR-contrast than cells expressing either of the other constructs, thus making iron-loaded Qt encapsulin a better contrast agent than Mx encapsulin under these conditions.

3.4 Application of encapsulins for EM

In this chapter, further applications of Qt encapsulin as a fully genetic contrast agent for other imaging methods are examined. In particular, the suitability of QtEnc for metal-based TEM contrast generation is demonstrated. Furthermore, fluorescence-based super-resolution imaging is demonstrated and mechanisms to further increase encapsulin-based signal are evaluated.

HEK 293T cells co-expressing QtEnc + QtIMEF or MxEnc + MxBCD together with Zip14 were treated with 0.5 mM FAS for 36 h before cells were collected for sample preparation. TEM images clearly revealed electron-dense, spherical particles in the cytosol of cells expressing either Qt or Mx encapsulin, whereas control cells overexpressing ferritin did not show distinct structures (**Figure 19A**). Particle diameters obtained from manual segmentation of 100 particles for each nano-compartment yielded narrow size distribution histograms (**Figure 19B**) with average diameters of 38.3 ± 1.5 nm for Qt encapsulin and 32.2 ± 2.0 nm for Mx encapsulin. Mean grey values obtained from the same segmentation furthermore revealed that Qt encapsulin particles are darker on average (**Figure 19C**), thus yielding more contrast in electron microscopy.

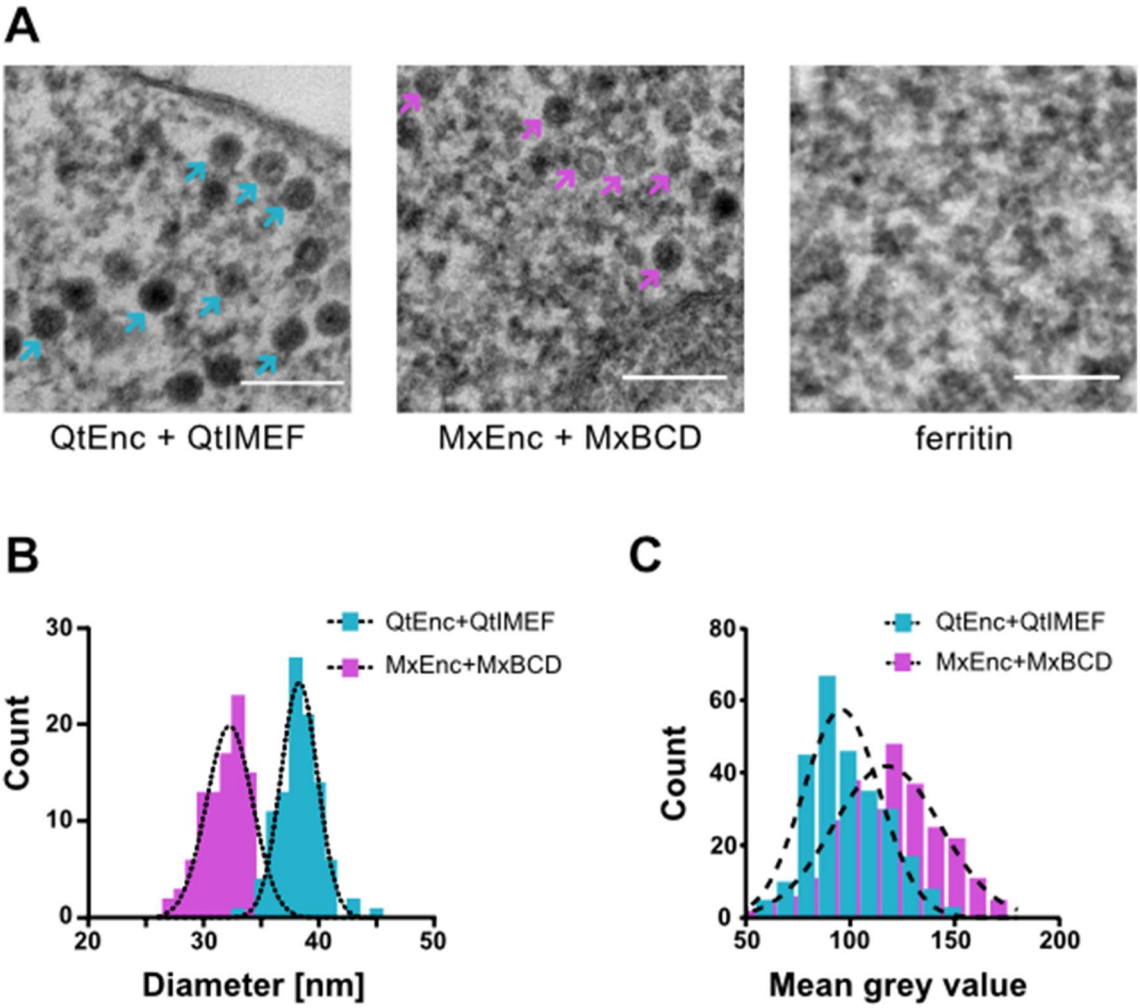

Figure 19| Application of QtEnc and MxEnc as contrast agents in electron microscopy.
Cells co-expressing either QtEnc + QtIMEF or MxEnc + MxBCD together with Zip14 were treated with 0.5 mM FAS for 36 h and imaged with TEM. **A)** TEM images of cells expressing the Qt or Mx encapsulin (left and middle panel, respectively) show encapsulins as large, electron-dense spherical objects in the cytosol. Arrows indicate selected particles. Overexpression of H-chain ferritin (right panel) did not show and discernible particles. **B)** Manual TEM image analysis of 100 nano-compartments each yielded average diameter of 38 and 32 nm for Qt and Mx encapsulins, respectively. **C)** The histogram of mean grey values obtained from the same analysis indicates that the Qt encapsulin system yields darker particles in TEM. Data were published in (Sigmund et al. 2019). Data were published in (Sigmund et al. 2019).

Chapter 4| Discussion

This doctoral thesis focused on the characterization and optimization of biological iron accumulating nano-compartments for different applications. In the first part, a possible transformation of naturally occurring ferrihydrite to magnetite is examined to improve the magnetic properties of iron-containing proteins. Different strategies are discussed to obtain magnetite or other iron minerals *in vitro* from naked ferrihydrite particles, inside the ferritin protein cage as an example of a natural biological nano-compartment or in defined organelles inside cells. In the second part, encapsulins are investigated as a nano-compartment with improved properties compared to ferritin. In particular, a new encapsulin system from *Quasibacillus thermotolerans* is characterized in detail and compared to the known encapsulin system of *Myxococcus xanthus* as well as ferritin regarding its capability to store iron and other cargos. Furthermore, possible applications of encapsulins in Magnetic Resonance Imaging (MRI) as well as Electron Microscopy are discussed.

4.1 Transformation of ferrihydrite to magnetite

Ferritin has been suggested as a fully genetically controlled EM marker (Wang et al. 2011; Matsumoto et al. 2015; Clarke und Royle 2018) and even as an interface for magnetic manipulation of cells (Stanley et al. 2016; Stanley et al. 2012; Stanley et al. 2015; Wheeler et al. 2016), although these findings were discussed controversially as the underlying physical mechanism is still poorly understood and thus questionable (Meister und Clapham 2016). In a previous work, we could demonstrate that exchanging the ferrihydrite core inside ferritin with magnetite yielding magnetoferritin lead to a considerable improvement of its magnetic properties, which allowed sorting of cells in magnetic fields and even cell ablation in magnetic hyperthermia experiments (Massner et al. 2018). However, magnetite synthesis inside the ferritin protein shell has to be performed *in vitro* under strictly anaerobic conditions and elevated temperatures, and thus magnetoferritin can only serve as a semi-genetic interface (Massner et al. 2018; Meldrum et al. 1992; Fan et al. 2012; Cai et al. 2015). Thus, the present work examined the possibility to transform ferrihydrite into magnetite under ambient conditions.

Ferrihydrite is a poorly crystalline iron oxide, which precipitates easily from solutions and is thought to be a precursor for more crystalline Fe^{3+} iron oxides as it is thermodynamically unstable (Kukkadapu et al. 2003; Cornell und Schwertmann 2003). In particular, ferrihydrite is metastable with regards to goethite, lepidocrocite and hematite, but transformation to magnetite has also been reported (Hansel et al. 2005; Kukkadapu et al. 2003; Liu et al. 2005). Several factors such as time, oxygen or different ligands can influence the transformation of ferrihydrite to other iron oxide phases, but the most important determinants are temperature, pH and the concentration of free ferrous iron (Liu et al. 2007; Hansel et al. 2005). High temperatures favor topotactic transformations, which in general require higher activation energies and often involve thermal dehydration or dehydroxylation processes (Cornell und Schwertmann 2003; Liu et al. 2007; Liu et al. 2005). At ambient temperatures ferrihydrite can undergo two competitive transformation processes, resulting in the formation of either hematite (topotactic) or lepidocrocite, goethite and magnetite (reconstructive), and pH as well as Fe^{2+} play a key role in determining which solid phase is formed (Cudennec und Lecerf 2006; Schwertmann und Murad 1983; Hansel et al. 2005; Liu et al. 2005; Kukkadapu et al. 2003). Ferrous iron as a catalyst is necessary to start the conversion processes of ferrihydrite and can significantly accelerate the transformation, and while both lepidocrocite and goethite form over a broad concentration range, transformation to magnetite requires relatively high concentrations of Fe^{2+} (Liu et al. 2007; Hansel et al. 2005). Thus, an increasing Fe^{2+} concentration shifts the secondary mineral phase from unaltered ferrihydrite to mixtures of lepidocrocite and goethite and finally to a mixture of goethite and magnetite (Hansel et al. 2005). The other key factor, pH, mainly influences the dissolution of ferrihydrite and the identity of the ionic species formed in the process. At pH 7, the dissolution of ferrihydrite is rather ineffective and thus a solid-state transformation to hematite is favored (Cudennec und Lecerf 2006; Liu et al. 2007). On the other hand, a low or high pH supports the dissolution of ferrihydrite and different ionic species can be formed, which favor the formation of either lepidocrocite or goethite (Cudennec und Lecerf 2006; Schwertmann und Murad 1983; Liu et al. 2007). For the transformation of ferrihydrite to magnetite, pH has to be tightly regulated: while magnetite formation at pH 6 or lower is impeded even at high Fe^{2+} concentrations, pH 8 potentiates magnetite precipitation and can enable a formation even at unfavorably low Fe^{2+} concentrations (Hansel et al. 2005).

While pH and Fe^{2+} concentrations are the two main determinants for the secondary mineralization of lepidocrocite and goethite, the transformation of ferrihydrite to magnetite additionally seems to be strongly influenced by the oxygenation level of the reaction solution, and most studies examining this pathway are conducted under anaerobic conditions (Liu et al. 2007; Hansel et al. 2005; Cudennec und Lecerf 2006). In general, both water and oxygen are capable of oxidizing ferrous iron, and from the resulting mixture of Fe^{2+}, Fe^{3+} and OH^- iron oxides of mixed valency such as magnetite can be formed (Cornell und Schwertmann 2003; Faivre 2016). However, under aerobic

conditions the oxidation of ferrous iron is rather effective and thus only little to no Fe^{2+} is left available to react with the resulting ferric iron, and thus purely trivalent iron oxides are preferentially formed.

4.1.1 Transformation of naked ferrihydrite particles

In chapter 3.1.1, the effect of selected variables on the transformation of naked ferrihydrite particles was studied at ambient temperatures and aerobic conditions in aqueous solution. The focus was put on pH and ferrous iron on the one hand and organic reducing agents on the other hand.

The role of pH and ferrous iron in ferrihydrite transformations

While aerobic aging of ferrihydrite particles was reported to yield goethite or hematite at ambient temperatures and a broad pH range (Liu et al. 2005), ferrous iron is thought to have a direct influence on the transformation of Ft as it supposedly controls magnetite nucleation (Hansel et al. 2005). However, transformations are heterogenous processes which can remain incomplete even at high Fe^{2+} concentrations if small fractions are not accessible for the reaction (Hansel et al. 2005; Cornell und Schwertmann 2003). In the scope of this work, no transformation of ferrihydrite was observed after four weeks in the absence of Fe^{2+}, which confirms that ferrous iron is necessary as a catalyst to trigger an interconversion (Hansel et al. 2005; Liu et al. 2005), despite the fact that ferrihydrite is considered to be a thermodynamically unstable precursor for better crystalline iron oxide phases (Cornell und Schwertmann 2003; Cudennec und Lecerf 2006). Upon addition of ferrous iron, a complete conversion of ferrihydrite was observed, and as postulated in literature (Cornell und Schwertmann 2003; Hansel et al. 2005; Cudennec und Lecerf 2006) the pH value seemed to determine which phase is re-precipitating as discussed in the following.

At pH 5, lepidocrocite was obtained as the only solid phase after 4 weeks of incubation. In previous studies, a mixture of lepidocrocite and goethite was obtained from ferrihydrite at pH 5-6, albeit under anaerobic conditions (Liu et al. 2007). However, it is postulated that $Fe(OH)^{2+}$ is the more prevalent species at acidic pH, which supports direct precipitation of lepidocrocite from monomeric or dimeric forms (Liu et al. 2007) and would thus support the findings in this thesis. In addition, according to Ostwald's step rule, the less stable phase nucleates first and higher solubility leads to higher initial precipitation rates (Ostwald 1897). As lepidocrocite is less stable and more soluble than goethite or hematite it has the highest initial precipitation rate (Hansel et al. 2005; Liu et al. 2007), which in combination with the Fe(III) species further supporting lepidocrocite formation could explain why only this mineral was observed instead of a mixture with goethite as might have been expected.

In contrast, incubation at pH 7 lead to the complete interconversion and exclusive formation of goethite. Theoretically, hematite formation should have been favored at this pH, as the ineffective dissolution of ferrihydrite hampers reconstructive transformation pathways (Cudennec und Lecerf 2006). However, this topotactic transformation would require elevated temperatures due to the high activation energy, while low temperatures lead to a reconstructive transformation instead (Liu et al. 2007; Schwertmann und Murad 1983). Furthermore, neutral pH conditions favor the formation of $Fe(OH)_2^+$ as the dominant ferric iron ion, which was suggested to promote the formation of goethite via a polymerization mechanism rather than lepidocrocite (Liu et al. 2007). In general, aquahydroxo ions, which form preferentially at elevated pH, are thought to be important for goethite formation, and an equilibrium of monovalent ions and ferrihydrite was suggested to favor goethite formation over lepidocrocite (Cudennec und Lecerf 2006; Schwertmann und Murad 1983). Aerobic aging of ferrihydrite at pH 7.2 was reported to yield predominantly goethite, albeit samples were incubated more than a year and without additional Fe^{2+} (Kukkadapu et al. 2003). It is possible that the combination of Fe^{2+} as a catalyst and the rather long incubation time in the present study were sufficient to enable even a potentially ineffective transformation process to complete, leading to goethite formation as a result.

Incubation at pH 8 also resulted in the complete transformation of ferrihydrite, but with goethite as the sole end phase. This sample condition was of special interest as the pH in combination with enough Fe^{2+} supplementation is supposed to be optimal for the transformation to magnetite (Cudennec und Lecerf 2006). However, reported successful transformations were conducted under strictly anaerobic conditions (Cudennec und Lecerf 2006; Hansel et al. 2005; Liu et al. 2007), and in nature known magnetite formation processes, *e.g.* in magnetosomes, also happen under anaerobic or micro-aerobic conditions (Yan et al. 2012; Lee et al. 1998). Furthermore, it has been reported that without initiation of magnetite nucleation, a complete transformation of ferrihydrite to lepidocrocite and goethite takes place, and lepidocrocite as the thermodynamically less stable phase at this pH dissolves again with time to form exclusively goethite (Hansel et al. 2005; Liu et al. 2007). On the other hand, pH 8 has been reported to favor transformation to hematite, although these observations are mainly in anaerobic reaction conditions or with high temperatures (Kukkadapu et al. 2003; Liu et al. 2005). It seems rational that no magnetite nucleation could be initiated in this set of experiments and hematite formation was impeded by the moderate incubation temperature, thus leading to the formation of goethite in the end, even though the detailed mechanisms initiating magnetite nucleation in literature remain unclear. It is entirely likely, however, that the aerobic incubation conditions led to an unfavorable low Fe^{2+} content due to high oxidation rates, and thus the correct Fe^{2+}/Fe^{3+} stoichiometry needed for magnetite precipitation could not be achieved.

At pH 4 and 9, no transformation of ferrihydrite was observed despite the addition of ferrous iron. This finding is rather surprising, as both low and high pH should enhance

the dissolution of ferrihydrite and Fe^{2+} was added to act as a catalyst (Hansel et al. 2005; Liu et al. 2007). In an old study by Schwertmann et. al. (Schwertmann und Murad 1983), pH 4 was determined as an optimum for ferrihydrite transformation to goethite via monovalent Fe(III) aquahydroxo ion complexes, albeit the transformation process was monitored over 3 years and no Fe^{2+} was added. More recent studies suggest that the transformation rate of ferrihydrite decreases at such a low pH because iron is not adsorbed to ferrihydrite as readily anymore, but becomes more soluble and no longer precipitate easily (Cudennec und Lecerf 2006; Liu et al. 2007; Liu et al. 2005). In addition, the formation of aqua ions instead of aquahydroxo ions at pH 4 was postulated, which are less favorable for goethite formation (Cudennec und Lecerf 2006; Schwertmann und Murad 1983). At pH 9, on the other hand, the adsorption rates and thus the transformation efficiencies are increased (Liu et al. 2005) and goethite formation was observed at high pH up to 12 (Liu et al. 2007; Cudennec und Lecerf 2006; Kukkadapu et al. 2003). However, only little ferrous iron is available as monomeric ions ($FeOH^+$) and the catalytic dissolution of ferrihydrite is slow, which slowed down goethite formation from ferrihydrite significantly (Liu et al. 2007). In addition, $Fe(OH)_2$ is the preferential species at pH 9, which usually catalyzes the solid-state transformation to hematite (Liu et al. 2007; Liu et al. 2005). As discussed earlier, such topotactic reactions are unlikely to happen at room temperature as the required activation energies are high.

In summary, the findings in chapter 3.1.1 are largely in accordance with literature and confirm that ferrihydrite can be transformed via reconstructive pathways only in the presence of ferrous iron, which acts as a catalyst. The suggested mechanism behind these processes is based on the adsorption of ferrous iron to the ferrihydrite surface followed by the transfer of an electron from ferrihydrite-bound Fe^{3+} to the adsorbed Fe^{2+}. The resulting ferrihydrite-bound Fe^{2+} decreases the crystallinity and destabilizes ferrihydrite due to its larger radius, thus detaching from the iron oxide allowing for a dissolution of ferrihydrite, which can then initiate the re-precipitation of different other phases (see **Figure 1B**) (Hansel et al. 2005; Cornell und Schwertmann 2003; Liu et al. 2007). While the important role of pH in determining the formed mineral phase could be confirmed in general, the obtained iron oxide phases were notably either pure lepidocrocite or pure goethite, while published experiments usually yielded a mixture of both, sometimes also interspersed with hematite (Liu et al. 2007; Hansel et al. 2005; Cudennec und Lecerf 2006). A transformation to magnetite was not observed in any reaction condition, which indicates that no nucleation could be initiated, probably due to the aerobic reaction conditions. These results also confirm that magnetite cannot be obtained from goethite or lepidocrocite upon addition of Fe^{2+} under aerobic conditions, which is in agreement with previous findings that ferrihydrite is necessary as a precursor (Hansel et al. 2005).

Reducing agents can serve as initiators of ferrihydrite transformation

In the scope of this work, different biologically relevant compounds have been investigated regarding their potential to interact with and reduce ferrihydrite. However, only ascorbic acid, which serves a dual purpose as reducing agent and oxygen scavenger, most likely led to a minor transformation of naked ferrihydrite particles to magnetite as confirmed by Raman analysis and XRD measurements (**Figure 1** and **Figure 2**).

Ferrihydrite has a high intrinsic activity thus allowing the adsorption of other metals or nutrients like phosphate, and strong reductants can transfer electrons to ferric iron leading to dissolution and re-precipitation as thermodynamically more stable phases (Hansel et al. 2005), as discussed in chapter XX in more detail. In addition, ferrous iron itself also has a strong reducing capacity and can thus induce dissolution of ferrihydrite with subsequent conversion to other mineral phases upon transfer of an electron (Hansel et al. 2005; Xiao et al. 2018), as outlined in chapter xx. Such reconstructive processes can lead to the transformation of ferrihydrite to e.g. lepidocrocite and goethite (Liu et al. 2007; Cornell und Schwertmann 2003).

Ferrihydrite also plays an important role for metabolic processes of dissimilatory iron-reducing bacteria, which can use iron oxides as terminal electron acceptors in anaerobic respiration. In the case of ferrihydrite, this leads to the reduction and transformation of ferrihydrite to a number of different phases (Hansel et al. 2005). Kukkadapu et. al. demonstrated that Shewanella putrefaciens, a facultative anaerobe marine bacterium, uses lactate for electron transfer to ferrihydrite leading to a reduction of Fe3+ bound in ferrihydrite, albeit under anaerobic conditions (Kukkadapu et al. 2003). Transformations to magnetite and goethite along with 6-line ferrihydrite were observed, but magnetite could only be obtained in PIPES buffer in the presence of a quinone. Interestingly, magnetite-containing samples also contained well-crystalline Ft, which prompted the authors to propose 6-line ferrihydrite as an intermediate in magnetite formation. However, no direct interaction between lactate and ferrihydrite was observed (Kukkadapu et al. 2003), even though lactate was reported to retard the formation of goethite (Liu et al. 2005), thus potentially favoring magnetite formation. In the scope of this thesis, a transformation of naked ferrihydrite particles incubated with lactate for 21 days was not observed (**Figure 1**), which indicates that either further additives or different buffer conditions are required or a lactate-mediated reduction of ferrihydrite is not possible under aerobic conditions.

The effect of ascorbate on ferrihydrite is controversial. On the one hand, some plants secrete ascorbic acid to increase their iron uptake as Asc induces a reductive dissolution of ferric iron oxides to soluble ferrous iron species (Xiao et al. 2018), and if the concentration of generated ferrous iron is high enough a Fe^{2+}-mediated transformation of ferrihydrite could be triggered indirectly mediated by ascorbate. On the other hand, Asc was shown to inhibit the formation of goethite, lepidocrocite and magnetite under

oxic and anoxic conditions, supposedly leading to a re-formation of ferrihydrite instead (Xiao et al. 2018). In the context of this work, incubation of naked ferrihydrite particles with ascorbic acid under aerobic conditions at room temperature led to a clear change in the Raman spectrum, and further XRD measurements confirmed a partial transformation to magnetite (**Figure 2**). However, the cytosolic concentration of ascorbic acid in humans is about an order of magnitude lower than in the experimental conditions chosen here (Badu-Boateng und Naftalin 2019), thus obtaining similar results in a cellular context would require high intracellular Asc concentrations, *e.g.* due to local accumulations. Furthermore, it has to be pointed out that the pH was not monitored and adjusted during the long-term incubation of ferrihydrite with Asc in the present work. While the oxidation of ascorbic acid in general is not affected in a pH range of 5.5 to 8.5 (Laroff et al. 1972), the pH of ferrihydrite solutions was observed to decrease with aging (Kukkadapu et al. 2003) and fluctuations of the solution pH could affect the protonation of ions on the iron oxide surface thus affecting the reaction (Boyer und J. McCleary 1987). It is also notable that no other iron oxide species apart from ferrihydrite and magnetite were observed in the Raman analyses. While this could indicate that no (stable) intermediates were formed in the transformation process, it is desirable to perform additional measurements at earlier time points both to confirm the absence of intermediates and to follow the time course of the transformation gaining more information about the reaction speed. Furthermore, the Raman spectra obtained after 14 and 21 days indicate an incomplete transformation with only a minor part of the ferrihydrite transformed into magnetite and no clear further progression of the reaction. While the reaction could have been stalled due to the consumption of Asc or its decomposition which is enhanced at acidic pH (Golubitskii et al. 2007) or due to a slower transformation rate at low pH (Kukkadapu et al. 2003), it is also possible that only the surface of ferrihydrite particles is accessible for a reductive transformation while the particle core is not affected, thus resulting in a mixture of ferrihydrite and magnetite. To address these questions, further experiments under optimized reaction conditions with stringent pH control and additional monitoring of ascorbic acid concentration as well as ferrous iron generation are recommended.

4.1.2 Transformation of protein-coated ferrihydrite

Chapter 3.1.2 addressed the transformation of protein-encapsulated ferrihydrite with focus on the iron storage protein ferritin. In particular, the effect of the reducing agent ascorbic acid as well as pH and lysosomal environment on ferritin iron content was examined.

Ascorbic acid and ferritin

While ascorbic acid is crucial as a reducing agent and functions as an antioxidant in nature (Vladimirova und Kochev 2010; Xiao et al. 2018), its role in ferritin iron mobilization in organism has been debated, although ferritin has even been suggested to have intrinsic ascorbate oxidase activity (Badu-Boateng und Naftalin 2019). Whereas some publications claim *asc* has strong reducing activity (Bienfait und van den Briel, M. L. 1980; Mazur et al. 1955; Reif 1992) and Asc-dependent release of iron from ferritin was even shown for neuroblastoma cells (Baader et al. 1996), other publications sees no major role for ascorbic acid-mediated iron mobilization in biological systems as it can mobilize only minor parts of the stored iron (Roginsky et al. 1997; Dognin und Crichton 1975; Sirivech et al. 1974). Mechanistically, ascorbic acid is known to mobilize iron from ferritin via a reductive pathway (see chapter 1.1.2 for details on ferritin iron biology) (Mazur et al. 1955; Reif 1992; Badu-Boateng und Naftalin 2019; Bienfait und van den Briel, M. L. 1980; Sirivech et al. 1974; Roginsky et al. 1997) without obvious damage to the protein shell itself (Bienfait und van den Briel, M. L. 1980). However, it is still debated if Asc is small enough to penetrate the shell and enter the cavity (Badu-Boateng und Naftalin 2019; Sirivech et al. 1974), if it instead enters only the three-fold channel that serve as entry points for iron (Roginsky et al. 1997) or whether it transfers electrons from the outside through the shell (Vladimirova und Kochev 2010; Carmona et al. 2014). Some published works even suggest that ascorbic acid might act only via an indirect mechanism involving Asc oxidation to generate superoxide ions which then reduce the iron inside ferritin (Baader et al. 1996; Badu-Boateng und Naftalin 2019; Boyer und J. McCleary 1987). Most commonly, however, it is assumed that it is either the ascorbate anion $AscH^-$ or the monodehydroascorbate radical $AscH^{\cdot -}$ that transfer electrons to the ferritin mineral core, resulting in either a monodehydroascorbate radical or dehydroascorbate Asc^{2-} according to the following two equations (Badu-Boateng und Naftalin 2019; Roginsky et al. 1997; Boyer und J. McCleary 1987):

$$AscH^- + ferritin{:}\,Fe^{3+} \rightarrow AscH^{\cdot -} + ferritin{:}\,Fe^{2+} + H^+ \quad \text{(Eq 1)}$$

$$AscH^{\cdot -} + ferritin{:}\,Fe^{3+} \rightarrow Asc^{2-} + ferritin{:}\,Fe^{2+} + H^+ \quad \text{(Eq 2)}$$

The generated ferrous iron associated with ferrihydrite can then dissolve from the mineral surface thus leading to a dissolution of the iron oxide (Roginsky et al. 1997). Further supporting these two equations are publications demonstrating that $AscH^-$ is the active form in ferritin iron mobilization, and the finding that the ascorbic acid radical can serve as an electron donor in single-electron transfer reactions, which led to increased ferritin iron mobilization compared to $AscH^-$ alone (Badu-Boateng et al. 2017; Roginsky et al. 1997; Bienfait und van den Briel, M. L. 1980; Badu-Boateng und Naftalin 2019).

While early publications on ascorbate and ferritin suggest that the ferrous iron generated upon reduction of the ferrihydrite mineral core might be retained inside the protein shell without a chelator (Boyer und J. McCleary 1987; Watt et al. 1985; Reif 1992; Roginsky et al. 1997), other works suggest that hydrated Fe^{2+} is soluble enough to leave the protein

shell via the three-fold channels (Vladimirova und Kochev 2010; Badu-Boateng et al. 2017; Badu-Boateng und Naftalin 2019; Theil 2011). As ascorbic acid had been shown to trigger a transformation of naked ferrihydrite particles yielding some magnetite in the scope of this work, the effect of *asc* on ferritin-ferrihydrite was tested based on the hypothesis that ferrous iron generated inside the ferritin cavity cannot leave the protein shell easily in the absence of chelators and thus could cause a local reductive transformation of ferrihydrite inside the ferritin shell potentially yielding protein-encapsulated magnetite. However, the results presented in chapter 3.1.2 suggest that ascorbic acid can indeed promote the mobilization of iron atoms from ferrihydrite even in the absence of iron chelators, resulting in a depleted but probably intact protein shell (**Figure 5B**). The formation of protein-free dark brown pellets indicates that the mobilized iron diffuses out of the ferritin shell and re-oxidizes in solution resulting in insoluble iron oxide precipitates, thus effectively dissolving and depleting the ferrihydrite core of ferritin. However, the observed ferritin iron depletion was significantly faster and more effective than expected, leaving the protein mostly drained of iron in about 5 hours in contrast to the incomplete iron removal reported in literature (Boyer und J. McCleary 1987; Badu-Boateng und Naftalin 2019). In addition, a fast re-oxidation of ferrous iron inside the ferritin shell by molecular oxygen has been proposed, which would cause a re-trapping in form of insoluble ferric iron (Roginsky et al. 1997). The findings in this work thus raise questions regarding the kinetics of iron diffusion through the shell, as they indicate that the dissolution of ferrous iron from the mineral core and its diffusion through the shell were faster than possible re-oxidation processes mediated by O_2 followed by re-precipitation inside the shell. However, the obtained results clearly indicate that a reductive transformation of ferrihydrite inside the protein shell mediated by ascorbic acid is hampered by the fast depletion of the mineral core, and thus other strategies to form magnetite in a biologically relevant context were assessed in the following.

Ferritin in an artificial lysosomal environment

Lysosomes play a crucial role in mammalian iron metabolism (see chapter 1.1.2), as transferrin will be taken up by the transferrin receptor TfR1 *via* receptor-mediated endocytosis to release its bound ferric iron in lysosomes due to the acidic pH (Octave et al. 1983). While the receptor is recycled back to the plasma membrane, the released iron will be reduced inside the lysosomal compartment by Steap3, and either fed into the labile iron pool or stored in ferritin (Badu-Boateng und Naftalin 2019). Lysosomes have also been discussed as crucial for the mobilization of stored iron from ferritin (Badu-Boateng und Naftalin 2019; Badu-Boateng et al. 2017), as ferrous iron dissociates more easily from ferrihydrite at low pH (Mazur et al. 1955). Notably, we were able to demonstrate in a recent publication that externally supplied ferritin could be taken up into cultured mammalian cells via TfR1, and that this uptake led to an accumulation inside lysosomes (Massner et al. 2018). To examine potential effects of the lysosomal environment on ferritin and its ferrihydrite mineral core in a more easily controllable *in*

vitro setting, ferritin samples were incubated in artificial lysosomal fluid (ALF) in the present work. ALF is an acidic solution mimicking the phago-lysosomal pH of 4.5-5 and has originally been developed as a simulated physiological fluid to investigate the durability of man-made fibers after phagocytosis into cells (Thélohan und Meringo 1994; Stopford et al. 2003).

As shown in **Figure 6**, dialysis of ferritin against ALF pH 4.6 for 24 h led to depletion of the ferritin mineral core and formation of iron oxide precipitates with only minor losses of the protein shell itself. The protein loss was not significant (unpaired t-test, $p > 0.1$, $n = 3$ biological replicates), confirming that ferritin is stable at acidic pH (Granick 1942; Crichton 1984), a finding which on the one hand strongly suggests that further proteolytic or enzymatic components are required for lysosomal degradation of ferritin and on the other hand indicates that a dissociation of the protein shell is not required to release iron from ferritin in a lysosomal environment. As the protein shell is still intact, the question arises how iron stored in ferritin was mobilized in this experimental set-up. Reportedly, reduction of ferric iron is pH-dependent and more effective at low pH (Watt et al. 1985), and such conditions also promote the dissociation of ferrous iron from ferrihydrite (Mazur et al. 1955). It is thus possible that the low pH conditions chosen in the presented work were sufficient to mobilize iron from ferritin. It should also be noted that the ALF formulation contains sodium citrate, citric acid and disodium tartrate which can all act as low molecular weight, endogenous iron chelators forming different complexes with ferrous and ferric iron (Graham et al. 1998; Hamm et al. 1954; Bobtelsky und Jordan 1947; Ivanov und Kosoy 1975) as well as glycine, which can also form complexes with Fe^{2+} and Fe^{3+} (Yakubov et al. 1983; Djurdjevic 1990). These reagents could potentially aid in the depletion of the ferritin iron core by aiding the dissociation of ferrous iron from the iron oxide mineral.

Magnetometry measurements of the obtained protein-free iron oxide pellet indicated the formation of superparamagnetic material with small blocking temperatures, and dialysis over longer time periods led to a small shift to higher blocking temperatures ($T_B = 9$ K for 11 d and $T_B = 12$ K for 27 d) while not affecting the protein stability, which could indicate a continuous growth or not yet completed transformation process of an iron oxide mineral outside the protein shell. While lactate as well as pyruvate are included in the artificial lysosomal fluid, both compounds were already determined as too weak reducing agents to trigger a reductive transformation as discussed in chapter 4.1.1. It could therefore be speculated that possible transformation processes in ALF are dictated solely by pH and thus ferrihydrite or lepidocrocite could be expected to form. However, possible influences of chelating agents and the complexes they form with iron have not been considered in experiments with naked ferrihydrite particles, so no final conclusion on the nature of the formed iron oxide can be made as Raman analysis failed due to high background noise. In addition, precipitation was only observed outside the ferritin protein shell, so while ferritin might be a suitable means to increase the iron load in lysosomes – which could enhance initial ferrihydrite aggregation and thus indeed help possible transformation

processes (Kukkadapu et al. 2003) – it seems a reductive transformation *inside* the ferritin protein shell is not possible in such an experimental setting.

The effect of long-term ferritin treatment on lysosomal iron content

While a reductive transformation of ferrihydrite inside the ferritin nano-compartment seems to be hampered by the insufficient retention of dissociated iron atoms thus probably not allowing enough interaction between ferrous iron and the remaining ferrihydrite to initiate magnetite nucleation, the lysosomal compartment itself could serve as a biologically defined, size-restricted compartment with defined environmental conditions for local ferrihydrite transformation. In such a setting, ferritin in combination with TfR1 would serve as an iron delivery mechanism to increase the local concentration of ferrihydrite in a controlled and biologically relevant manner. While magnetite formation usually occurs at basic pH (Cudennec und Lecerf 2006; Hansel et al. 2005; Liu et al. 2007) and lysosomes are reported to have an oxidizing milieu (Austin et al. 2005), the presence and activity of reducing agents in lysosomes has been demonstrated (Lloyd 1986; Lockwood 2013). It can thus be theorized that the continuous reduction and dissolution of iron from the surface of ferrihydrite mediated by reducing agents in combination with a high local ferrihydrite concentration accelerating transformation processes (Kukkadapu et al. 2003) could be sufficient to trigger a transformation of ferrihydrite, either to lepidocrocite as favored by the acidic pH or to magnetite if a nucleation after reduction of ferric iron can occur.

Raman analysis of lysosomes isolated from HEK 293T cells continuously supplemented with ferritin proved to be difficult as the biological samples generated noisy signals. However, in comparison to control cells a small peak could be identified which was indicative of ferrihydrite based on its chemical shift. Importantly, no peaks indicating lepidocrocite formation could be distinguished upon comparison with control spectra, which strongly suggests that no pH-driven transformation has occurred. Further magnetometry measurements of purified lysosomes after 27 d of ferritin supplementation revealed a blocking temperature T_B of 15 K with a clear curve splitting up to $T_B \approx 100$ K, which indicates the presence of larger agglomerates. Such an effect has already been described for short-term loading of lysosomes with magnetoferritin in combination with the murine ferritin uptake receptor Tim-2, however larger agglomerations were obtained within a shorter supplementation time (Massner et al. 2018).

In conclusion, the findings presented in this work indicate that ferrihydrite originating from ferritin can precipitate or form agglomerations inside lysosomes after mobilization from the protein iron core. However, it has to be assumed that no pH-driven transformation or reduction took place as the particles were most likely identified as ferrihydrite. In addition, particle agglomeration was less effective than previously observed for magnetite inside lysosomes, which suggests that ferrihydrite is less stable in the lysosomal environment and prone to dissolution, which possibly led to a partial export from lysosomes to feed

mobilized iron into the cellular iron metabolism. While this observation contradicts earlier findings that naked ferrihydrite particles are stable at pH 4, it is likely that iron chelators are present in the lysosome aiding the dissolution of ferrihydrite, as was also observed in experiments with artificial lysosomal fluid. To confirm this hypothesis, further studies will be necessary including an analysis of intracellular and intra-lysosomal iron contents to determine the degree of iron export from lysosomes, and it is recommended to perform further magnetometry measurements at earlier time points to gain more insight in the kinetics of iron agglomeration inside lysosomes.

4.2 Characterization of the Qt encapsulin system

Encapsulins are of bacterial or archaeal origin and so far, different encapsulins with T = 1 or T = 3 icosahedral symmetry have mostly been studied either in their originating organism, in *E. coli* (Namba et al. 2005; McHugh et al. 2014; Moon et al. 2014; Sutter et al. 2008; Lau et al. 2018) or even *in vitro* (Rurup et al. 2014). In 2018, the first successful encapsulin expressions in eukaryotic cells have been reported. On the one hand, expression of MxEncA and loading of artificial (split-)fluorescent cargo was shown in yeast (Lau et al. 2018), and on the other hand the successful assembly of MxEncA was demonstrated in mammalian HEK 293T cells with loading of either functional MxEncB,C,D cargos mediating iron loading or artificial cargos mediating other enzymatic reactions (Sigmund et al. 2018). In the scope of this work and the resulting publication (Sigmund et al. 2019), the first encapsulin with T = 4 icosahedral symmetry was characterized in detail and its successful self-assembly as well as loading of native and artificial cargos was demonstrated both in *E. coli* and in mammalian cells.

4.2.1 Expression in bacteria and mammalian cells

For expression of the Qt encapsulin system in *E. coli* BL21(DE3), the pRSFDuet™-1 vector containing two multiple cloning sites was used for IPTG-inducible expression. Interestingly, an efficient encapsulin formation was only observed when the QtEnc shell protein was inserted into the second MCS (data not shown) despite both MCS being preceded by a T7 promotor. This sequence order mimics the architecture of core encapsulin operons, where the cargo proteins are immediately upstream of the capsid protein, if not fused to the shell (Sutter et al. 2008; Giessen 2016).

For mammalian expression, plasmid constructs were generated containing either QtEnc or the cargo QtIMEF under a CMV promotor for high-level constitutive expression. A FLAG epitope was added C-terminal of QtEnc *via* a short GSG-linker to enable affinity purification and enrichment on magnetic beads. The QtIMEF cargo contained the conserved C-terminal targeting peptide KGFTVGSLIQ (QtSig). Co-expression of QtEnc

and QtIMEF in HEK 293T cells and subsequent analysis on BN-PAGE showed a single, high molecular weight protein band above 1.2 MDa (**Figure 8B**). Interestingly, while expression of the T=3 icosahedral Mx encapsulin was reported to give additional particles with T=1 symmetry if expressed outside its host organism suggesting a decreased fidelity of self-assembly in *E.coli* and mammalian cells (McHugh et al. 2014; Sigmund et al. 2018), expression of QtEnc yielded only one single protein band running above the corresponding T=3 protein band of MxEnc. This indicates that QtEnc forms nano-compartments with a higher molecular weight than MxEnc thus probably having a higher triangulation number, and that QtEnc particles assemble with high fidelity even in a non-native host organism. The DLS measurements of FLAG-purified QtEnc and QtEnc + QtIMEF, which showed a narrow size distribution (**Figure 8D**), further support this finding while also indicating that cargo encapsulation does not lead to an increase in particle size, *e.g.*, due to expansion of the shell as has been observed for some viruses packaging nucleic acids (Sutter et al. 2008; Heinemann et al. 2011). Notably, DLS measurements of the smaller Tm encapsulin expressed in *E.coli* were reported to yield large hydrodynamic diameters, which was attributed to random attachment of nucleic acids to the exterior surface by the authors (Moon et al. 2014), while DLS measurements of Mx encapsulin as well as Qt encapsulin obtained from mammalian cells did not show such deviations (Sigmund et al. 2018). FLAG affinity purification of QtEnc shells co-expressing QtIMEF and subsequent SDS-PAGE analysis confirmed that the QtIMEF cargo is co-localized to the encapsulin shell. Furthermore, the percental protein ratio of shell and cargo was determined to be almost 1:1 with 231 ± 5 molecules QtIMEF packaged in one shell on average (**Figure 8C**). Notably, a different study on IMEF from Bacillaceae MTCC 10057 suggested that about 150 IMEF cargos are situated within the T = 3 encapsulin (180 shell monomers), which would yield a comparable shell:cargo ratio (Giessen und Silver 2017). In comparison, for the Mx encapsulin which encapsulates three native cargos, only about 28 % of the total protein content were allotted to the cargo proteins corresponding to about 175 cargo proteins per shell (McHugh et al. 2014). These numbers are in stark contrast to the T=1 encapsulin system of *B. linens*, where only one DyP cargo can be packed per shell due to the relatively large size of the cargo protein (Sutter et al. 2008), which was however demonstrated to be still fully functional upon encapsulation (Rahmanpour und Bugg 2013).

4.2.2 Structural analysis of the Qt encapsulin system

So far, several encapsulin structures from different bacterial and archaeal organisms have been resolved either via crystallography or by high-resolution electron microscopy (Akita et al. 2007; McHugh et al. 2014; Sutter et al. 2008; Rahmanpour und Bugg 2013; Nichols et al. 2020; Lončar Nikola et al. 2020), and they were all classified as either T = 1 or T = 3 icosahedral symmetry. In the scope of the present work, the Qt encapsulin structure was resolved with cryo-EM in cooperation with the Laboratory for Biomolecular

Design at the Technical University of Munich and was identified as the first to be reported with T=4 icosahedral symmetry. The asymmetric unit consisted of three hexameric and one pentameric monomer (**Figure 9B**) compared to three possible monomer conformations (two hexameric and one pentameric) in T = 3 encapsulins (Akita et al. 2007) and only one monomer conformation in the T = 1 Tm encapsulin, which is built entirely from pentamers (Sutter et al. 2008). Qt encapsulins expressed in either bacterial or mammalian hosts did not differ in their structure with both showing an identical overall architecture, same monomer conformations and also same outer and inner diameters (**Figure 10**). The outer diameter of QtEnc was determined as 43 nm on the five-fold axis and 40 nm on the two-fold axis, whereas the inner diameter was determined as 30 nm. These dimensions are significantly larger than T = 1 encapsulins with about 24 nm outer diameter (Sutter et al. 2008) and T = 3 encapsulins with about 32 nm outer diameter (McHugh et al. 2014; Akita et al. 2007). Furthermore, two putative pore regions could be identified at the five-fold and three-fold symmetry centers. At the two-fold axis, a third electron-sparse region could be identified which is in accordance with literature reports (Giessen et al. 2019; McHugh et al. 2014; Sutter et al. 2008); however, this region seems to be closed by opposing monomer residues and is thus unlikely to act as a pore, as has been confirmed by another study (Giessen et al. 2019). The cargo densities observed in cargo-loaded particles were about 2.5 nm distanced from the shell densities, which in general is in agreement with findings in another study suggesting that the QtIMEF cargo is bound to the QtEnc shell via a 37 amino acid linker (Giessen et al. 2019).

4.2.3 QtIMEF cargo functionality

Compartmentalization is a well-known strategy to sequester toxic products, store nutrients or create a micro-environment for physiological processes; however, while eukaryotes mostly form membrane-encased organelles such as lysosomes, mitochondria or the nucleus, bacteria form proteinaceous compartments such as the carboxysome or encapsulins (Diekmann und Pereira-Leal 2013; Giessen 2016; McHugh et al. 2014; Sutter et al. 2008). Protein nano-compartments can self-assemble from one or few capsid monomers and are characterized by a precisely defined nano-architecture as well as by their highly uniform size and shape. In addition, protein cages like encapsulins, which were suggested to be among the first examples of such structures with a naturally encoded self-sorting peptide, can benefit from cargo auto-targeting with high selectivity and fidelity (Rurup et al. 2014).

While the *M. tuberculosis* encapsulin cargo is related to redox processes (Rosenkrands et al. 1998; Giessen 2016) and the DyP cargo of *Rhodococcus jostii* was shown to have lignin degradation activity (Rahmanpour und Bugg 2013), it was suggested that the encapsulin systems of *T. maritima*, *M. xanthus* as well as *P. furiosus* are involved in iron metabolism or detoxification as their cargos have been identified as ferritin-like proteins (McHugh et al. 2014; Sigmund et al. 2018; Sutter et al. 2008). Among the latter

encapsulins, the Mx encapsulin system with the shell protein MxA and its three cargos MxB, MxC, and MxD is probably the best-characterized regarding its role in iron metabolism (Sigmund et al. 2018; McHugh et al. 2014). Encapsulin expression in *Myxococcus xanthus* was observed to be upregulated upon starvation and the particles were shown to accumulate iron, possibly to protect the organism from oxidative stress (McHugh et al. 2014). While little is known about MxD, the two other two cargo proteins MxB and MxC possess ruberythrin/ferritin-like domains, and as they are both predicted to form only two α-helices each a dimerization was suggested yielding the known four-helix bundle ferritin-like motif (McHugh et al. 2014; Sigmund et al. 2018; Giessen und Silver 2017; Andrews 2010). Mx encapsulin cargos bind to the inside of the protein shell via C-terminal targeting peptides, and the iron deposits probably nucleate on the cargo proteins to form discrete granules with about 5 nm in diameter (McHugh et al. 2014). Experimental data suggested that Mx encapsulins can store up to 30,000 iron atoms per cage as a mixture with phosphate in a molar ratio of 4:1 ($Fe:P_i$), and as the cargo proteins resemble ferritins in their functionality, the formation of ferrihydrite has been suggested (McHugh et al. 2014; Sutter et al. 2008). Efficient iron loading of Mx encapsulins was also observed upon expression in mammalian cells; and interestingly, co-expression of either MxB or MxC was enough to facilitate iron sequestration inside the encapsulin shell whereas MxD did not lead to iron mineralization (Sigmund et al. 2018).

Apart from the *Myxococcus xanthus* encapsulin, the encapsulin system of *Quasibacillus thermotolerans* was also reported to form iron cores upon expression in *E. coli*, and notably the corresponding IMEF cargo does not contain known residues for iron-coordination (Giessen und Silver 2017). IMEF (iron-mineralizing encapsulin-associated Firmicute cargo) is a four-helix bundle protein and forms an unusual inter-subunit ferroxidase center upon dimerization (Giessen und Silver 2017; Giessen et al. 2019). While IMEF was first described as part of the encapsulin system of Bacillaceae MTCC 10057 which contained an additional ferredoxin cargo (Giessen und Silver 2017), it's crystal structure was later solved as part of the Qt encapsulin system (Giessen et al. 2019). In the present work, the QtIMEF cargo was characterized in more detail in mammalian cells in comparison to Mx encapsulin and ferritin. Quantification of the iron content of MxEnc and QtEnc expressed under comparable conditions showed that the Qt encapsulin system had accumulated almost twice as much iron per Enc particle than Mx encapsulin and almost 20-times as much as ferritin, which is more than reported for the expression of either encapsulin in *E. coli* (Giessen et al. 2019). However, it has to be noted that the iron content in QtEnc had previously been determined via electron energy loss spectroscopy (EELS) of encapsulins purified from *E. coli*. While the present work demonstrated that Qt encapsulins purified from mammalian and bacterial sources are structurally similar and can both encapsulate cargos, it is possible that expression in different host organisms affects the iron content, *e.g.* due to different intracellular iron concentrations or general iron availability. It should also be noted that in this work, cells were treated with iron for 36 h before encapsulins were isolated. However, as both Mx

and Qt encapsulins were treated similar in the scope of this work, the comparison between both encapsulin systems can indicate differences either in iron storage capacity or iron accumulation efficiency. Due to these findings, a ferroxidase assay was performed on purified encapsulin particles (**Figure 11A**). While QtEnc + QtIMEF showed a hyperbolic curve with a fast onset comparable to published results (Giessen et al. 2019), the Mx encapsulin system had a delayed onset with a lag-phase of about 5 min and a slower rise in signal. The QtEnc + QtIMEF system thus showed an earlier reaction onset in combination with a faster reaction catalysis, and accordingly another set of experiments demonstrated that Qt encapsulin can compete with the endogenous iron storage protein ferritin for cellular iron more efficiently than Mx encapsulin in low-iron conditions (**Figure 11C**). In this context, it is of interest to note that Firmicutes possessing an IMEF system lack the classical ferritins or bacterioferritins that usually play an important role in iron metabolism and thus probably rely on encapsulins as the main iron storage system (Giessen und Silver 2017), which could explain why the Qt encapsulin system has superior iron accumulation properties compared to *e.g.* MxEnc.

4.2.4 Cargo encapsulation in QtEnc and MxEnc

Self-sorting of associated cargo proteins in an important feature of encapsulin nano-compartments (Rurup et al. 2014), and apart from exceptions where the cargo is directly fused to the encapsulin shell monomer, conserved C-terminal motifs serve as peptide tags anchoring the cargos to conserved binding sites on the inner surface of the encapsulin lumen (Sigmund et al. 2018; Sutter et al. 2008; Giessen 2016; Giessen et al. 2019; McHugh et al. 2014; Rahmanpour und Bugg 2013). While the presence of such a highly conserved sequence is helpful to identify putative encapsulin cargos and has even been exploited to screen for encapsulin operons in organisms and to identify new encapsulin cargo types (Rahmanpour und Bugg 2013; Giessen und Silver 2017), the distinct sequence similarity raised the question whether the high selectivity of cargo self-sorting observed within an organism also has a high inter-encapsulin fidelity; that is, whether encapsulins can distinguish cargos based on different targeting sequences.

As the native cargos of Qt and Mx encapsulin are well-characterized and have already been used within this work, their inter-encapsulin fidelity as well as functionality have been tested. As the protein analysis of encapsulin pulldowns demonstrated, both encapsulins were capable of loading the respective non-native cargo proteins (**Figure 12**). While no densitometric analysis of the silver-stained gel was performed, the band intensities indicate that QtIMEF was encapsulated with higher efficiency inside Qt than Mx. On the other hand, the MxBCD cargo set seemed to be encapsulated in a slightly higher concentration in Qt, too. This could indicate that differences in packaging load might not be caused by a hampered recognition of the non-native targeting peptide but rather due to the larger volume of QtEnc allowing more space for cargo proteins. In agreement with previous reports for Mx encapsulin (Sigmund et al. 2018; McHugh et al.

2014), the cargo combination MxBCD as well as either of MxB or MxC alone were capable of mediating iron accumulation inside the Qt encapsulin shell. In addition, QtIMEF was capable of mediating iron loading of Mx shells. The band intensities on the BN-PAGE indicates that QtIMEF mediated more iron accumulation inside the Qt shell than either of the Mx cargos did. While QtIMEF was shown to be a more efficient ferroxidase than MxBCD in chapter 3.2.3, it cannot be excluded that differences in iron loading are also at least partially mediated by the different cargo encapsulation efficiency. Interestingly, QtIMEF seems to diminish the amount of accumulated inside Mx compared to the native MxBCD cargos despite its enhanced ferroxidase activity. While the different cargo loading efficiencies can again be a reason, it is also possible that either steric or size limitations hamper the activity of QtIMEF inside Mx, and it cannot be excluded that possible differences in the overall shell architecture, such as potential differences in pore sizes or pore hydrophobicity, further add to that. The inter-encapsulin cargo encapsulation efficiency was also addressed with a foreign fluorescent cargo (**Figure 13**). It could again be confirmed that both MxSig- and QtSig-cargos can be targeted to either of the encapsulin shells. Notably, the encapsulation inside Mx via the Qt signal peptide also led to the previously reported formation of T = 1 encapsulins (McHugh et al. 2014; Sigmund et al. 2018), which did not show a fluorescent signal indicating that probably no cargo was encapsulated. In conclusion, while the functionality of cross-targeted native and foreign encapsulin cargos has clearly been demonstrated, further characterizations of potentially different encapsulation efficiencies, the amount of iron accumulation as well as ferroxidase activity measurements are recommended to shed a light not only on the cargo functionality itself but also on possible synergies between cargo and shell further promoting iron accumulation.

4.2.5 Targeting of sub-cellular structures

While early publications suggested that encapsulins are being secreted as bacteriocins (Valdés-Stauber und Scherer 1994; Hicks et al. 1998), they were later shown in electron microscopy as electron-dense granules inside the respective host (McHugh et al. 2014; Giessen und Silver 2017) and their cytosolic localization was also confirmed for mammalian hosts (Lau et al. 2018; Sigmund et al. 2018), which seems reasonable due to their suggested involvement in various metabolic processes (Sutter et al. 2008; McHugh et al. 2014; Giessen 2016). However, controlling the sub-cellular localization of encapsulins could be beneficial not only with regards to manipulation of the iron mineral species as has been discussed for lysosomally localized ferritin earlier in this works, it might also be a useful feature in the scope of using encapsulins as generalizable nano-compartments in mammalian cell engineering. A C-terminal fusion of affinity tags for encapsulin purification has already been demonstrated also in the present work (Sigmund et al. 2018; Sigmund et al. 2019), and a previous report even demonstrated

cancer cell targeting via genetically modified *T. maritima* encapsulin displaying a SP94-peptide on its surface (Moon et al. 2014).

For sub-cellular targeting of encapsulins, a bipartite nuclear localization sequence (NLS) or a tripeptide peroxisomal transport signal (PTS) was C-terminally fused to the encapsulin shell as well as an artificial fluorescent cargo containing a terminal QtSig for encapsulation. Co-expression in mammalian cells revealed distinct fluorescent patterns clearly different from disperse cytosolic signal, and in the case of nuclear targeting the co-localizing with a DNA stain was shown, indicating successful sub-cellular targeting of cargo-loaded encapsulins into the nucleus (fig. 16, 17). Interestingly, omitting the NLS on the fluorescent cargo still yielded the same distinctly nuclear fluorescent pattern, whereas expression of cargo without shell led to fast degradation and thus no signal generation (data not shown). This raises questions regarding the still largely unknown process of encapsulin assembly and cargo loading. It seems clear that encapsulated protein cargos have to associate with an encapsulin intermediate during the shell assembly as they cannot fit through the pores of the fully-assembled nano-cages. For QtEnc, a different study reported 42 IMEF densities per shell, which would equal one cargo per capsomer (QtEnc consists of 12 pentamers and 30 hexamers) (Giessen et al. 2019), and a similar stoichiometry was observed for the T=1 encapsulin of *B. linens* (Rurup et al. 2014). However, in the present work a shell:cargo monomer stoichiometry of almost 1 was observed. Another publication reported low molecular mass species upon denaturation of *R. jostii* encapsulin, which was attributed to dimeric species (Rahmanpour und Bugg 2013). Based on the presented data, it might thus be possible that encapsulin intermediates – either dimers or fully-formed capsomers – bind to the cargo proteins tightly enough to facilitate their co-transport into the nucleus even if the cargo does not carry an NLS. In a previous chapter of this work, the possibility of inter-encapsulin cargo targeting as well as potential differences in cargo encapsulation efficiency were discussed. Continuing this study with *e.g.* differently-sized cargos or encapsulation signals from other species might thus reveal more information not only on the encapsulin assembly process and possible nuclear import routs, but also about the interaction strength of different encapsulation signals with the respective shells.

4.3 Application of iron-loaded encapsulins for MRI

The Mx encapsulin system has already been shown to yield detectable iron-based MRI contrast in HEK cells as well as in xenografts in rat brain (Sigmund et al. 2018). As discussed in the previous chapter, the Qt encapsulin system can load more iron in its cavity, and QtEnc expressing cells show higher iron content than MxEnc expressing cells.

Determination of the transverse relaxivity r_2 of iron-loaded Qt and Mx encapsulins compared to the ubiquitous iron storage protein ferritin revealed that QtEnc has the highest relaxivity per protein shell followed by MxEnc, and they have a 23- and 13-times higher relaxivity than ferritin, respectively. These findings match the observed differences in iron accumulation efficiency (**Figure 18**). However, normalized to the respective protein iron contents both encapsulins showed a 18 % higher relaxivity per iron than ferrihydrite-containing ferritin, which was unexpected as encapsulins were suggested to also form ferrihydrite (Sutter et al. 2008; McHugh et al. 2014). It seems unlikely that magnetite has formed inside encapsulins, because an exchange of ferrihydrite to magnetite inside ferritin has led to a relaxivity increase of more than 400 % in a previous publication (Massner et al. 2018), which is orders of magnitudes higher than the differences observed in this work. However, this finding still rises questions regarding the identity of the mineral species formed by encapsulins, and it is recommended to perform further magnetometry analyses on encapsulins such as Raman spectroscopy or SQUID measurements to determine the identity of the formed iron oxide. Similar trends were also observed when imaging cells expressing the encapsulin systems, where the highest MRI contrast was obtained from cells expressing Qt encapsulin. These findings demonstrate that both Qt and Mx encapsulin could potentially be exploited as a fully genetically encoded contrast agent for magnetic resonance imaging. While it can be speculated that the mineralization of magnetite inside the encapsulin shell would lead to even higher contrast generation based on observations for ferritin and magnetoferritin (Massner et al. 2018), the presented data indicate that ferrihydrite-derived contrast can be significantly improved by accumulation effects.

4.4 Application of encapsulins for EM

While electron microscopy has become a valuable tool to study cellular processes (Beck und Baumeister 2016; Robinson et al. 2007) and even cell circuits (Denk et al. 2012; Helmstaedter 2013; Zheng et al. 2018; Tamura et al. 2015), this technique still lacks a tool box of genetic reporters equivalent to fluorescent proteins and optical reporters (Tsien 1998; Shaner et al. 2007). While the ubiquitous iron storage protein ferritin has been proposed as a genetic EM contrast agent in different organism, its small size and the limited electron density generated by its ferrihydrite mineral core are difficult to differentiate from other well-contrasted cellular structures (Wang et al. 2011; Matsumoto et al. 2015; Clarke und Royle 2018; Jutz et al. 2015).

In contrast, encapsulin nano-compartments of different origins have been visualized by electron microscopy not only as purified particles (Namba et al. 2005; McHugh et al. 2014; Sutter et al. 2008; Rurup et al. 2014; Lau et al. 2018) but also in bacteria, where they appeared as small, electron-dense particles (McHugh et al. 2014; Giessen und

Silver 2017). In the scope of the present work, both Qt and Mx encapsulins were visualized in HEK 293T cells in TEM. The encapsulin nano-compartments were visible as spherical particles of defined sizes and high electron density (**Figure 19**). Notably, manual segmentation of 100 particles revealed that the two encapsulin systems have a clearly distinguishable size and differ in their mean grey values. While these findings can be expected as the Qt encapsulin was shown to be larger and to accumulate more iron in the previous chapters, the fact that these features are clearly discernible in TEM could enable multiplexed imaging with two fully-genetic markers. While further studies will be necessary, it can also be reasoned that encapsulin shells devoid of iron could still be detected in TEM due to their size and distinct shape, which would give additional multiplexing capabilities. In addition, encapsulins have been shown to load fully-functional foreign cargos, so targeting of different other metal binders into the encapsulin lumen could be possible. By coupling TEM for example with energy-dispersive x-ray spectroscopy (TEM-EDX), it could be possible to distinguish encapsulins based on the incorporated metals, which in combination with the two different available encapsulin sizes opens a large combinatorial space. However, as the targeting of cargos via native encapsulation signals is not inter-encapsulin specific as shown in this work, an additional strategy would have to be developed to ensure the fidelity of cargo loading. Such self-sorting cargo assignments in a multi-encapsulin scenario could be mediated by establishing an artificial targeting system, for example via coiled-coil protein heterodimers which were reported to have excellent specificity (Chen et al. 2019; Ljubetič et al. 2017).

Bibliography

Literaturverzeichnis

Akita, Fusamichi; Chong, Khoon Tee; Tanaka, Hideaki; Yamashita, Eiki; Miyazaki, Naoyuki; Nakaishi, Yuichiro et al. (2007): The Crystal Structure of a Virus-like Particle from the Hyperthermophilic Archaeon Pyrococcus furiosus Provides Insight into the Evolution of Viruses. In: *Journal of molecular biology* 368 (5), S. 1469–1483. DOI: 10.1016/j.jmb.2007.02.075.

Andrews, Simon C. (2010): The Ferritin-like superfamily: Evolution of the biological iron storeman from a rubrerythrin-like ancestor. In: *Biochimica et biophysica acta* 1800 (8), S. 691–705. DOI: 10.1016/j.bbagen.2010.05.010.

Asano, Takeshi; Komatsu, Masaaki; Yamaguchi-Iwai, Yuko; Ishikawa, Fuyuki; Mizushima, Noboru; Iwai, Kazuhiro (2011): Distinct mechanisms of ferritin delivery to lysosomes in iron-depleted and iron-replete cells. In: *Molecular and cellular biology* 31 (10), S. 2040–2052. DOI: 10.1128/MCB.01437-10.

Austin, Cary D.; Wen, Xiaohui; Gazzard, Lewis; Nelson, Christopher; Scheller, Richard H.; Scales, Suzie J. (2005): Oxidizing potential of endosomes and lysosomes limits intracellular cleavage of disulfide-based antibody–drug conjugates. In: *Proceedings of the National Academy of Sciences of the United States of America* 102 (50), S. 17987. DOI: 10.1073/pnas.0509035102.

Baader, S. L.; Bill, E.; Trautwein, A. X.; Bruchelt, G.; Matzanke, B. F. (1996): Mobilization of iron from cellular ferritin by ascorbic acid in neuroblastoma SK-N-SH cells: an EPR study. In: *FEBS Letters* 381 (1-2), S. 131–134. DOI: 10.1016/0014-5793(96)00098-1.

Badu-Boateng, Charles; Naftalin, Richard J. (2019): Ascorbate and ferritin interactions: Consequences for iron release in vitro and in vivo and implications for inflammation. In:

Free radical biology & medicine 133, S. 75–87. DOI: 10.1016/j.freeradbiomed.2018.09.041.

Badu-Boateng, Charles; Pardalaki, Sofia; Wolf, Claude; Lajnef, Sonia; Peyrot, Fabienne; Naftalin, Richard J. (2017): Labile iron potentiates ascorbate-dependent reduction and mobilization of ferritin iron. In: *Free Radical Biology and Medicine* 108, S. 94–109. DOI: 10.1016/j.freeradbiomed.2017.03.015.

Beck, Martin; Baumeister, Wolfgang (2016): Cryo-Electron Tomography: Can it Reveal the Molecular Sociology of Cells in Atomic Detail? In: *Trends in cell biology* 26 (11), S. 825–837. DOI: 10.1016/j.tcb.2016.08.006.

Bhattacharya, Abhishek; Aghayeva, Ulkar; Berghoff, Emily G.; Hobert, Oliver (2019): Plasticity of the Electrical Connectome of C. elegans. In: *Cell* 176 (5), 1174-1189.e16. DOI: 10.1016/j.cell.2018.12.024.

Bienfait, H. F.; van den Briel, M. L. (1980): Rapid mobilization of ferritin iron by ascorbate in the presence of oxygen. In: *Biochimica et biophysica acta* 631 (3), S. 507–510. DOI: 10.1016/0304-4165(80)90028-8.

Bobtelsky, M.; Jordan, J. (1947): The Structure and Behavior of Ferric Tartrate and Citrate Complexes in Dilute Solutions1. In: *Journal of the American Chemical Society* 69 (10), S. 2286–2290. DOI: 10.1021/ja01202a014.

Bouchet-Marquis, Cédric; Pagratis, Maria; Kirmse, Robert; Hoenger, Andreas (2012): Metallothionein as a clonable high-density marker for cryo-electron microscopy. In: *J Struct Biol* 177 (1), S. 119–127. DOI: 10.1016/j.jsb.2011.10.007.

Boyer, Rodney F.; J. McCleary, Craig (1987): Superoxide ion as a primary reductant in ascorbate-mediated ferretin iron release. In: *Free Radical Biology and Medicine* 3 (6), S. 389–395. DOI: 10.1016/0891-5849(87)90017-7.

Brocard, Cécile; Hartig, Andreas (2006): Peroxisome targeting signal 1: Is it really a simple tripeptide? In: *Biochimica et Biophysica Acta (BBA) - Molecular Cell Research* 1763 (12), S. 1565–1573. DOI: 10.1016/j.bbamcr.2006.08.022.

Cai, Yao; Cao, Changqian; He, Xiaoqing; Yang, Caiyun; Tian, Lanxiang; Zhu, Rixiang; Pan, Yongxin (2015): Enhanced magnetic resonance imaging and staining of cancer cells using ferrimagnetic H-ferritin nanoparticles with increasing core size. In: *Int J Nanomedicine* 10, S. 2619–2634. DOI: 10.2147/IJN.S80025.

Cao, Changqian; Wang, Xuxia; Cai, Yao; Sun, Lei; Tian, Lanxiang; Wu, Hao et al. (2014): Targeted in vivo imaging of microscopic tumors with ferritin-based nanoprobes across biological barriers. In: *Advanced materials (Deerfield Beach, Fla.)* 26 (16), S. 2566–2571. DOI: 10.1002/adma.201304544.

Carmona, Unai; Le Li; Zhang, Lianbing; Knez, Mato (2014): Ferritin light-chain subunits: key elements for the electron transfer across the protein cage. In: *Chemical Communications* 50 (97), S. 15358–15361. DOI: 10.1039/C4CC07996E.

Chen, Zibo; Boyken, Scott E.; Jia, Mengxuan; Busch, Florian; Flores-Solis, David; Bick, Matthew J. et al. (2019): Programmable design of orthogonal protein heterodimers. In: *Nature* 565 (7737), S. 106–111. DOI: 10.1038/s41586-018-0802-y.

Chiang, Ann-Shyn; Lin, Chih-Yung; Chuang, Chao-Chun; Chang, Hsiu-Ming; Hsieh, Chang-Huain; Yeh, Chang-Wei et al. (2011): Three-Dimensional Reconstruction of Brain-wide Wiring Networks in Drosophila at Single-Cell Resolution. In: *Current Biology* 21 (1), S. 1–11. DOI: 10.1016/j.cub.2010.11.056.

Clarke, Nicholas I.; Royle, Stephen J. (2018): FerriTag is a new genetically-encoded inducible tag for correlative light-electron microscopy. In: *Nature communications* 9 (1), S. 2604. DOI: 10.1038/s41467-018-04993-0.

Cohen, Batya; Dafni, Hagit; Meir, Gila; Harmelin, Alon; Neeman, Michal (2005): Ferritin as an endogenous MRI reporter for noninvasive imaging of gene expression in C6 glioma tumors. In: *Neoplasia* 7 (2), S. 109–117. DOI: 10.1593/neo.04436.

Cohen, Batya; Ziv, Keren; Plaks, Vicki; Israely, Tomer; Kalchenko, Vyacheslav; Harmelin, Alon et al. (2007): MRI detection of transcriptional regulation of gene expression in transgenic mice. In: *Nature medicine* 13 (4), S. 498–503. DOI: 10.1038/nm1497.

Cornell, R. M.; Schwertmann, Udo (2003): The iron oxides. Structure, properties, reactions, occurrences, and uses. 2nd, completely rev. and extended ed. Weinheim: Wiley-VCH.

Crichton, Robert R. (1984): Iron uptake and utilization by mammalian cells II. Intracellular iron utilization. In: *Trends in Biochemical Sciences* 9 (6), S. 283–286. DOI: 10.1016/0968-0004(84)90167-1.

Cudennec, Yannick; Lecerf, André (2005): Topotactic transformations of goethite and lepidocrocite into hematite and maghemite. In: *Solid State Sciences* 7 (5), S. 520–529. DOI: 10.1016/j.solidstatesciences.2005.02.002.

Cudennec, Yannick; Lecerf, André (2006): The transformation of ferrihydrite into goethite or hematite, revisited. In: *Journal of Solid State Chemistry* 179 (3), S. 716–722. DOI: 10.1016/j.jssc.2005.11.030.

D'Angelo, Maximiliano A.; Raices, Marcela; Panowski, Siler H.; Hetzer, Martin W. (2009): Age-dependent deterioration of nuclear pore complexes causes a loss of nuclear integrity in postmitotic cells. In: *Cell* 136 (2), S. 284–295. DOI: 10.1016/j.cell.2008.11.037.

Denk, Winfried; Briggman, Kevin L.; Helmstaedter, Moritz (2012): Structural neurobiology: missing link to a mechanistic understanding of neural computation. In: *Nature reviews. Neuroscience* 13 (5), S. 351–358. DOI: 10.1038/nrn3169.

Diekmann, Yoan; Pereira-Leal, José B. (2013): Evolution of intracellular compartmentalization. In: *Biochem J* 449 (2), S. 319–331. DOI: 10.1042/BJ20120957.

Djurdjevic, Preorag (1990): The complexation between iron(III) ion and glycine in nitrate medium. In: *Transition Metal Chemistry* 15 (5), S. 345–350. DOI: 10.1007/BF01177459.

Dognin, Janine; Crichton, Robert R. (1975): Mobilisation of iron from ferritin fractions of defined iron content by biological reductants. In: *FEBS Letters* 54 (2), S. 234–236. DOI: 10.1016/0014-5793(75)80081-0.

Faivre, Damien (2016): Iron oxides: from nature to applications: John Wiley & Sons.

Fan, Kelong; Cao, Changqian; Pan, Yongxin; Di Lu; Yang, Dongling; Feng, Jing et al. (2012): Magnetoferritin nanoparticles for targeting and visualizing tumour tissues. In: *Nature Nanotechnology* 7 (11), S. 765. DOI: 10.1038/nnano.2012.204.

Fang, Tao; Lu, Xiaotang; Berger, Daniel; Gmeiner, Christina; Cho, Julia; Schalek, Richard et al. (2018): Nanobody immunostaining for correlated light and electron microscopy with preservation of ultrastructure. In: *Nature methods* 15 (12), S. 1029–1032. DOI: 10.1038/s41592-018-0177-x.

Feng, Yupeng; Liu, Qicai; Zhu, Junfeng; Xie, Fukang; Li, Li (2012): Efficiency of ferritin as an MRI reporter gene in NPC cells is enhanced by iron supplementation. In: *Journal of biomedicine & biotechnology* 2012, S. 434878. DOI: 10.1155/2012/434878.

Giessen, Tobias W. (2016): Encapsulins: microbial nanocompartments with applications in biomedicine, nanobiotechnology and materials science. In: *Curr Opin Chem Biol* 34, S. 1–10. DOI: 10.1016/j.cbpa.2016.05.013.

Giessen, Tobias W.; Orlando, Benjamin J.; Verdegaal, Andrew A.; Chambers, Melissa G.; Gardener, Jules; Bell, David C. et al. (2019): Large protein organelles form a new iron sequestration system with high storage capacity. In: *eLife* 8, e46070. DOI: 10.7554/eLife.46070.

Giessen, Tobias W.; Silver, Pamela A. (2017): Widespread distribution of encapsulin nanocompartments reveals functional diversity. In: *Nature Microbiology* 2 (6), S. 17029. DOI: 10.1038/nmicrobiol.2017.29.

Golubitskii, G. B.; Budko, E. V.; Basova, E. M.; Kostarnoi, A. V.; Ivanov, V. M. (2007): Stability of ascorbic acid in aqueous and aqueous-organic solutions for quantitative determination. In: *Journal of Analytical Chemistry* 62 (8), S. 742–747. DOI: 10.1134/S1061934807080096.

Graham, R. M.; Morgan, E. H.; Baker, E. (1998): Characterisation of citrate and iron citrate uptake by cultured rat hepatocytes. In: *Journal of hepatology* 29 (4), S. 603–613. DOI: 10.1016/s0168-8278(98)80156-6.

Granick, S. (1942): FERRITIN: I. PHYSICAL AND CHEMICAL PROPERTIES OF HORSE SPLEEN FERRITIN. In: *Journal of Biological Chemistry* 146 (2), S. 451–461. Online verfügbar unter http://www.jbc.org/content/146/2/451.short.

Hagiwara, Haruo; Aoki, Takeo; Suzuki, Takeshi; Takata, Kuniaki (2010): Double-label immunoelectron microscopy for studying the colocalization of proteins in cultured cells. In: Immunoelectron Microscopy: Springer, S. 249–257.

Hamm, Randall E.; Shull, Charles M.; Grant, David M. (1954): Citrate Complexes with Iron(II) and Iron(III)1. In: *Journal of the American Chemical Society* 76 (8), S. 2111–2114. DOI: 10.1021/ja01637a021.

Hansel, Colleen M.; Benner, Shawn G.; Fendorf, Scott (2005): Competing Fe (II)-induced mineralization pathways of ferrihydrite. In: *Environmental science & technology* 39 (18), S. 7147–7153. DOI: 10.1021/es050666z.

Hartmann, Carolin (2019): Zerstörungsfreie Analyse des Eisenkerns von Ferritin und Magnetoferritin mittels Raman-Mikrospektroskopie. Dissertation. Technische Universität München, München. Institut für Wasserchemie und Chemische Balneologie. Online verfügbar unter http://mediatum.ub.tum.de/?id=1510031.

Hartmann, Carolin; Elsner, Martin; Niessner, Reinhard; Ivleva, Natalia P. (2019): Nondestructive Chemical Analysis of the Iron-Containing Protein Ferritin Using Raman Microspectroscopy. In: *Applied Spectroscopy* 74 (2), S. 193–203. DOI: 10.1177/0003702818823203.

Heinemann, Joshua; Maaty, Walid S.; Gauss, George H.; Akkaladevi, Narahari; Brumfield, Susan K.; Rayaprolu, Vamseedhar et al. (2011): Fossil record of an archaeal HK97-like provirus. In: *Virology* 417 (2), S. 362–368. DOI: 10.1016/j.virol.2011.06.019.

Helmstaedter, Moritz (2013): Cellular-resolution connectomics: challenges of dense neural circuit reconstruction. In: *Nature methods* 10 (6), S. 501–507. DOI: 10.1038/nmeth.2476.

Helmstaedter, Moritz; Briggman, Kevin L.; Turaga, Srinivas C.; Jain, Viren; Seung, H. Sebastian; Denk, Winfried (2013): Connectomic reconstruction of the inner plexiform layer in the mouse retina. In: *Nature* 500 (7461), S. 168–174. DOI: 10.1038/nature12346.

Hicks, P. M.; Rinker, K. D.; Baker, J. R.; Kelly, R. M. (1998): Homomultimeric protease in the hyperthermophilic bacterium Thermotoga maritima has structural and amino acid sequence homology to bacteriocins in mesophilic bacteria. In: *FEBS Letters* 440 (3), S. 393–398. DOI: 10.1016/s0014-5793(98)01451-3.

Honarmand Ebrahimi, Kourosh; Hagedoorn, Peter-Leon; Hagen, Wilfred R. (2015): Unity in the biochemistry of the iron-storage proteins ferritin and bacterioferritin. In: *Chemical reviews* 115 (1), S. 295–326. DOI: 10.1021/cr5004908.

Iordanova, Bistra; Ahrens, Eric T. (2012): In vivo magnetic resonance imaging of ferritin-based reporter visualizes native neuroblast migration. In: *Neuroimage* 59 (2), S. 1004–1012. DOI: 10.1016/j.neuroimage.2011.08.068.

Ivanov, M. A.; Kosoy, A. L. (1975): The structure of the iron(III) complex with sodium tartrate (FeTNa). In: *Acta Cryst. B* 31 (12), S. 2843–2848. DOI: 10.1107/S0567740875009028.

Joesch, Maximilian; Mankus, David; Yamagata, Masahito; Shahbazi, Ali; Schalek, Richard; Suissa-Peleg, Adi et al. (2016): Reconstruction of genetically identified neurons imaged by serial-section electron microscopy. In: *eLife* 5. DOI: 10.7554/eLife.15015.

Jutz, Günther; van Rijn, Patrick; Santos Miranda, Barbara; Böker, Alexander (2015): Ferritin: a versatile building block for bionanotechnology. In: *Chemical reviews* 115 (4), S. 1653–1701. DOI: 10.1021/cr400011b.

Kasthuri, Narayanan; Hayworth, Kenneth Jeffrey; Berger, Daniel Raimund; Schalek, Richard Lee; Conchello, José Angel; Knowles-Barley, Seymour et al. (2015): Saturated Reconstruction of a Volume of Neocortex. In: *Cell* 162 (3), S. 648–661. DOI: 10.1016/j.cell.2015.06.054.

Kukkadapu, Ravi K.; Zachara, John M.; Fredrickson, James K.; Smith, Steven C.; Dohnalkova, Alice C.; Russell, Colleen K. (2003): Transformation of 2-line ferrihydrite to 6-line ferrihydrite under oxic and anoxic conditions. In: *American Mineralogist* 88 (11-12), S. 1903–1914.

Lam, Stephanie S.; Martell, Jeffrey D.; Kamer, Kimberli J.; Deerinck, Thomas J.; Ellisman, Mark H.; Mootha, Vamsi K.; Ting, Alice Y. (2015): Directed evolution of APEX2 for electron microscopy and proximity labeling. In: *Nature methods* 12 (1), S. 51–54. DOI: 10.1038/nmeth.3179.

Lametschwandtner, G.; Brocard, C.; Fransen, M.; van Veldhoven, P.; Berger, J.; Hartig, A. (1998): The difference in recognition of terminal tripeptides as peroxisomal targeting signal 1 between yeast and human is due to different affinities of their receptor Pex5p to the cognate signal and to residues adjacent to it. In: *The Journal of biological chemistry* 273 (50), S. 33635–33643. DOI: 10.1074/jbc.273.50.33635.

Laroff, G. P.; Fessenden, R. W.; Schuler, R. H. (1972): The electron spin resonance spectra of radical intermediates in the oxidation of ascorbic acid and related substances. In: *Journal of the American Chemical Society* 94 (26), S. 9062–9073. DOI: 10.1021/ja00781a013.

Lau, Yu Heng; Giessen, Tobias W.; Altenburg, Wiggert J.; Silver, Pamela A. (2018): Prokaryotic nanocompartments form synthetic organelles in a eukaryote. In: *Nature communications* 9 (1), S. 1311. DOI: 10.1038/s41467-018-03768-x.

Laufberger, Vilem (1937): Sur la cristallisation de la ferritine. In: *Soc Chim Biol* 19, S. 1575–1582.

Laurent, Sophie; Forge, Delphine; Port, Marc; Roch, Alain; Robic, Caroline; Vander Elst, Luce; Muller, Robert N. (2008): Magnetic Iron Oxide Nanoparticles: Synthesis, Stabilization, Vectorization, Physicochemical Characterizations, and Biological Applications. In: *Chemical reviews* 108 (6), S. 2064–2110. DOI: 10.1021/cr068445e.

Lawrence, Rosalie E.; Zoncu, Roberto (2019): The lysosome as a cellular centre for signalling, metabolism and quality control. In: *Nature Cell Biology* 21 (2), S. 133–142. DOI: 10.1038/s41556-018-0244-7.

Lawson, D. M.; Treffry, A.; Artymiuk, P. J.; Harrison, P. M.; Yewdall, S. J.; Luzzago, A. et al. (1989): Identification of the ferroxidase centre in ferritin. In: *FEBS Letters* 254 (1-2), S. 207–210. DOI: 10.1016/0014-5793(89)81040-3.

Lawson, David M.; Artymiuk, Peter J.; Yewdall, Stephen J.; Smith, John M. A.; Livingstone, J. Craig; Treffry, Amyra et al. (1991): Solving the structure of human H ferritin by genetically engineering intermolecular crystal contacts. In: *Nature* 349 (6309), S. 541–544. DOI: 10.1038/349541a0.

Lee, Alasdair P.; Webb, John; Macey, D. J.; van Bronswijk, Wilhelm; Savarese, Angela R.; Witt, G. Charmaine de (1998): In situ Raman spectroscopic studies of the teeth of the chiton Acanthopleura hirtosa. In: *JBIC Journal of Biological Inorganic Chemistry* 3 (6), S. 614–619. DOI: 10.1007/s007750050274.

Liu, Hui; Li, Ping; Zhu, Meiying; Wei, Yu; Sun, Yuhan (2007): Fe(II)-induced transformation from ferrihydrite to lepidocrocite and goethite. In: *Journal of Solid State Chemistry* 180 (7), S. 2121–2128. DOI: 10.1016/j.jssc.2007.03.022.

Liu, Hui; Wei, Yu; Sun, Yuhan (2005): The Formation of hematite from ferrihydrite using Fe(II) as a catalyst. In: *Journal of Molecular Catalysis A: Chemical* 226 (1), S. 135–140. DOI: 10.1016/j.molcata.2004.09.019.

Ljubetič, Ajasja; Lapenta, Fabio; Gradišar, Helena; Drobnak, Igor; Aupič, Jana; Strmšek, Žiga et al. (2017): Design of coiled-coil protein-origami cages that self-assemble in vitro and in vivo. In: *Nature biotechnology* 35 (11), S. 1094–1101. DOI: 10.1038/nbt.3994.

Lloyd, J. B. (1986): Disulphide reduction in lysosomes. The role of cysteine. In: *Biochem J* 237 (1), S. 271–272. DOI: 10.1042/bj2370271.

Lockwood, Thomas D. (2013): Lysosomal metal, redox and proton cycles influencing the CysHis cathepsin reaction. In: *Metallomics* 5 (2), S. 110–124. DOI: 10.1039/C2MT20156A.

Lončar Nikola; Rozeboom Henriette J.; Franken Linda E.; Stuart Marc C. A.; Fraaije Marco (2020): Molecular Packaging of Biocatalysts Using a Robust Protein Cage. DOI: 10.26434/chemrxiv.12063243.v1.

Martell, Jeffrey D.; Deerinck, Thomas J.; Sancak, Yasemin; Poulos, Thomas L.; Mootha, Vamsi K.; Sosinsky, Gina E. et al. (2012): Engineered ascorbate peroxidase as a genetically encoded reporter for electron microscopy. In: *Nature biotechnology* 30 (11), S. 1143–1148. DOI: 10.1038/nbt.2375.

Massner, Christoph; Sigmund, Felix; Pettinger, Susanne; Seeger, Markus; Hartmann, Carolin; Ivleva, Natalia P. et al. (2018): Genetically Controlled Lysosomal Entrapment of Superparamagnetic Ferritin for Multimodal and Multiscale Imaging and Actuation with Low Tissue Attenuation. In: *Adv. Funct. Mater.* 28 (19), S. 1706793. DOI: 10.1002/adfm.201706793.

Masuda, Taro; Goto, Fumiyuki; Yoshihara, Toshihiro; Mikami, Bunzo (2010): The universal mechanism for iron translocation to the ferroxidase site in ferritin, which is mediated by the well conserved transit site. In: *Biochemical and biophysical research communications* 400 (1), S. 94–99. DOI: 10.1016/j.bbrc.2010.08.017.

Matsumoto, Yuri; Chen, Ritchie; Anikeeva, Polina; Jasanoff, Alan (2015): Engineering intracellular biomineralization and biosensing by a magnetic protein. In: *Nature communications* 6 (1), S. 8721. DOI: 10.1038/ncomms9721.

Mazur, Abraham; Baez, Silvio; Shorr, Ephraim (1955): The Mechanism of Iron Release from Ferritin as Related to its Biological Properties. In: *Journal of Biological Chemistry* 213 (1), S. 147–160. Online verfügbar unter http://www.jbc.org/content/213/1/147.short.

McCarthy, Ryan C.; Kosman, Daniel J. (2015): Mechanisms and regulation of iron trafficking across the capillary endothelial cells of the blood-brain barrier. In: *Frontiers in molecular neuroscience* 8, S. 31. DOI: 10.3389/fnmol.2015.00031.

McHugh, Colleen A.; Fontana, Juan; Nemecek, Daniel; Cheng, Naiqian; Aksyuk, Anastasia A.; Heymann, J. Bernard et al. (2014): A virus capsid-like nanocompartment that stores iron and protects bacteria from oxidative stress. In: *The EMBO journal* 33 (17), S. 1896–1911. DOI: 10.15252/embj.201488566.

Meguro, Reiko; Asano, Yoshiya; Odagiri, Saori; Li, Chengtai; Iwatsuki, Hiroyasu; Shoumura, Kazuhiko (2007): Nonheme-iron histochemistry for light and electron microscopy: a historical, theoretical and technical review. In: *Archives of histology and cytology* 70 (1), S. 1–19. DOI: 10.1679/aohc.70.1.

Meister, Markus; Clapham, David E. (2016): Physical limits to magnetogenetics. In: *eLife* 5, e17210. DOI: 10.7554/eLife.17210.

Meldrum, F. C.; Heywood, B. R.; Mann, S. (1992): Magnetoferritin: in vitro synthesis of a novel magnetic protein. In: *Science (New York, N.Y.)* 257 (5069), S. 522–523. DOI: 10.1126/science.1636086.

Moon, Hyojin; Lee, Jisu; Min, Junseon; Kang, Sebyung (2014): Developing Genetically Engineered Encapsulin Protein Cage Nanoparticles as a Targeted Delivery Nanoplatform. In: *Biomacromolecules* 15 (10), S. 3794–3801. DOI: 10.1021/bm501066m.

Namba, Kazunori; Hagiwara, Kyoji; Tanaka, Hideaki; Nakaishi, Yuichiro; Chong, Khoon Tee; Yamashita, Eiki et al. (2005): Expression and molecular characterization of spherical particles derived from the genome of the hyperthermophilic euryarchaeote Pyrococcus furiosus. In: *Journal of biochemistry* 138 (2), S. 193–199. DOI: 10.1093/jb/mvi111.

Naumova, Anna V.; Reinecke, Hans; Yarnykh, Vasily; Deem, Jennifer; Yuan, Chun; Murry, Charles E. (2010): Ferritin overexpression for noninvasive magnetic resonance imaging-based tracking of stem cells transplanted into the heart. In: *Molecular imaging* 9 (4), S. 201–210.

Nemoto, Michiko; Ren, Dongni; Herrera, Steven; Pan, Songqin; Tamura, Takashi; Inagaki, Kenji; Kisailus, David (2019): Integrated transcriptomic and proteomic analyses of a molecular mechanism of radular teeth biomineralization in Cryptochiton stelleri. In: *Scientific reports* 9 (1), S. 856. DOI: 10.1038/s41598-018-37839-2.

Nichols, Robert J.; LaFrance, Benjamin; Phillips, Naiya R.; Oltrogge, Luke M.; Valentin-Alvarado, Luis E.; Bischoff, Amanda J. et al. (2020): Discovery and characterization of a novel family of prokaryotic nanocompartments involved in sulfur metabolism. In: *bioRxiv*, 2020.05.24.113720. DOI: 10.1101/2020.05.24.113720.

Niederer, W. (1970): Ferritin: iron incorporation and iron release. In: *Experientia* 26 (2), S. 218–220. DOI: 10.1007/bf01895596.

Octave, Jean-Noël; Schneider, Yves-Jacques; Trouet, André; Crichton, Robert R. (1983): Iron uptake and utilization by mammalian cells. I: Cellular uptake of transferrin and iron. In: *Trends in Biochemical Sciences* 8 (6), S. 217–220. DOI: 10.1016/0968-0004(83)90217-7.

Ostwald, Wilhelm (1897): Studien über die Bildung und Umwandlung fester Körper. In: *Zeitschrift für physikalische Chemie* 22 (1), S. 289–330.

Pallotto, Marta; Watkins, Paul V.; Fubara, Boma; Singer, Joshua H.; Briggman, Kevin L.; Häusser, Michael (2015): Extracellular space preservation aids the connectomic analysis of neural circuits. In: *eLife* 4, e08206. DOI: 10.7554/eLife.08206.

Pape, L.; Multani, J. S.; Stitt, C.; Saltman, P. (1968): In vitro reconstitution of ferritin. In: *Biochemistry* 7 (2), S. 606–612. DOI: 10.1021/bi00842a014.

Rahmanpour, Rahman; Bugg, Timothy D. H. (2013): Assembly in vitro of Rhodococcus jostii RHA1 encapsulin and peroxidase DypB to form a nanocompartment. In: *The FEBS journal* 280 (9), S. 2097–2104. DOI: 10.1111/febs.12234.

Reif, David W. (1992): Ferritin as a source of iron for oxidative damage. In: *Free radical biology & medicine* 12 (5), S. 417–427. DOI: 10.1016/0891-5849(92)90091-t.

Robinson, Carol V.; Sali, Andrej; Baumeister, Wolfgang (2007): The molecular sociology of the cell. In: *Nature* 450 (7172), S. 973–982. DOI: 10.1038/nature06523.

Roginsky, V. A.; Barsukova, T. K.; Bruchelt, G.; Stegmann, H. B. (1997): Iron bound to ferritin catalyzes ascorbate oxidation: effects of chelating agents. In: *Biochimica et biophysica acta* 1335 (1-2), S. 33–39. DOI: 10.1016/s0304-4165(96)00120-1.

Rosenkrands, Ida; Rasmussen, Peter Birk; Carnio, Markus; Jacobsen, Susanne; Theisen, Michael; Andersen, Peter (1998): Identification and Characterization of a 29-Kilodalton Protein from Mycobacterium tuberculosis Culture Filtrate Recognized by Mouse Memory Effector Cells. In: *Infection and Immunity* 66 (6), S. 2728. DOI: 10.1128/IAI.66.6.2728-2735.1998.

Rurup, W. Frederik; Snijder, Joost; Koay, Melissa S. T.; Heck, Albert J. R.; Cornelissen, Jeroen J. L. M. (2014): Self-Sorting of Foreign Proteins in a Bacterial Nanocompartment. In: *Journal of the American Chemical Society* 136 (10), S. 3828–3832. DOI: 10.1021/ja410891c.

Ryan, Kerrianne; Lu, Zhiyuan; Meinertzhagen, Ian A.; Marder, Eve (2016): The CNS connectome of a tadpole larva of Ciona intestinalis (L.) highlights sidedness in the brain of a chordate sibling. In: *eLife* 5, e16962. DOI: 10.7554/eLife.16962.

Schwertmann, U.; Murad, E. (1983): Effect of pH on the Formation of Goethite and Hematite from Ferrihydrite. In: *Clays and Clay Minerals* 31 (4), S. 277–284. DOI: 10.1346/CCMN.1983.0310405.

Shahidi, Réza; Williams, Elizabeth A.; Conzelmann, Markus; Asadulina, Albina; Verasztó, Csaba; Jasek, Sanja et al. (2015): A serial multiplex immunogold labeling method for identifying peptidergic neurons in connectomes. In: *eLife* 4, e11147. DOI: 10.7554/eLife.11147.

Shaner, Nathan C.; Patterson, George H.; Davidson, Michael W. (2007): Advances in fluorescent protein technology. In: *Journal of Cell Science* 120 (24), S. 4247. DOI: 10.1242/jcs.005801.

Shu, Xiaokun; Lev-Ram, Varda; Deerinck, Thomas J.; Qi, Yingchuan; Ramko, Ericka B.; Davidson, Michael W. et al. (2011): A genetically encoded tag for correlated light and electron microscopy of intact cells, tissues, and organisms. In: *PLoS biology* 9 (4), e1001041. DOI: 10.1371/journal.pbio.1001041.

Sigmund, Felix; Massner, Christoph; Erdmann, Philipp; Stelzl, Anja; Rolbieski, Hannes; Desai, Mitul et al. (2018): Bacterial encapsulins as orthogonal compartments for mammalian cell engineering. In: *Nature communications* 9 (1), S. 1990.

Sigmund, Felix; Pettinger, Susanne; Kube, Massimo; Schneider, Fabian; Schifferer, Martina; Schneider, Steffen et al. (2019): Iron-Sequestering Nanocompartments as Multiplexed Electron Microscopy Gene Reporters. In: *ACS nano* 13 (7), S. 8114–8123.

Sirivech, S.; Frieden, E.; Osaki, S. (1974): The release of iron from horse spleen ferritin by reduced flavins. In: *Biochem J* 143 (2), S. 311–315. DOI: 10.1042/bj1430311.

Stanley, Sarah A.; Gagner, Jennifer E.; Damanpour, Shadi; Yoshida, Mitsukuni; Dordick, Jonathan S.; Friedman, Jeffrey M. (2012): Radio-wave heating of iron oxide nanoparticles can regulate plasma glucose in mice. In: *Science (New York, N.Y.)* 336 (6081), S. 604–608. DOI: 10.1126/science.1216753.

Stanley, Sarah A.; Kelly, Leah; Latcha, Kaamashri N.; Schmidt, Sarah F.; Yu, Xiaofei; Nectow, Alexander R. et al. (2016): Bidirectional electromagnetic control of the hypothalamus regulates feeding and metabolism. In: *Nature* 531 (7596), S. 647–650. DOI: 10.1038/nature17183.

Stanley, Sarah A.; Sauer, Jeremy; Kane, Ravi S.; Dordick, Jonathan S.; Friedman, Jeffrey M. (2015): Remote regulation of glucose homeostasis in mice using genetically encoded nanoparticles. In: *Nature medicine* 21 (1), S. 92–98. DOI: 10.1038/nm.3730.

Stopford, Woodhall; Turner, John; Cappellini, Danielle; Brock, Tom (2003): Bioaccessibility testing of cobalt compounds. In: *Journal of environmental monitoring : JEM* 5 (4), S. 675–680. DOI: 10.1039/b302257a.

Sun, Conroy; Lee, Jerry S.H.; Zhang, Miqin (2008): Magnetic nanoparticles in MR imaging and drug delivery. In: *Advanced Drug Delivery Reviews* 60 (11), S. 1252–1265. DOI: 10.1016/j.addr.2008.03.018.

Sutter, Markus; Boehringer, Daniel; Gutmann, Sascha; Günther, Susanne; Prangishvili, David; Loessner, Martin J. et al. (2008): Structural basis of enzyme encapsulation into a bacterial nanocompartment. In: *Nature Structural & Molecular Biology* 15 (9), S. 939–947. DOI: 10.1038/nsmb.1473.

Takemura, Shin-ya; Bharioke, Arjun; Lu, Zhiyuan; Nern, Aljoscha; Vitaladevuni, Shiv; Rivlin, Patricia K. et al. (2013): A visual motion detection circuit suggested by Drosophila connectomics. In: *Nature* 500 (7461), S. 175–181. DOI: 10.1038/nature12450.

Tamura, Akio; Fukutani, Yosuke; Takami, Taku; Fujii, Motoko; Nakaguchi, Yuki; Murakami, Yoshihiko et al. (2015): Packaging guest proteins into the encapsulin nanocompartment from Rhodococcus erythropolis N771. In: *Biotechnol. Bioeng.* 112 (1), S. 13–20. DOI: 10.1002/bit.25322.

Theil, Elizabeth C. (2011): Ferritin protein nanocages use ion channels, catalytic sites, and nucleation channels to manage iron/oxygen chemistry. In: *Curr Opin Chem Biol* 15 (2), S. 304–311. DOI: 10.1016/j.cbpa.2011.01.004.

Theil, Elizabeth C.; Behera, Rabindra K.; Tosha, Takehiko (2013): Ferritins for Chemistry and for Life. In: *Coordination chemistry reviews* 257 (2), S. 579–586. DOI: 10.1016/j.ccr.2012.05.013.

Thélohan, S.; Meringo, A. de (1994): In vitro dynamic solubility test: influence of various parameters. In: *Environ Health Perspect* 102 Suppl 5 (Suppl 5), S. 91–96. DOI: 10.1289/ehp.102-1567254.

Toussaint, Louise; Bertrand, Luc; Hue, Louis; Crichton, Robert R.; Declercq, Jean-Paul (2007): High-resolution X-ray structures of human apoferritin H-chain mutants correlated with their activity and metal-binding sites. In: *Journal of molecular biology* 365 (2), S. 440–452. DOI: 10.1016/j.jmb.2006.10.010.

Treffry, Amyra; Hirzmann, Jorg; Yewdall, Stephen J.; Harrison, Pauline M. (1992): Mechanism of catalysis of Fe(II) oxidation by ferritin H chains. In: *FEBS Letters* 302 (2), S. 108–112. DOI: 10.1016/0014-5793(92)80417-F.

Tsien, Roger Y. (1998): THE GREEN FLUORESCENT PROTEIN. In: *Annual Review of Biochemistry* 67 (1), S. 509–544. DOI: 10.1146/annurev.biochem.67.1.509.

Valdés-Stauber, N.; Scherer, S. (1994): Isolation and characterization of Linocin M18, a bacteriocin produced by Brevibacterium linens. In: *Appl Environ Microbiol* 60 (10), S. 3809–3814. Online verfügbar unter https://pubmed.ncbi.nlm.nih.gov/7986050.

Vladimirova, Lilia S.; Kochev, Valery K. (2010): Potentiometric assessment of iron release during ferritin reduction by exogenous agents. In: *Analytical biochemistry* 404 (1), S. 52–55. DOI: 10.1016/j.ab.2010.04.027.

Wang, Qing; Mercogliano, Christopher P.; Löwe, Jan (2011): A ferritin-based label for cellular electron cryotomography. In: *Structure (London, England : 1993)* 19 (2), S. 147–154. DOI: 10.1016/j.str.2010.12.002.

Watt, G. D.; Frankel, Richard B.; Papaefthymiou, G. C. (1985): Reduction of mammalian ferritin. In: *Proceedings of the National Academy of Sciences* 82 (11), S. 3640–3643.

Wheeler, Michael A.; Smith, Cody J.; Ottolini, Matteo; Barker, Bryan S.; Purohit, Aarti M.; Grippo, Ryan M. et al. (2016): Genetically targeted magnetic control of the nervous system. In: *Nature neuroscience* 19 (5), S. 756–761. DOI: 10.1038/nn.4265.

White, John G.; Southgate, Eileen; Thomson, J. Nichol; Brenner, Sydney (1986): The structure of the nervous system of the nematode Caenorhabditis elegans. In: *Philos Trans R Soc Lond B Biol Sci* 314 (1165), S. 1–340.

Xiao, Wei; Jones, Adele M.; Collins, Richard N.; Waite, T. David (2018): Investigating the effect of ascorbate on the Fe(II)-catalyzed transformation of the poorly crystalline iron mineral ferrihydrite. In: *Biochimica et biophysica acta. General subjects* 1862 (8), S. 1760–1769. DOI: 10.1016/j.bbagen.2018.05.005.

Yakubov, Kh.M.; Vinnichenko, G. M.; Offengenden, E.Ya.; Astanina, A. N. (1983): Iron coordination compounds with glycine, glycylglycine and diglycylglycine. In: *Inorganica Chimica Acta* 79, S. 273–274. DOI: 10.1016/S0020-1693(00)95319-2.

Yan, Lei; Zhang, Shuang; Chen, Peng; Liu, Hetao; Yin, Huanhuan; Li, Hongyu (2012): Magnetotactic bacteria, magnetosomes and their application. In: *Microbiological research* 167 (9), S. 507–519. DOI: 10.1016/j.micres.2012.04.002.

Zheng, Zhihao; Lauritzen, J. Scott; Perlman, Eric; Robinson, Camenzind G.; Nichols, Matthew; Milkie, Daniel et al. (2018): A Complete Electron Microscopy Volume of the Brain of Adult Drosophila melanogaster. In: *Cell* 174 (3), 730-743.e22. DOI: 10.1016/j.cell.2018.06.019.

Acknowledgements

I am deeply grateful to my mentor and PhD supervisor, Prof. Gil Westmeyer, who gave me the chance to work on these challenging but interesting topics in a highly interdisciplinary scientific field. Not only did I have plenty of scientific possibilities and a great amount of freedom to develop and pursue own ideas, he also taught me to always keep the bigger picture in my mind. I also greatly enjoyed our scientific discussions and exchanges which always brought up new ideas and exciting concepts.

Furthermore, I would like to thank my mentor Prof. Michael Winklhofer, his input during meetings and discussions was always helpful and added new perspectives to my project. I also want to thank my second supervisor Prof. Wolfgang Wurst for his helpful inputs and for the resources he made available to me at the Institute of Developmental Genetics (IDG). I also thank Prof. Vasilis Ntziachristos and all the people at the Institute of Biological and Medical Imaging (BMI) for the fruitful discussions as well as the resources they shared with me.

I am grateful to all collaborators who helped with important experiments and measurements and provided analytical methods we could not conduct in our laboratory. I would like to thank Carolin Hartmann and Natasha Ivleva not only for the Raman analyses they provided, but also for the great scientific exchange, the meetings and discussions that always helped to progress our joint project. I also want to mention Ulf Wiedwald and Michael Winklhofer, who not only performed SQUID and VSM measurements, but were also extremely helpful in analyzing and interpreting data and who always found time for helpful discussions. A special thanks goes to Fabian Schneider and Massimo Kube, who performed cryo-EM analysis of the encapsulin and who not only provided helpful information but were also always open for discussions. I am grateful to Dr. Damian Faivre and Lucas Kurths for performing X-ray diffraction measurements. I would also like to thank Michaela Aichler, who performed several TEM measurements to visualize encapsulins in various sample preparations.

I thank all the former and current lab members Sheryl, Ahne, Antonella, Michele, Panos, Anurag, Jeff, Hannes, Silviu, Mariia and Yuan Yuan for their scientific input, the helpful discussions and all the fun time we spent together. Our kicker tournaments will forever be a fond memory for me! In particular, I want to thank Christoph Massner and Felix Sigmund, who have supervised my Master's Thesis and not only sparked my interest in the whole research field, but also aided me with many practical aspects of my research work. Chris was an enormous help especially in the beginnings of my PhD, where he was not only providing a lot of support on scientific aspects but also helped me with developing my project. His thoughts and input as well as the regular discussions we had guided me throughout my work and collaboration with him. Felix was a great support towards the end of my PhD when we collaborated on the encapsulin project. I not only greatly enjoyed working with him, I also admired his profound knowledge and his ability to solve any upcoming problem. A huge thanks goes to Anja Stelzl, who is not only an amazing technician and an incredible organizational talent, but also the lab's fairy godmother. Her cakes and her friendly ear helped me through difficult times. Another thank goes to Tobias Köllen, who was first doing an internship and then worked as a student assistant for me. I also want to acknowledge Tanja Orschman; while not part of our group, she was always willing to share great advice and she never failed to raise my spirits.

I also want to mention the iGEM Munich 2019 team. While they did not directly contribute to my PhD project, supervising the team was a unique and challenging experience for me. These 8 months have been some of the most intense in my life so far, but they also taught me a lot about team leadership and social dynamics. I greatly enjoyed the time we spent in Boston as a team, as well as all the good times we had on our journey there.

Most importantly, I want to thank my whole family, my parents, sisters, aunts and uncle for their continuous, unconditional support during all my life including this PhD. My older sisters Gela and Tine have always been both inspiration and role models, and they never failed to be there for moral support. Finally, my parents have always granted me the freedom and support to explore my interests, be it music or biochemistry, and at the same time they always unfailingly, unwavering there for me whenever I needed them. Without all of them, I wouldn't be where I am today. Thank you!